國立交通大學

材料科學及工程研究所

博士論文

低溫化銀電極膏製備與高頻應用之研究
Preparation and High-frequency Application of Low-temperature-curing Silver Paste

研　究　生：林鴻欽

指導教授：林　鵬　教授

　　　　　王錫福　教授

中華民國九十七年七月

低溫化銀電極膏製備與高頻應用之研究
Preparation and High-frequency Application of Low-temperature-curing Silver Paste

研究生：林鴻欽　　Student：Hong-Ching Lin

指導教授：林鵬　　Advisor：Pang Lin
王錫福　　Sea-Fue Wang

國立交通大學
材料科學及工程研究所
博士論文

A Thesis
Submitted to Department of Materials Science and Engineering
College of Engineering
National Chiao Tung University
in partial Fulfillment of the Requirements
for the Degree of
Doctor of Philosophy
in

Materials Science and Engineering Science

July 2008

Hsinchu, Taiwan, Republic of China

中華民國九十七年七月

低溫化銀電極膏製備與高頻應用之研究

學生：林鴻欽　　　　　　　　　　　　　　指導教授：林　鵬

王錫福

國立交通大學材料科學及工程研究所　博士班

摘　　要

本論文研究分別以草酸銀和氧化銀做為誘發金屬有機銀鹽類（Metallo-Organic Decomposition, MOD）的反應劑，以高速混合機及三軸滾輪進行混合及分散等來製備金屬銀膏。銀膏之燒附條件可藉由草酸銀和氧化銀的添加而降低金屬有機銀鹽類產生熱裂解反應（Thermal Decomposition Reaction）的溫度，並使金屬有機銀鹽類與添加劑還原形成奈米金屬銀後形成金屬膜。

本研究針對所製備出之金屬膜層進行分析與研究，藉由熱重分析(Thermogravimetric analysis, TGA)、熱差分析（Differential thermal analysis, DTA) 與（Derivative thermogravimetry, DTG)等，探討不同反應劑對金屬有機銀鹽類之熱裂解反應，並藉由掃瞄式電子顯微鏡（SEM)分析金屬膜之微結構及燒附現象，透過動態流變儀(Stress and Strain Rheometers）量測之黏彈性行為（Viscoelasticity）探討不同反應劑於膏體中之各項流變特性等。針對其中分布均勻性與觸媒反應特性最好之氧化銀反應劑進行成份及熱裂解反應等深入之探討與研究，找尋出最佳之組合量。研究中更針對高溫、低溫燒附行為之金屬膜層的高頻阻抗特性進行深入研究與比較。並初步完成濾波器元件特性，後續將針對低溫高頻元件進行研究。

Preparation and High-frequency Application of Low-temperature-curing Silver Paste

Student：Hong-Ching Lin
Advisors：Dr. Pang Lin
Dr. Sea-Fue Wang

Department of Materials Science and Engineering
National Chiao Tung University

ABSTRACT

In this study, at first, focus on the effect of silver oxalate addition on physical characteristics of metallo-organic-decomposition (MOD) silver screen-printable paste for thick film technology. The addition of silver oxalate in the paste not only produces fresh fine silver particles after curing, but also reduces the decomposition temperature of the lubricant coated on the silver flakes. This is an effective route to provide fine silver particles to the paste without significantly changing the rheological behavior.

Then, the next study focus on paste formulations containing silver oxide coated with MOD (metallo-organic decomposition) agent of silver stearate were prepared without the use of any silver powders or silver flakes. The lowest electrical resistivity of $13.2\text{x}10^{-6}$ Ω-cm was obtained for the film prepared from paste with the Ag_2O/silver stearate ratio of 100:5 at a solid loading of 80wt% in solvent α-terpineol, after being cured at 160°C for 5min, which meets the requirements of low-temperature and high speed manufacturing for practical applications. Co-existence of the Ag_2O and silver stearate induces their simultaneous transformation to the silver form at temperatures below 160°C.

The electrical properties of silver films, prepared using a low-curing-temperature metallo-organic-decomposition (MOD) paste and a high-temperature silver paste screen-printed on polished and nonpolished alumina substrates, at microwave frequency were characterized in this study. At last, to evaluate RF electrical properties between low-temperature-curing and high-temperature silver paste, multilayered structure and the low-temperature co-fired ceramic technology are employed to design and fabricate the filter.

誌　　謝

由衷感謝我的指導教授-林鵬 博士和王錫福 博士，在這段時間對我辛勤的教導。在實驗嚴謹性的要求和論文撰寫的指導上讓我獲益良多，在此致上最深的謝意。

再來要感謝的是工研院材化所讓我有進修的機會，在此要謝謝我的長官們，尤其是洪英彰副組長無論是在實驗上和生活態度上都毫不吝嗇的提供建議。另外特別要感謝盧俊安學弟在實驗和論文資料整理的大力幫忙。也要感謝研究室的其他同仁: 啟仁、信賢、麗琳、宏達、穎容、炯雄和俊璋，在工作上的鼎力協助讓我能順利完成學業。因為論文完成的時間太長，如果有遺漏的同仁請不要介意。

特別要感謝我的家人，感謝父母在我成長路上的栽培。 感謝我的內人如惠在這一段漫長的日子裡對我的幫助與包容，還有老天賜給我三個可愛的小孩長盟、長楙和長鈺，他們帶給我的精神力量。

最後要感謝在已經在天上的紀財叔公和紀備叔父的鼓勵。

Contents

Table Caption

Chapter 1

Chapter 3

Chapter 4

Chapter 6

Chapter 7

Figures Caption

Chapter 1

Chapter 2

Chapter 3

Chapter 4

Chapter 5

Chapter 6

Chapter 7

Chapter 1

Overview

Flexible electronics is emerging as a multidisciplinary research topic with far-reaching impact in a number of research areas, including flat-panel displays, organic electronics and distributed macro electronic systems and architectures. Furthermore, for the requirements of high performance, multiple functions and high production efficiency, to do the best to decrease the processing temperature and processing time and to retain the desired functional properties are essential for the development of flexible electronics.

Well conductors, such as gold, silver, copper and aluminum etc., are extensively applied in electronic devices, due to the low resistivity property. In order to process compatibly with the flexible polymer substrate, it is the grand challenge to develop the low-curing-temperature and high conductivity metal paste.

1-1. General Background

Metals are widely used because of their properties: strength, ductility, toughness, high melting point, thermal and electrical conductivity. Metal conductors (gold, silver, copper and aluminum) have good conductivity with excellent electron transmission ability for electronics industry. The pure bulk metal electrical conductivity and thermal conductivity properties were shown at **Table 1-1.** The metal excellent electrical conductivity can make use of any electron transmission for electronics devices, such as, metal circuit, antenna pattern, inner interconnect, terminal electrode of passive component and front-end module etc. For popularity applications were inner circuit electrode and terminal electrode of capacitor, inductance and ceramic module, surface circuit of IC, and circuit pattern of antenna. Flexible electronics become the new devices tendency and direction. Products can be flexibility for collection and application were promoted the life handling convenient. For popularity products, like as, Flexible full color display, polysilicon thin film transistor, Organic filed effect transistors, organic light emitting diodes, amorphous silicon solar cell, and low cost RFID (Radio Frequency Identification).

Recently, the real application of flexible electronics is RFID tags. Tags consist of antenna, IC chip and substrate. Typical dielectric substrate choices for RFID applications include polyester (PET), FR4, paper, high permittivity dielectrics, etc. For conducting materials, several choices are available, including silver paste, copper, aluminum and others. For ultra-high frequency (UHF) application, the antenna is typically a dipole design as shown in the figure. RFID tags will be used for comparison with current methodologies to elucidate the advantage of high speed roll to roll printing presses in the manufacture of electrical interconnects[1]. The low cost RFID tags are applied to logistic application by Wal-Mart, since they expect to replace UPC barcodes on consumer products, ushering in an era of enhanced consumer convenience and warehousing efficiency, though a realization of real-time price and product controls, automated inventory processes, and automated checked[2]. RFID is hitting the mainstream now for a number of reasons. There are three parts of the RFID system. The tag is affixed to the item being tracked. The reader is the device that reads the tag. The third part of the system is the antennas, an important of communication between the tag and reader[3]. The system figure was shown at Figure 1-1.

An important performance criterion for RFID tag is its read range – the maximum distance at which tag can be detected. Theoretical read range can be calculated as:

$$D = \frac{\lambda}{4\pi}\sqrt{\frac{P_t G_t G_r \tau}{P_{th}}} \qquad (1.1)$$

where λ is the wavelength ,

P_t is the power transmitted by the reader,

G_t is the gain of the transmitting reader antenna,

$\tau = \mathrm{Re}(Zc)\mathrm{Re}(Za)/|Zc+Za|^2$ is the power transmission coefficient (Zc is chip impedance)

P_{th} is the minimum threshold power necessary to power up the chip.

It can be concluded that the tag performance depends both on material and on the shape of the antenna[4]. Silver paste is not as conductivity of copper but is inexpensive and can be printed in affordable way on flexible substrate. That is a challenge how to develop printed conductive paste to suit to high throughput for RFID tags.

Some previously investigated such as a technology, based on metallic nanoparticles. Small-diameter nanoparticles have reduced melting points relative to their bulk material counterparts. Some technology investigated such as a technology, based on polymer additions.

Used polymer low temperature curing to consolidate the structure and used flake metal powder to connect each other were form electrons conductivity and flexibility. The DuPont were developed the polymeric think film (PTF) for RFID tags and smart labels application. The paste has been specially developed for the printing of coils for RFID tags and for contactless smart cards and has the following key properties. This produces has 10-20 mΩ/sq at 25mm after drying and 4-8 mΩ/sq at 25μm after lamination. And can substrate compatibility at polyester, ABS, polycarbonate and paper [5].

Another conductive process way, punched aluminum offers a cheaper alternative but as it is a subtractive process it is only possible to maintain the high level of waste by the relatively low cost of aluminum. And aluminum does not offer the same conductivity as silver and products made by this technique offer interior performance.

However, materials development of metal conductivity ink was important factor for low-cost roll-to-roll process and other low temperature process of low cost technology. The Parelec Inc[6,7], innovative process provides a high yield and two-step process which printing and curing. The system that is adaptable to sheet fed or roll-to-roll printing processes. The materials are comprised of metal particles and a reactive organic medium (MOD) that volatilizes during the heating process and can cure very quickly to give a very thin highly conductive film[show at **Figure 1-2**]. The films can cure in 25 seconds to 5 minutes at temperature as low as 135℃ in a box oven or roll-to-roll continuous print and cure production line.

Technology advances in the fields of materials, printing, and electronics have led to the evolution of the field of printable electronics. Direct printing of electronic features may eliminate complex procedures employed in traditional electronics manufacturing, leading to low cost devices.

1-2. Silver paste

Metal pastes are currently used for the production of various electrical and electronic components such as solar cells, multilayer ceramic capacitors, single and multichip modules and hybrids for the automotive and aerospace industries. All these applications require finely structured conductive layers, which are usually produced with screen printing technologies, using metal powders containing print paste.

For multilayer ceramic devices, high conductivity of the internal metallization is important to reduce the dissipation factor, especially at high frequencies[8, 9]. Ag powder has a problem of shrinkage mismatch with the dielectric during co-firing because the metal film starts to sinter at lower temperatures and it rapidly becomes very dense. This shrinkage mismatch can potentially create tensile stress in the region which sinters faster and shrinks more.

It is a method for minimizing shrinkage mismatch by coating the Ag powder surface with Ti organometallic compounds. It was found that the formation of nanocrystallized titania accompanied the combustion of the organometallic compounds and was found to inhibit the densification of silver at low temperature, thus retarding sintering of the silver to a higher temperature[10].

Conventionally, on the substrate, the terminal electrode by the conductive paste and the dielectric layer by the dielectric print a printing ceramic condenser in the shape of sandwiches, and it is formed. Generally this conductive paste makes powder, such as Ag, Au, Pd, Pt, Cu and Ni., the shape of paste by the glass frit and the organic vehicle, and used. Sometime the conductive paste of Ag system has added Pd, in order to lessen the solder foods crack at the time of soldering of the terminal electrode of this printing ceramic condenser product and to prevent it. The purity of metals powders that is now typically required for the production of metal pastes is not at all well-defined. In most cases, only the main metal content is analyzed, whereas the presence of trace elements is normally neglected. But trace element content, in particular, can significantly influence rheological properties and long-term storage stability of pastes. For metal powder, some parameters must be select for different applications, such as, particles size distribution, tap density, fisher sub sieve sizer, surface area, sintering losses conditions, degree of deagglomerated, and powder shape (coarse, general or flake) etc,. All of the foregoing parameters were effect the paste rheology for printing of other process conditions and phenomenon of after sintering for microstructure and physical characteristic.

The typical pastes used today are based on organic solvents such as butyl carbitol acetates, terpineol, hydrated castor oils in combination with rheological additives such as pine or fish oils. Most experts agree that in the long-term use of such solvents is inconsistent with aims to protect the environment and with the concept that ecological aspects should be integrated into production procedures. Some solvent used today are based on water solvents, but general are used at low temperature or quickly curing paste, some low viscosity paste application and requirement of environmental.

Low-curing-temperature conductor technology with metallo-organic decomposition (MOD) compound additions was investigated to form a three dimensional metal network. MOD compounds are generally synthetic metallo-organic salts that can decompose completely at low temperatures to precipitate metal or oxide, depending on the metal and atmosphere[11,12].

MOD silver pastes with silver flakes substituted by Ag_2O and AgO to modify the curing conditions while retaining good electrical conductivity were analyzed. Results indicate that the silver oxides effectively catalyze the organic species. The reduced silver and the remaining Ag_2O enhance the connectivity of the silver flake and thus increase the electric conductivity of the films[11].

1-3. Analyses and Measurement Techniques

1-3-1 Thermogravimetric analysis, TGA[13]

Thermogravimetric analysis (TGA) was the study of weight changes of a specimen as a function of temperature. The technique is useful strictly for transformations involving the absorption or evolution of gases from a specimen consisting of a condensed phase. Typical TG specimen powder or liquid was placed on a refractory pan, often porcelain or platinum. The pan, in the hot zone of the furnace, is suspened from a high precision balance. A thermocouple is in close proximity to the specimen but not to interface with the free float of the balance. The balance was electronically compensated so that the specimen pan does not move when the specimen gain or loss weight.

If reactive gases are passed through the specimen chamber or gases are released by the specimen, the chamber containing the balance is often maintained at a slightly more positive pressure via compressed air or inert gas; this is in order to protect the balance chamber and its associated electronic components from exposure to corrosive gases.

Sometime were shown the figure is the numerical derivative TG trace (DTG), which is a smoothed plot of the instantaneous slope of the specimen mass with respect to time. DTG does not contain any new information, however it clearly identifies the temperature at which mass loss is at maximum “the DTG peak”. Superimposed transformations, which are seen only as subtle slope changes in a TG trace appear more clearly shown as DTG peaks. Comparison of DTG data with DTA data of the same material shows striking similarity for those transformations with an associated weight change. Thus, combining DTA and DTG traces is useful for differentiating the types of transformations depicted by the DTA trace.

Thermogravimetric analysis that provide for a spell of constant temperature of a specimen once the non-steady heating is over give the most correct results. They are used to determine key physical and chemical properties of individual substances. The percentage difference was calculated as:

$$p = [(T_f - T_{sp}) / T_f] \cdot 100\% \qquad (1.2)$$

The results of thermogravimetric analysis cast doubts over the validity of a number of experimental investigations in which the reference temperature for the data obtained was that of the furnace space rather than the specimen temperature. Note than an intensification of heating did not lead to a proportional increase in the temperature of specimens T_{sp} which leveled out at an ultimate value peculiar to every substance.

Dynamic thermal analysis of thermal decomposition was investigated by thermogravimetric analysis. Depending on the importance and goals of investigation, one may call upon various types of heaters: convective heaters, lasers, plasma gun and a whole range of burners and furnaces. The derivatographs manufactured produce TG and DTG curves, which make it possible to determine the thermal effects of decomposition, complete with the decomposition rate records $\dot{\omega} = \omega(t)$.

The most common approach to describing the kinetics of isothermal decomposition is to consider it as a homogeneous one-stage chemical reaction:

$$\frac{d\omega}{dt} = -k\omega^n \qquad (1.3)$$

Where, *n* is the reaction order; *w* is the weight per unit of a reacting substance; *k* is reaction rate constant at a given temperature; $w=M/M_0$. By integrating blow equation one can obtain an analytical expression describing the kinetic curves of decomposition. At n = 1:

$$\omega = \omega_0 \exp^{-(kt)} \qquad (1.4)$$

The constant of integration, w_0, is determined by the initial condition,

$\omega|_{t=0} = \omega_0$. It is not much more difficult to obtain solutions at $n \neq 1$.

One-stage chemical reaction between gases and solutions sometimes follow fairly well the empirical Arrhenius equation in relatively narrow ranges of temperature:

$$k = k_0 \exp^{(-E/RT)} \tag{1.5}$$

Where, k_0 is pre-exponential factor; E is activation energy.

The equation includes the Boltzmann constant $e^{-E/RT}$ which has a physical meaning in rate calculations for gas-phase reactions, according to the theonection that a more elaborate temperature dependence of the rate of chemical reactions was derived from this theory [14]:

$$k = (k_B T / h) k_0 \exp^{(-E/RT)} \tag{1.6}$$

Where, the k_0 coefficient takes account of changes in entropy and in the number of particles produced when an activated complex is being formed which has great bearing on polymer systems.

The physical irrelevance of apparent characteristics is evident in activation energy changing with temperature and depending on the extent of conversion, pre-exponential factor is, in turn, often time-dependent and differeing from its theoretical value of 10^{12} s^{-1}.

The theory of absolute rates of chemical reactions forms the groundwork of blow equation within the strict framework of rigorous limitations the most important of which are:

1. the reaction should be homogenous and occur in a gas medium;
2. the starting compound should be in equilibrium with its activated complex;
3. temperature and all other parameters are constant;

4. the reaction does not alter the Maxwell-Boltzmann equilibrium distribution;

Non-isothermal decomposition of solid substances fails to meet these requirements to a lesser or greater extent. It is a heterogeneous process developing at phase boundaries. This equilibrium between an initial substance and its activated complex is broken by the loss of vibration stability of oscillators in three-dimensional and liner crystals. Kinetic equations of heterogenous decomposition of solids were shown at **Table 1-2**. The equations cited may describe intricate kinetic curves more than exponential equations, yet they fall short of taking into account certain factors of nonisothermal heating such as homogeneous nucleation. The thermodynamic feasibility of such nucleation is well established and experimentally verified for metastable liquids[15].

Responding to the practical need to have simple analytical relationships for TG curves, many researchers are determined to apply equations derived for isothermal conditions to the kinetics of decomposition during monotonic heating. The KEKAM equation, which incorporated the Arrhenius law, will then become:

$$\frac{d\alpha}{dt} = nk_0^{1/n}\exp(-E/nRT)(1-\alpha)[1-In(1-\alpha)^{1-1/n}] \tag{1.7}$$

At constant heating rate:

$$[-In(1-\alpha)]^{1/n} \cong [nk_0^{1/n}RT^2/bE]\exp(-E/nRT) \tag{1.8}$$

To describe the non-isothermal kinetics of decomposition of condensed substances, many also adopt the One-stage chemical reaction equation:

$$\frac{d\omega}{dT} = (-k_0 / b)\exp(-E / RT)\omega^n \tag{1.9}$$

The TG curves of linear polymers while quantitatively different from calculated curves are qualitatively the same at low heating rates. More complex substances such as coals and thermosets do not evince even a qualitative agreement with calculated plots at high heating rates.

1-3-2 Differential thermal analysis, DTA[13]

Differential Thermal Analysis DTA, can provide the some material information during thermal processing. The temperatures of transformations as well as the thermodynamics and kinetics of a process may be determined using DTA. The DTA information of material were glass transition, crystallization temperature, melting temperature, and any reaction about exothermic and endothermic during thermal processing.

The Differential Thermal Analysis (DTA), measures the difference in temperature between a sample and reference which are exposed to the same heating schedule via symmetric placement with respect to the furnace. The reference material is any substance, with about the same thermal mass as the sample, which undergoes no transformations in the temperature range of interest. The temperature difference between sample and reference is measured by the differential thermocouple in which one junction is in contact with the underside of the reference crucible. The sample temperature is measured via the voltage across the appropriate screw terminals and similarly for the reference temperature; generally only one or the other is recorded.

The material sample undergoes a transformation, the single will either absorb, means endothermic, or release, means exothermic, heat. Usually the melting of solid material will absorb heat, where that thermal energy is used to promote the phase transformation. The DTA will detect that the sample is cooler than the reference, and will indicate the transformation as the endothermic on the plot of differential temperature (ΔT) versus time.

In order to analyze the differential heating curve, it is convenient to write down a formal expression for the rate at which heat is transferred into and out of the sample or reference cell.

$$\frac{dq_s}{dt} = K_s(T_w - T_s) + \sigma(T_r - T_s) + \alpha(T_0 - T_s) \tag{1.10}$$

$$\frac{dq_r}{dt} = K_r(T_w - T_r) + \sigma(T_s - T_r) + \alpha_r(T_0 - T_r) \tag{1.11}$$

Here *dq/dt* is the rate at which heat is received by the reference material and sample material, respectively. *Kr* and *Ks* are heat transfer coefficients between the materials and the furnace wall. They are made as nearly identical as possible by choice of reference material and design of cell and furnace. Sigma is the heat transfer coefficient between the cells, and alpha is the heat loss to the outside environment. T_w, T_r, T_s and T_0 are the temperature of the furnace wall, reference and sample materials, and external environment, respectively.

Next use can be made of the identity

$$\frac{dq}{dt} = \frac{dH}{dt} = \frac{dH}{dt}\frac{dT}{dt} \tag{1.12}$$

For the sample it is convenient to segregate the portion of the increased heat content arising from phase change, writing

$$\frac{dq_s}{dt} = C_s \frac{dT_s}{dt} + \Delta H \frac{df}{dt} \tag{1.13}$$

Here C_s is the heat capacity of the cell plus its contents, while ΔH is the heat of the transformation and *df/dt* is its time rate of occurrence under the conditions of the experiment, *f* being the fraction of the sample transformed at any time *t*.

For reaction kinetics in DTA, the temperature distribution in the differential thermal analysis specimen holders obeys the general heat flow equation.

$$\frac{\partial T}{\partial t} - \frac{k}{\rho c}\nabla^2 T = \frac{1}{\rho c}\frac{dq}{dt} \tag{1.14}$$

Where *T* is the temperature, *t* the time, *k* the thermal conductivity, σ the density, *c* the specific heat, and *dq/dt* the rate of heat generation due to a chemical reaction per unit volume of sample. No heat effects occur in the reference sample, so the temperature distribution in the reference is given by:

$$\frac{\partial T}{\partial t} = \frac{k}{\rho c}\nabla^2 T \tag{1.15}$$

The differential temperature is the difference in temperature of the centers of the two samples. The differential temperature, θ, is then given by

$$\theta = f\left(\frac{dq}{dt}\right)_{sample} - \left(\frac{\phi \rho c a^2}{4k}\right)_{reference} \tag{1.16}$$

This equation it is seen that when d^2q/dt^2, the derivative of the rate of heat absorption, is zero, $d\theta/dt$ is also zero. Since the rate of heat absorption is proportional to the rate of reaction, the equation states that the peak differential deflection occurs when the reaction rate is a maximum. So the results of the differential thermal study agree with results obtained isothermally except in some specific cases.

1-3-3 Stress and Strain Rheometers[16]

Rheology is the science of deformation and flow. It is a branch of physic since the most important variables come from the field of mechances: forces, deflections and velocities. All forms of shear behavior, which can be described rheologically in a scientific way, can be viewed as lying in between two extremes: the flow of idealviscous liquids on one hand and the deformation of idealelastic solids on the other. The behavior of all real materials is based on the combination of both the viscous and the elastic portion and therefore, it is called ***viselastic***.

Rheometry is the measuring technology used to determine rheological data. The emphasis here is on measuring system, instruments and analysis methods. Both liquids and solids can be investigated using rotational and oscillatory rheometers. Viscosity curves are usually plotted with $\dot{\gamma}$ on the x-axis and η on the y-axis. When measuring at shear rates $\dot{\gamma}$ < 1 1/s, it is important to ensure that the measuring point duration is long enough. This is especially true for high-viscosity samples which are tested at very low shear rates. Otherwise start effects or time-dependent transition effects are obtained, this means the transient viscosity instead of the desired steady-state viscosity is measured. When $\dot{\gamma}$ >1 1/s, transient effects only influence samples with pronounced viscoelastic properties. Therefore, for liquids with low or medium viscosities the duration of t=5 s is sufficient in most cases for each measuring point.

However, transient effects should always be expected for polymers at shear rates $\dot{\gamma} < 1$ 1/s.

Rotational tests are performed to characterize viscous behavior and evaluated viscoeleastic behavior, creep tests, relaxation tests and oscillatory tests are performed. In all fluids, there are frictional forces between the molecules and, therefore, they display a certain flow resistance which can be measured as viscosity. The dynamic viscosity is sometimes used for η. However, many rheologists also use this term to describe either the complex viscosity measured in oscillatory tests or the real part of the complex viscosity. The inverse value of viscosity is referred to as fluidity ϕ and following as:

$$\varphi[1/\mathrm{pas}] = 1/\eta \tag{1.17}$$

For rotational tests, the different types of flow behavior were presented and their rheological background was explained using, for example, Newton’s law or other viscosity functions which depend on the structure of the sample. A normal test for shear rate tests, the speed or shear rate is set and controlled. This tests method with controlled shear rate is usually selected when specific flow velocities of technical processes have to be simulated. The viscosity curves are usually poltted with $\dot{\gamma}$ on the x-axis and η on the y-axis.

To know the structure decomposition and regeneration were measured by thixotropy and rheopexy which are shear rate step function test. For measurements like this, three test intervals are preset:

1. Rest phase under low-shear conditions during the time period between

t_0 and t_1. The aim is to achieve a fairly constant η value for the whole first interval, since it is then used as the reference value for the third interval;

2. Load phase under high-shear condition during the time period between t_1 and t_2 in order to decompose the structure of the sample;
3. Phase after removing the load under low-shear conditions during the time period between t_2 and t_3, under the same shear conditions as in the first interval to facilitate regeneration of the structure.

The extent of thixotropy is given as the change in viscosity $\Delta\eta$, which is calculated as the difference between the maximum viscosity. Here, η_{min} is taken at the time point t_2 and η_{max} at the point t_3. The formula were $\Delta\eta = \eta_{\max} - \eta_{\min}$. And the total thixotropy time is the time difference between the end of the structural decomposition phase and the time point at which the maximum value η_{max} is reached after structural regeneration. The total thixotropy time were analyzed as the period of time required for the structure to reach the state of complete regeneration in the third test interval. The testing and analysis method that flow curve with hysteresis area for determining thixotropic and rheopectic behavior were now outdated, although it is still used for QC tests in some industrial laboratories. The hysteresis area was determined by taking the difference between the following two areas: the area between the upward curve and the γ axis, and the area between the downward curve and the $\dot{\gamma}$ axis. Sample with positive area value were referred to as thixotropic and those with negative values as rheopectic.

For viscoelastic behavior, a viscoelastic material shows viscous and elastic behavior simultaneously. For viscous portion behaves accorded to Newton's law, and elastic portion behaves accorded to Hooke's law. The behavior of viscoelastic liquid can be illustrated using the combination of a spring and a dashpot in serial connection. Both components can be deflected independently of each other. The extent of the reformation represents the elastic portion, and the extent of permanently remaining deformation corresponds to the viscous portion. So the deformation process is irreversible, as the sample has changed its form at the end of the process because its reformation is not complete. Therefore, the material behaves essentially as a liquid and is referred to as a viscoelastic or Maxwell liquid due to the above-mentioned properties.

For an elastic deformation you apply the Hook's law to rheology: Shear Stress $\tau = \frac{F}{A}$, and the deformation $\tau = G^{*}\gamma$. The reasons of viscoelasticity were entanglement in polymers and structure or network of an emulsion. Always used the oscillation test to give the extension of the measuring range, non destructive methode, and analyses data of the material structure and monitoring of time or temperature-depending changes. The oscillation were used the change of direction for input shear stress τ then give the elastic reaction for deformation γ and 0^{0} phase shift for elastic response or 90^{0} viscous response. Separation in elastic and viscous components was:

$$\gamma = \gamma_0 \sin(\omega t - \delta) = \gamma_0[\sin(\omega t)\cos\delta - \cos(\omega t)\sin\delta] \tag{1.18}$$

So to define the complex mouulus:

$$G^* = \frac{\tau}{\gamma} = G' + iG'' \tag{1.19}$$

The G’ is storage modulus to define:

$$G' = G^* \cos\delta \tag{1.20}$$

And G” is loss modulus to define:

$$G'' = G^* \sin\delta \tag{1.21}$$

The oscillatory test included some methods as simple oscillation, time curve for ageing, curing and gelation, and sweep experiment for frequency, amplitude and temperature, and preshear oscillation for structure recovery, and multiwave for monitoring material changes. The stress sweep test was determination of the linear-visco-elastic range for material stability and yield point. The G’ and G” are independent from stress or deformation. All stress sweeps can be presented either as function of stress or strain. For material stability, the critical stress from the stress sweep is used as characteristic value. The frequency sweep was investigated materials response to impact or gradual load and usually applied at material condition, impact resistance, damping properties and mouth feeling. The frequency sweep was obtained the material characterization of gel, paste and liquid material structure. Usually the behaviors were obtained the viscous at low frequency and elastic at high frequency.

Moreover, the time temperature sweeps were observed of change of material properties due to different initiators for material aging, gelation, fusion, curing, crosslinking and degradation. The multiple creep tests were see the slope value deviating from zero and applied for leveling, sagging and stability. Modeling test was described the material functions as mathematical equation. Relaxation test was known the non linear equations incorporate coefficients, which are known as relaxation times.

Reference

1. D. Lochun, E. Zeira and R. Menize., Electronic Components and Technology Conference., (2002).
2. S. Molesa, D. R. Redinger, D. C. Huang, and V. Subramanian., Mat. Res. Soc. Symp. Proc., 769, (2003).
3. J. Kabachinski., Biomedical Instrumentation and Technology., March/April, (2005).
4. Pavel V. Nikitin et al "Low cost silver ink RFID Tag Antennas" IEEE 2005,p.353~356.
5. DuPont's registered trademark.
6. P. H. Kydd: PCT pattern WO 98/37133 (1998).
7. P. H. Kydd: U. S. Patent 6036889 (2000).
8. Herbert J M 1985 *Ceramic Dielectrics and Capacitors* (*Electrocomponent Science Monographs vol 6*) (New York: Gordon and Breach)
9. NoorlanderW 1978 Some aspects of multilayer ceramic chip capacitors for hybrid circuits *Electrocomponent Sci. Technol.***5** 33–40
10. Chi-Jen Shih, Shao-Ju Shih, Hong-Ching Lin, Hsin-Hsien Yeh and Ying-Chang Hung "Thermal-decomposition and crystallization behaviour of coupling agents for silver paste application" Nanotechnology 14 (2003) 1014–1018
11. C. A. Lu, P. Lin, H. C. Lin, and S. F. Wang: Jpn. J. Appl. Phys. 45 (2006) 6987.
12. C. A. Lu, P. Lin, H. C. Lin, and S. F. Wang: Jpn. J. Appl. Phys. 46 (2007) 251.
13. T. X. Liang, W. Z. Sun, L. D. Wang and H. D. Li., IEEE. Trans.

Component. Package. Manuf. Tech. B., 19(2) (1996).

14. S. Glasstone, K. Leidler, and G. Ecring., The Theory of Rate Processes., IL, Moscow., 1948.

15. V. P. Skripov, E. N. Sinitsyn., Termophysical properties of liquids in a metastable state., Moscow, Atomizdat, 1980, 208p.

16. H. P. Le., J. Image. Sci. Tech., 42(1) (1998).

Table 1-1. Metal electrical conductivity and thermal conductivity properties

	Electrical conductivity (μΩ· cm)	Thermal conductivity (W/mK)		Electrical conductivity (μΩ· cm)	Thermal conductivity (W/mK)
Ag	1.59	427.0	Fe	9.71	25.1
Cu	1.67	398.0	Pt	10.6	71.4
Au	2.35	315.0	Pd	10.8	75.5
Al	2.66	237.0	Sn	11.0	66.6
Zn	5.92	121.0	Cr	12.9	90.3
Ni	6.84	90.5	Pb	20.6	35.2

Table 1-2. Kinetic equations of heterogenous decomposition of solids

Basic Factors	Function
Two-dimensional motion of an interface	$(1-\alpha)^{1/2}$
Three-dimensional motion of an interface	$(1-\alpha)^{2/3}$
Linear diffusion	$1/2\alpha$
Three-dimensional diffusion	$3(1-\alpha)^{2/3}/2[1-(1-\alpha)^{1/3}]$
Prout-Tompkins' mechanism	$\alpha(1-\alpha)$
Avrami-Erofeev's mechanism	$(1-\alpha)[-In(1-\alpha)^{1-1/n}]$
Ultimate decomposition temperature T_{u1}	$(1-\alpha)\exp[A/(1/T-1/T_{u1}+\Delta)]$

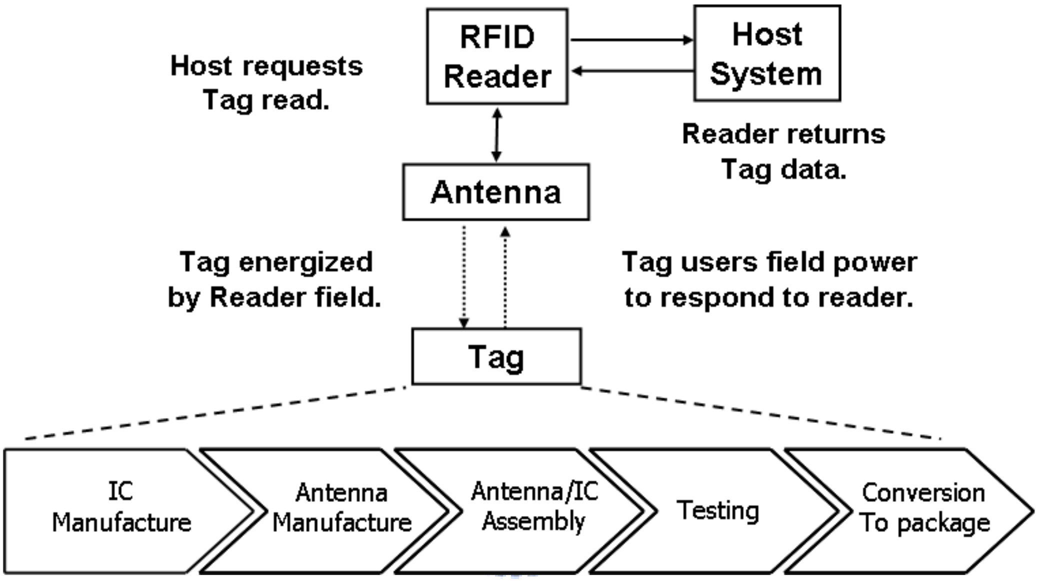

Figure 1-1. A typical RFID System.

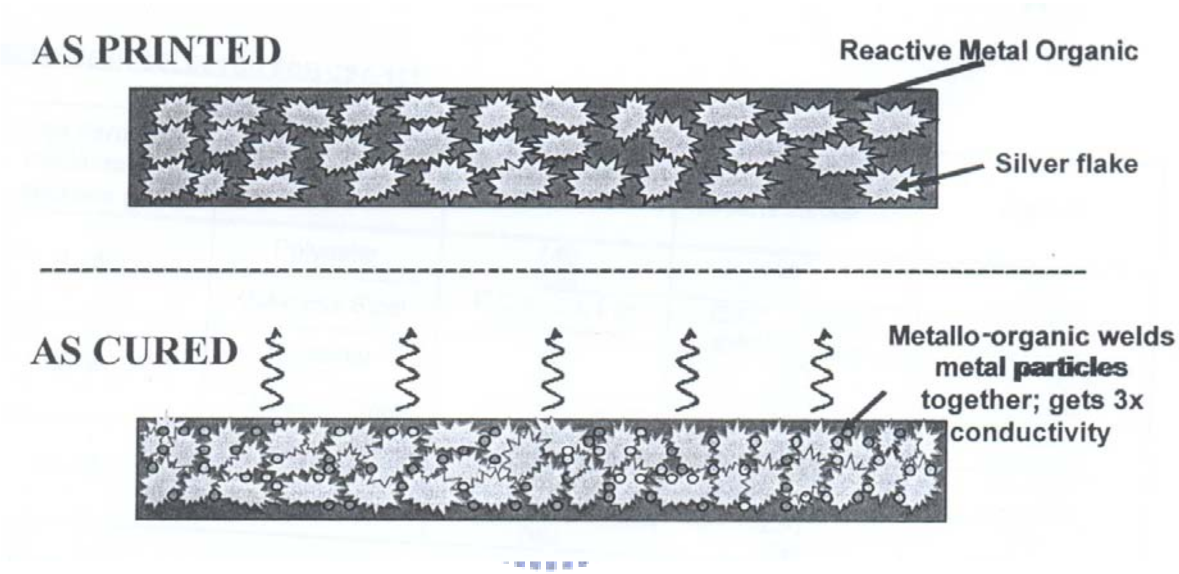

Figure 1-2. The diagram of Parelec Inc innovative 2-step low curing and roll-to-roll printing metal ink process [6].,

Chapter 2

Experiment

2-1. Mixing Process of Paste

The various pastes mixtures, solvent, metal powder and Metallo-organic were mixed by high speed mixer (Thinky Mixer, Japan) for 3 min and then de-bubbled for 1min. The high speed mixer structures were shown at **Figure 2-1.** Subsequently, uniform pastes were formed through a triple roller grinding (EXERT, Germany), which causes breaking down of the pigment agglomerates. The triple roller grinding structures were shown at **Figure 2-2**.

2-2. Printing Process

The paste were screen-printed on alumina substrate as spiral lines and then thermally treated at a range of temperatures, according to the results of thermal study described above. The chart of screen-printing was shown at **Figure 2-3**. The dimension of screen-printed spiral silver metal lines are specifically controlled at the length of 216 cm, the line wide of 0.8mm and the line thickness of 20~40μm to promote the accuracy of the electrical measurement. The spiral line structure and printing results photo was shown at **Figure 2-4** and **Figure 2-5**.

2-3. *Thermal Analyses*

The TG trace were derivatively calculated to identify the thermal decompose temperatures at which the mass loss of the paste is at a maximum. In this research, Termo-gravimetry analyzer (TGA) from Perkin-Elmer was used. Also, the TGA were performed at different heating rates including 2°C /min, 5°C /min, 10°C /min, 20°C /min and 40°C /min, in order to evaluate the activation energy. The decomposition activation energy E_a was calculated using the following formula form Doyle-Ozawa [1]:

$$-\log\phi - 0.4567\left(\frac{E_a}{RT_m}\right) = \text{constant} \tag{2.1}$$

ϕ is the heating rates (dt/dT) of the measurement and T_m is the thermal decompose temperature of the paste measured.

2-4. *Electrical Measurement*

Keithely 2400 multimeter with a four-point probe was used to measure the bulk resistance of curing silver paste. The resistivity of the silver conducting line curied at the different temperature was calculated using the relationship of：

$$\rho = (R \cdot w \cdot d)/l\ . \tag{2.2}$$

R is the silver conducting line bulk resistance measured

w, *l*, *d* are the width, length and thickness of the silver conducting line

And the high-frequency surface resistances were determined using the TE_{011}-mode dielectric resonator, which was designed by Krupka2) and manufactured by QWED (QWED Inc., Poland), as indicated in **Figure 2-6**. To evaluate the Q-factor due to parasitic losses, the dielectric loss tangents of the substrate and dielectric resonator have to be known. The dielectric loss tangent of the substrate was measured by the split-post dielectric resonator method [3]. A BZT dielectric resonator of 17 mm diameter and of 8 mm height was used in this study. The measurement frequency ranged between 4 and 5 GHz. The electric energy filling factor and geometric factor were rigorously computed using the Rayleigh-Ritz method [4].

Reference

1. C. D. Doyle, “Kinetic Analysis of Thermogravimetric Data,” J. Appl. Polym. Sci., 285 (1961).
2. J. Krupka, IEEE MTT-S Int. Symp. Dig., 2007, p. 515.
3. J. Krupka, R. G. Geyer, J. B. Jarvis, and J. Ceremuga: DMMA’ 96 Conf., Bath, U.K. 23-26 Sept. 1996, p. 21.
4. J. Barker-Jarvis, M. D. Janezic, B. Riddle, C. Holloway, N. G. Paulter, and J. E. Blendell: NIST Tech. Note 1520 (2001).

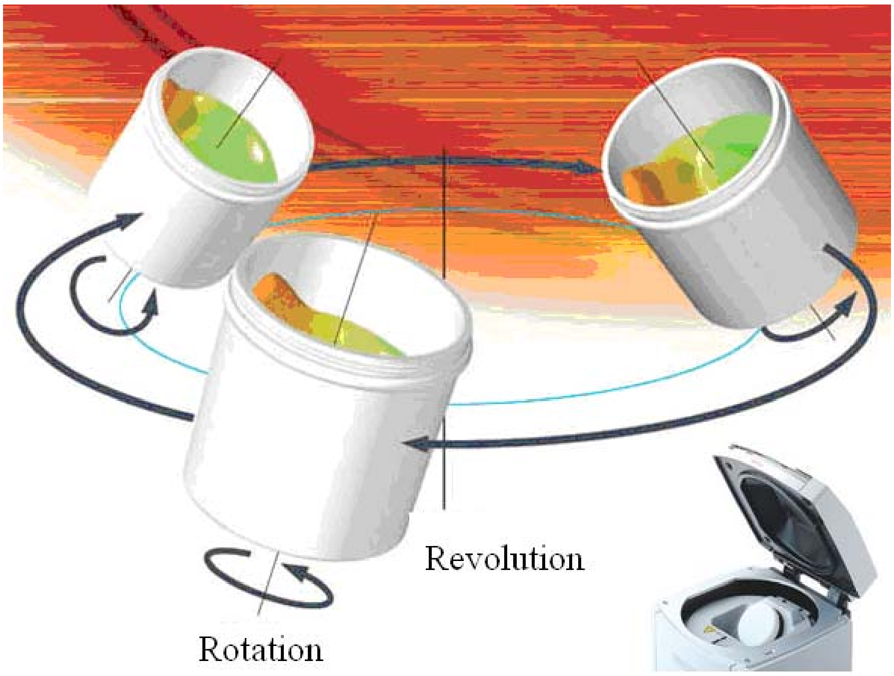

Figure 2-1. The high speed mixer structures.

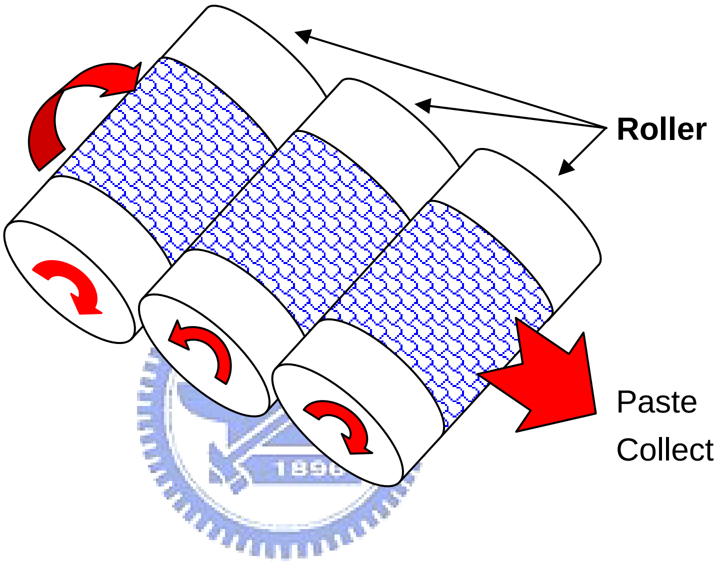

Figure 2-2. The mechanism of triple roller grinding structures.

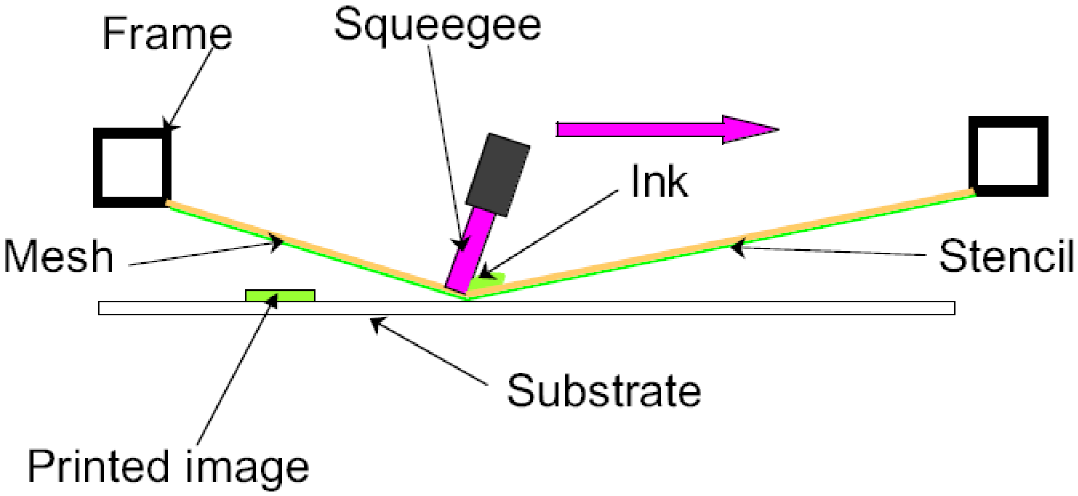

Figure 2-3. The structure chart of screen-printing.

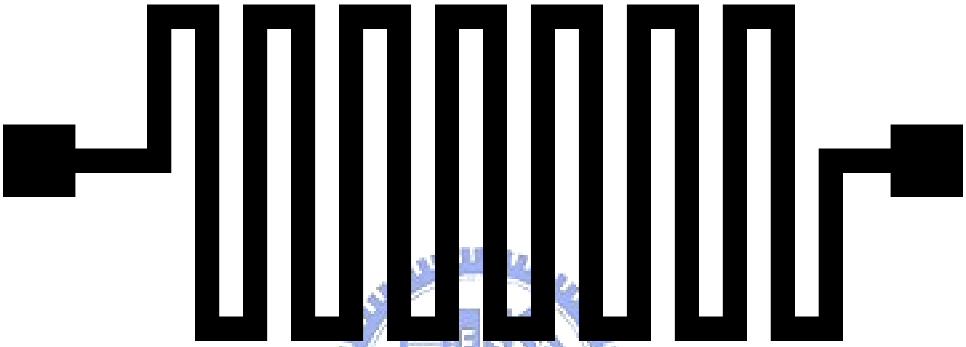

Figure 2-4. The chart of spiral line structure for resistivity measurement.

Figure 2-5. The photo of spiral line structure printing results.

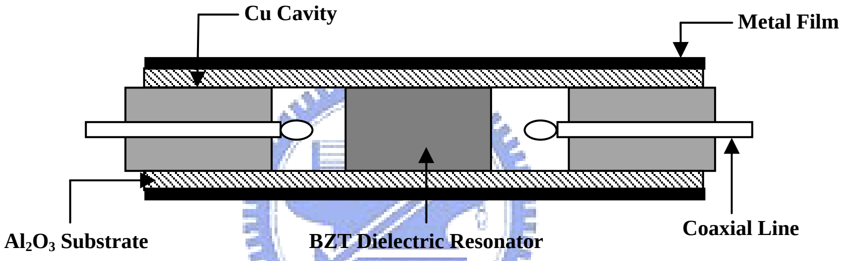

Figure 2-6 Schematic of dielectric resonator

Chapter 3

Effects of Silver Oxalate Additions on the Physical Characteristics of Low-Temperature-Curing MOD Silver Paste for Thick Film Applications

In this Chapter, the effect of silver oxalate addition on physical characteristics of metallo-organic-decomposition (MOD) silver screen-printable paste for thick film technology was investigated. The addition of silver oxalate in the paste not only produces fresh fine silver particles after curing, but also reduces the decomposition temperature of the lubricant coated on the silver flakes. This is an effective route to provide fine silver particles to the paste without significantly changing the rheological behavior. At the curing temperature of 225℃, the resistivity decreases from 180.1 to 31.9$\mu\Omega$-cm, as the silver oxalate content increases from 0 to 10 wt%. This is due to the fact that active silver catalysts produced increase the packing density of silver flakes, and also the removal of lubricant from the surface of silver flakes enhances the electron conduction, thereby decreasing the resistivity of film.

3-1 Introduction

Recently, technologies of common electrical appliances have been tremendously interested in the development of low-cost disposable microelectronic devices on flexible substrates, such as radio frequency identification (RFID) tags, smart cards, and other similar items. In the field of material science, metallizations used for the bonding of devices to the substrate and the interconnections between devices are an important part of the material applications, because they have to provide necessary electrical conduction, wetting on the substrate and structure support. Materials with a high electrical conductivity and a low-temperature and high-speed process were generally required for many flexible electronic applications [1,2]. Among various processing methods, screen printing, electro-photographic printing and ink-jet printing have commonly been used to form precise electrically-conductive patterns by depositing metal particles onto an insulating substrate surface.

Typically, fabricating a conductive layer on substrates requires temperatures less than 350°C for polyimide substrates, 290°C for printed circuit boards (PCBs), and 200°C for other plastics, to prevent any softening or wrapping. Conventional low temperature electrically conductive adhesives (ECA) have several limitations such as relatively low electrical conductivity and unstable contact resistance. Resistivity of the conductive layer such as silver on the substrate is usually 10-50 times that of pure silver, due to the presence of binding organics, which results in more power consumption and signal loss and thus decreasing transmission distance during signal transmission. These shortcomings can be resolved by the use of metallo-organic decomposition (MOD) technology. High conductivity can be achieved at a low temperature by decomposing metallo-organic compounds on various substrates, where the molecular nature of the compounds allows low temperature of conversion to the metal. The MOD-metal flake mixtures have been applied by screen printing [3,4,5] and ink-jet printing process [6,7]. R.W. Vest and coworkers successfully applied ink jet printing system with silver neodecanoate MOD ink for hybrid microcircuits [8]. Recently, very low curing temperature silver inks for used in ink-jet printing were reported [6,7]. The resistivity values of the printed conductive films composed of nano-silver particles were found to have dropped to two or three times the theoretical resisitivity of the bulk silver after heat-treatment at 150°C. The ink-jet printable inks usually have a solid loading of less than 20 wt%, binder content of less than 3 wt% and viscosity of less than 10 cps.

Also, patent literatures have further revealed the technology of MOD combined with metal flake in screen-printable thick film metallizations and terminations, which are then built up with solder or electroplating [3,4]. These techniques have used silver metallo-organic compounds, such as silver neodecanoate MOD compound, with the addition of silver flakes to immobilize it during melting and decomposition. The MOD-metal flake mixture maintains its configuration during heating, and will decompose to form a well-bonded, well-resolved conductor at a temperature compatible to polymer based circuit board substrates. The electrical conductivity is equal to that obtained by conventional thick film conductors sintered at high temperatures (>700°C).

A previous study [5] indicated that silver 2-ethylhexanoate ($C_8H_{15}O_2Ag$) possesses a very low decomposition temperature (190.3°C) among the MOD agents, and it forms silver particles to promote linking among silver flake particles. A low-curing-temperature silver paste with 5 wt% silver 2-ethylhexanoate addition for thick-film applications possesses shear-thinning and thixotropic properties. A resistivity of 7.8×10^{-6} Ω-cm for screen-printed films was obtained after being cured at 250°C for 30 min, which is close to the bulk resistivity of silver [9]. In this study, attempts to modify the curing conditions of MOD silver screen-printable pastes through the addition of silver flakes by silver oxalate ($Ag_2C_2O_4$) were made. The effect of silver oxalate addition on the thermal properties, rheological behavior and curing conditions of the MOD silver paste were investigated. The microstructure and resistivities of screen-printed films on alumina substrate after being thermally treated were characterized and discussed.

3-2 Experiment Procedure

The low-temperature-curing silver pastes used in this study were prepared from silver flake (Ferro, U.S.A.), silver oxalate ($Ag_2C_2O_4$, Rose Scientific Ltd., Alberta, Canada), metallo-organic compound of silver 2-ethylhexanoate (STREM, MA, U.S.A.), and solvent of α-terpineol (TCI, Japan). All materials were mixed by a high-speed mixer (Thinky Mixer) for 3 min and de-bubbled for 1min. Subsequently, uniform pastes were formed using a triple-roller grinder (EXERT, Germany), which causes the breakdown of pigment agglomerates. The weight ratio of silver flake powder and silver 2-ethylhexanoate to solvent was fixed at 81:4:15 (Table I). Also, 1, 3, 5, 10 wt% of the silver oxalate were added, in order to reduce the curing temperature while still retaining a good conductivity of the resultant film. The silver oxalate powders have average particle size (d50) of 1.7 μm as measured by light scattering (HORIBA LA-910).

In order to understand the thermal behavior, the thermogravimetry analysis (TGA; Perkin-Elmer) and differential thermal analysis (DTA; Perkin-Elmer 7) were performed in air at a heating rate of 10°C/min on the pastes as well as pure MOD silver 2-ethylhexanoate and pure silver oxalate. The rheological behaviors of the pastes were explored using a controlled-shear-stress rheometer (HAAKE RS150) with a plate-plate measuring system (35 mm diameter, 0.5 mm gap).

Spiral silver metal lines with a length (l) of 216 cm, a line width (w) of 0.8mm and a line thickness (d) of 20~40 μm were screen-printed on alumina substrate for the resistivity measurement. A Keithely 2400 multimeter with a four-point probe was used to measure the bulk resistance of cured silver paste. The resistivity of the silver conducting line cured at various temperatures was calculated using the relationship $\rho=(R\cdot wd)/l$, in which R is the resistance of the spiral. The microstructures of the films cured at various temperatures and holding times were investigated using a field-emission scanning electron microscope (SEM; JEOL-6500F, Tokyo, Japan).

3-3 Results and Discussion

Figure 3-1 shows the DTA curves for pure MOD silver 2-ethylhexanoate and pure silver oxalate. The thermal decomposition of silver oxalate occurs at a lower temperature than that of silver 2-ethylhexanoate. It manifests that both reactions are exothermic, which generates a relative large amount of heat. The silver oxalate shows an exothermic peak at 229.39°C and the silver 2-ethylhexanoate at 266.25°C. The reactions are as follows:

$$AgC_8H_{15}O_2 + (43/4)O_2 \longrightarrow Ag + 8CO_2 + (15/2)H_2O \qquad (3.1)$$

$$Ag_2C_2O_4 \longrightarrow 2Ag + 2CO_2 \qquad (3.2)$$

Previous study revealed that the thermal treatment of $C_8H_{15}O_2Ag$ results in the formation of various organic species including CH_3, CO, O_2, CH_2CO, CO_2, C_4H_9, CH_5COOH, $C_5H_{10}O$, etc., depending on the temperature and the atmosphere [9]. On the other hand, thermal decomposition of the silver oxalate is different from most oxalates that usually decompose to form a metal carbonate or a metal oxide. It gives rise to silver as the solid product and CO_2 as the gaseous product [10]. The decomposition of the silver oxalate produces nearly 71 wt% of fine silver catalyst, which is certainly a good silver source among various MOD compounds. When the silver 2-ethylhexanoate or silver oxalate was mixed with solvent α-terpineol, the former is soluble in the solvent, but the latter is not. Previous study has shown that the decomposition temperatures of silver 2-ethylhexanoate or silver oxalate in α-terpineol are reduced to 190.3 and 212.14°C, respectively [5].

Figure 3-2 shows the results of the thermogravimetric analysis (TGA) for the pastes without and with 3 wt% silver oxalate added in air. For the paste without silver oxalate added, the decompositions of the α-terpineol and silver 2-ethylhexanoate lead to a weight loss of ≈17.26 wt% at temperatures below 190°C. There is a weight loss of ≈0.3% observed at ≈235°C, which corresponds to the decomposition of the lubricant, fatty acid, coated on the silver flakes. For the paste with 3 wt% silver oxalate added, there are three weight drops as the temperature increases from room temperature to 300°C. Weight loss of ≈16.76 wt% occurs at temperatures below 190°C due to the decompositions of α-terpineol and silver 2-ethylhexanoate, ≈0.87 wt% at ≈210°C resulting from the decomposition of silver oxalate, and ≈0.3% at ≈222°C associated with removal of lubricant from the surfaces of silver flakes. The weight losses observed are relatively consistent with the theoretical values calculated from the paste formulations and the chemical formula of the compounds. The results verify that the addition of the silver oxalate not only produces fresh fine silver particles, but also reduces the decomposition temperature of the lubricant coated on the silver flakes.

Rheological characteristics of the pastes with various amounts of silver oxalate added are shown in **Figure 3-3**. It indicates that all pastes have pseudoplastic flow (shear-thinning) property [**Figure 3-3(a)**]. The solid loading of the paste increases with the silver oxalate content since it is not soluble in the α-terpineol. However, the viscosity of the paste only slightly increases with the content of silver oxalate. **Figure 3-3(b)** indicates that all pastes possess pseudoplastic flow property with an apparent yield point, which is beneficial to the dimensional control during screen printing process. The apparent yield point does not vary with the content of silver oxalate. Based on the paste formulations shown in **Table 3-1**, the total silver content in the paste slightly decreases from 82.74 to 81.67 wt% as the content of the silver oxalate increases from 0 to 10 wt%. Whereas, the ratio of the fresh fine silver particles, decomposed from the silver oxalate and silver 2-ethylhexanoate, would increase from 1.74 to 8.03 wt% of the total paste. This is an effective route to provide fine silver particles to the paste without significantly changing the rheology of the paste. Direct addition of a small quantity of nano-size silver particles in the paste would significantly increase the viscosity of the paste to an un-acceptable value and easily leads to agglomeration of the silver particles.

Figure 3-4 shows the SEM micrographs of the films, prepared from the pastes with 0, 3, and 10wt% of silver oxalate additions, after being cured for 5 min at 225°C. The films generally contain silver grains with a wide size distribution. They indicate that a higher amount of silver oxalate added produces a higher packing density of film. Fine silver particles, produced from the decomposition of silver oxalate and silver 2-ethylhexanoate, occupied the voids among silver flakes. This will enhance the connectivity of the silver particles in the film, as shown in **Figures 3-4(b)** and **3-4(c)**.

Figure 3-5 shows the resistivities of silver films prepared from the pastes with various amounts of silver oxalate added and cured at different temperatures for 5 min. The film resistivity generally decreases with increasing curing temperature, due to a better connectivity of the metal particles associated with the decomposition of organics. The resistivity decreases with increasing silver oxalate content for the films cured at temperatures less than 250°C. At the curing temperature of 225°C, the resistivity decreases from 180.1 to 31.9 μΩ-cm, as the silver oxalate content increases from 0 to 10 wt%. There are two contributions which are responsible for lowering the resistivity of the films. One is that the fresh fine silver particles in the cured silver film increases from 2.10 to 10.17% wt% of the total silver, due to the decomposition of MOD compounds, as the silver oxalate content raises from 0 to 10 wt%. (**Table 3-1**). The other contribution is from the addition of the silver oxalate in the paste that reduces the thermal-decomposition-temperature of the lubricant, fatty acid, coated on the silver flakes. The thermal decomposition of silver oxalate and silver 2-ethylhexanoate produces active silver catalysts, which increase the packing density and assist the necking of silver flakes in the films. The removal of the lubricant from the surfaces of silver flakes would increase their connectivity. These would be beneficial to the electron conduction and thus decrease the resistivity of the film. For the curing temperature above 250°C, the resistivities of the films are very similar and range from 10.18 to 15.03 μΩ-cm, since there are no organic residues left and the connectivity of the silver particles gets to a saturation limit. The resistivity is insensitive to the increasing curing temperature, unless it reaches the sintering temperature of silver particles.

3-4 Summary

In this study, MOD silver screen-printable pastes with various amounts of silver oxalate added were prepared. With the addition of silver oxalate, the decompositions of α-terpineol and silver 2-ethylhexanoate occur at temperatures below 190°C, the silver oxalate at ≈210°C, and the lubricant on the surfaces of silver flakes at ≈222°C. The resistivity of the film prepared from the pastes decreases with increasing curing temperature, due to a better connectivity of the metal particles associated with the decomposition of organics. A resistivity of 31.9 μΩ-cm was obtained for the film prepared from the paste with 10 wt% silver oxalate added and curried at 225°C.

References

1. D. Redinger, S. Yin, R. Farschi and V. Subramanian: IEEE. Trans. Electron. Devices. 51 (2004) No. 12, 1978.
2. V. Subramanian, J. M. J. Frechet, P. C. Chang, D. C. Huang, J. B. Lee, S. E. Molesa, A. R. Murphy, D. R. Redinger, S. K. Volkman: Proc. IEEE. **93** (2005) No. 7, 1330.
3. P. H. Kydd: United States Patent, No. 6,036,889 (2000).
4. P. H. Kydd: PCT Patent, WO 98/37133 (1998).
5. C. A. Lu, P. Lin, H. C. Lin and S. F. Wang: Jpn. J. Appl. Phys. 45 (2006), 6987.
6. A.L. Dearden, P.J. Smith, D.Y. Shin, N. Reis, B. Derby, and P. O’Brien: Marcromol. Rapid Commun. 26 (2005) 315.
7. D. Kim, and J. Moon: Electrochemical and Solid State Letters, 8 (2005) J30.
8. K. F. Teng and R. W. Vest: IEEE. Trans. Components. Hybrid. and Manufacturing. V CHMT-12 (1987) No. 4, 545.
9. C. A. Lu, P. Lin, H. C. Lin and S. F. Wang: Jpn. J. Appl. Phys. 46 (2007), 251.
10. V. V. Boldyrev: Thermochimica Acta. 388 (2002), 63.

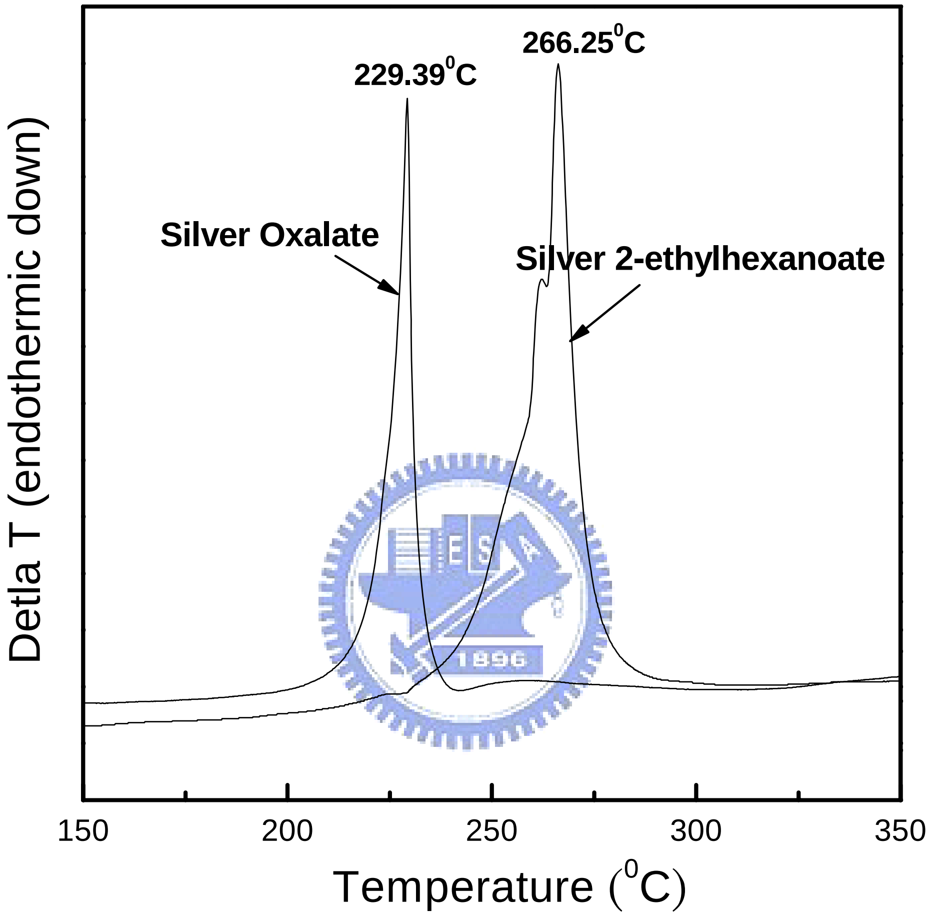

Figure 3-1. DTA curves for pure silver 2-ethylhexanoate and pure silver oxalate.

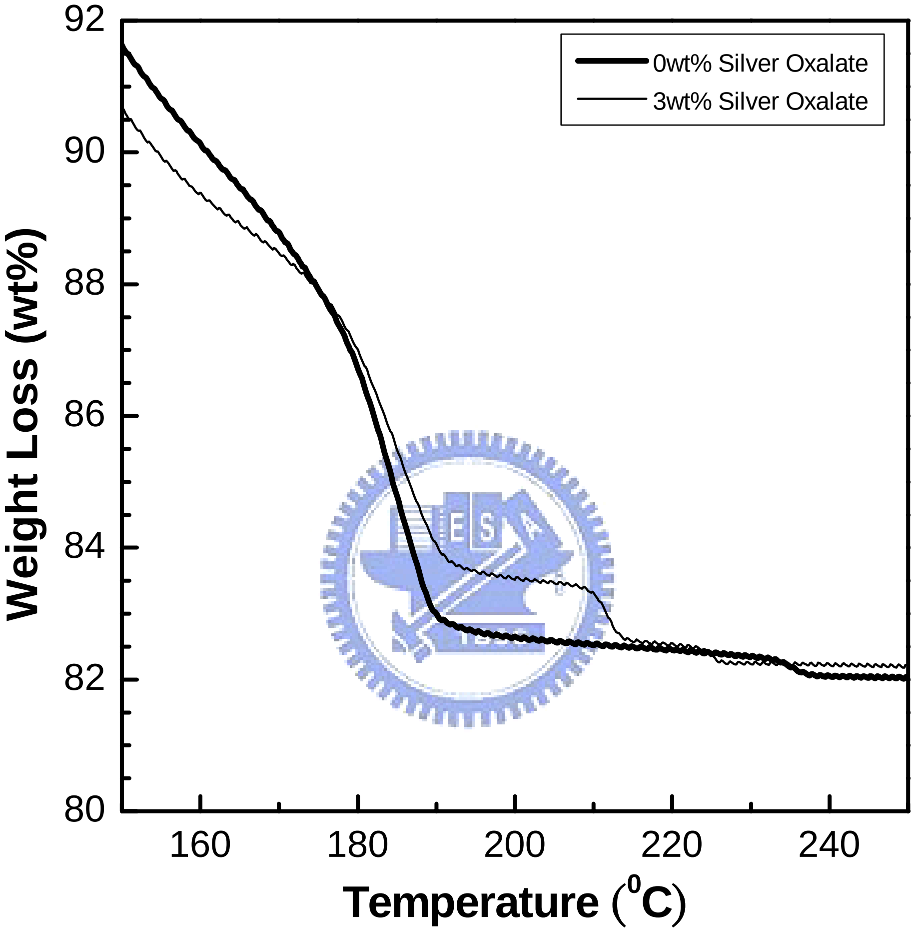

Figure 3-2. TGA curves for the pastes with 0 and 3wt% silver oxalate additions.

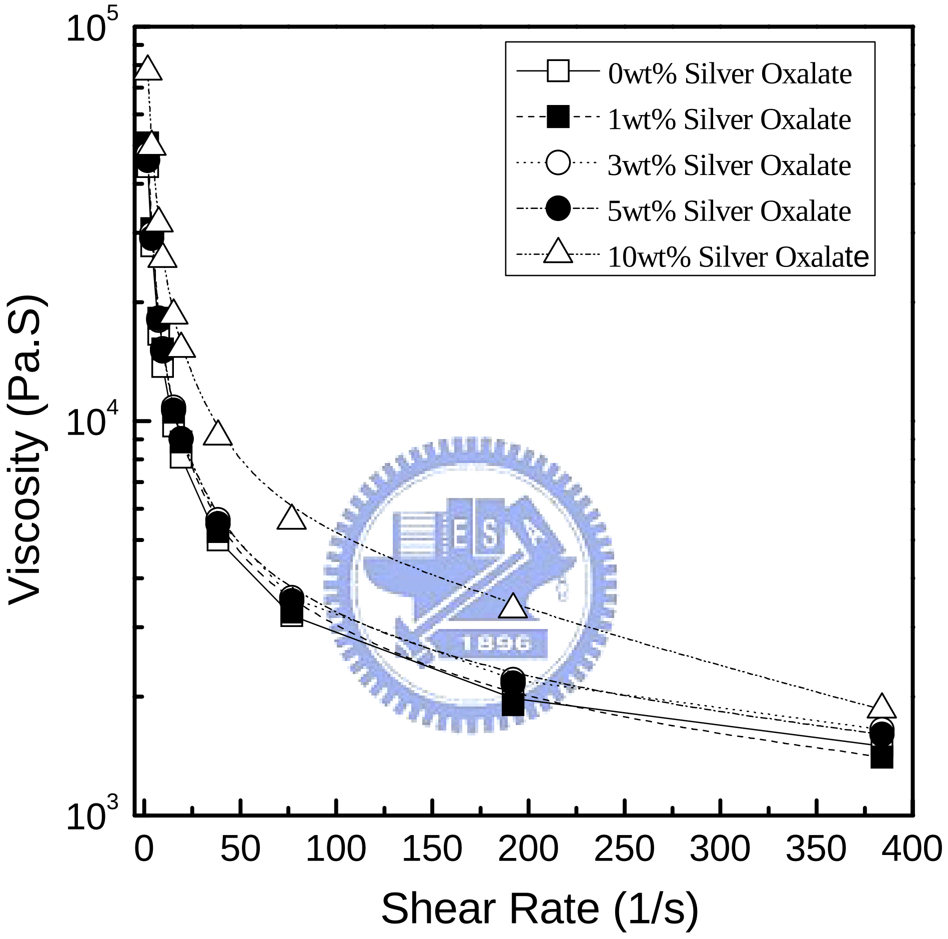

Figure 3-3(a). Rheological properties of the pastes with various amounts of silver oxalate added.

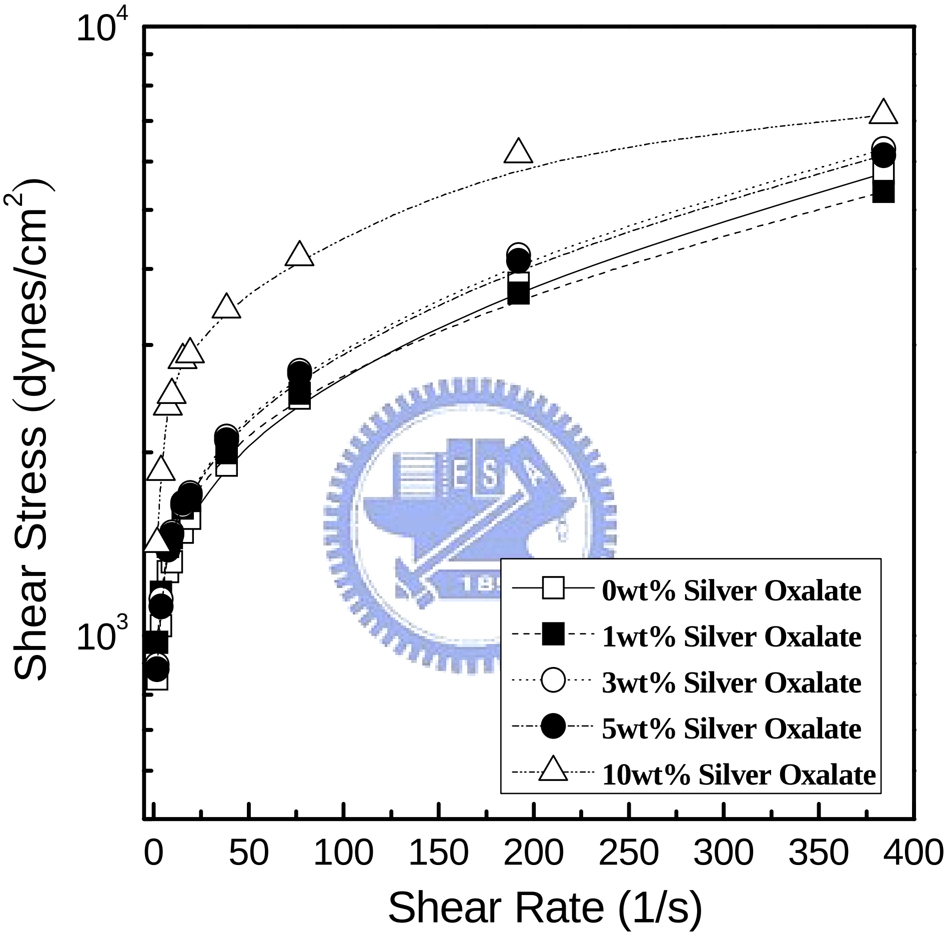

Figure 3-3(b). Rheological properties of the pastes with various amounts of silver oxalate added.

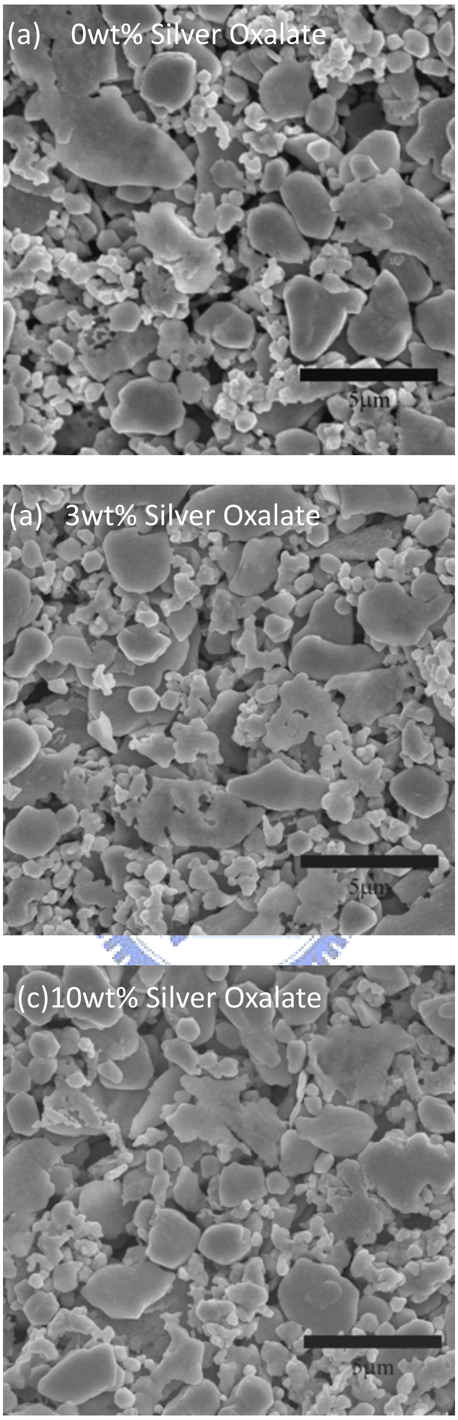

Figure 3-4. SEM micrographs of the silver films prepared from the pastes with (a) 0 wt%, (b) 3 wt%, and (c) 10 wt% silver oxalate added and cured at 225°C for 5 min.

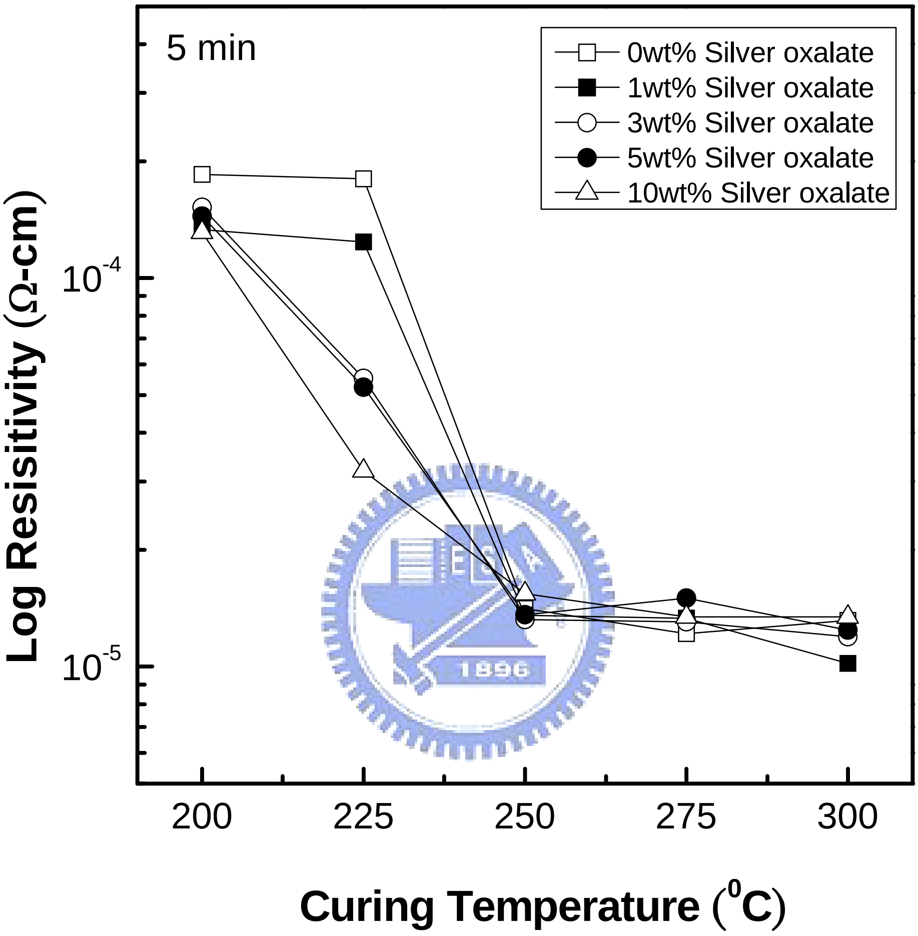

Figure 3-5. Resistivity of silver films prepared from the pastes with various amounts of silver oxalate added and cured at various temperatures for 5 min.

Table 3-1. Formulations of the pastes prepared in this study

Paste No.	Paste Formulation (wt%)			Addition of Silver Oxalate (wt% of paste)	Final Paste Formation (wt%)				Silver Content in Paste (wt%)
	Silver Flake	α-terpineol	Silver 2-ethylhexanoate		Silver Flake	α-terpineol	Silver 2-ethylhexanoate	Silver Oxalate	
1	81.00	15.00	4.00	0	81.00	15.00	4.00	0	82.74
2	81.00	15.00	4.00	1.00	80.20	14.85	3.96	0.99	82.62
3	81.00	15.00	4.00	3.00	78.64	14.56	3.88	2.91	82.35
4	81.00	15.00	4.00	5.00	77.14	14.28	3.81	4.76	82.17
5	81.00	15.00	4.00	10.00	73.64	13.64	3.64	9.09	81.67

Chapter 4

Microstructure and Electrical Resistivity of Low -Temperature-Cured Silver Films Prepared with Silver Oxide and Silver Stearate Pastes

In this Chapter, paste formulations containing silver oxide coated with MOD (metallo-organic decomposition) agent of silver stearate were prepared without the use of any silver powders or silver flakes. Results indicate that all pastes appear to have a pseudoplastic flow property which is acceptable for roll-to-roll printing and screen printing. The pastes were screen-printed on alumina substrate and then thermally treated in a range of temperatures. The lowest electrical resistivity of 13.2×10^{-6} *Ω-cm was obtained for the film prepared from paste with the* Ag_2O*/silver stearate ratio of 100:5 at a solid loading of 80wt% in solvent α-terpineol, after being cured at 160℃ for 5min, which meets the requirements of low-temperature and high speed manufacturing for practical applications. The low resistivity of the film is facilitated by the combination of the* Ag_2O *and silver stearate added in the paste.* Ag_2O *produces a high density of silver matrix after being reduced at low temperatures and the presence of silver stearate contributes to the rheological behavior of the paste after dissolution in the solvent. Co-existence of the* Ag_2O *and silver stearate induces their simultaneous transformation to the silver form at temperatures below 160℃.*

4-1 Introduction

Flexible electronics is emerging as a multidisciplinary research topic with far-reaching impact in a number of research areas, including flat-panel displays, organic electronics and distributed macroelectronic systems and architectures. To develop flexible electronics, each component must tend towards a low-temperature process, adhesion to polymer-based substrates, low-cost and high-speed manufacturing, and high performance. Screen printing, electro-photographic printing and ink-jet printing have been used to form precise electrically-conductive patterns by depositing metal particles onto an insulating substrate surface. In particular, screen printing and ink-jet printing have been used for printing the antennas in RFID (Radio Frequency Identification) tags [1].

Most commercial conductive pastes designed for various printing processes are formulated using the conducting metal particles dispersed in a resin or solvent. The conductive pastes are mainly classified into two types, namely the firing type conductive paste and resin type conductive paste. The former has glass as binder, which develops conductive film when heated to a temperature ranging from 500 to 900°C. The latter contains a resin as binder and vehicle, which requires only a low temperature curing process to form a continuous film. However, glasses and resins are generally nonconductive, which may hinder the contacts of metal powders and reduce the electron transmission. Recently, there has been a tremendous interest in low-curing-temperature conductive pastes, which have no glass or resin as addition, but manufactured in a low-cost and at high speed for flexible electronic applications.

Conventional low-curing-temperature pastes have several limitations, such as relatively low electrical conductivity and unstable contact resistance. Several approaches were proposed to overcome these obstacles. The first is the use of a suspension of metal nanoparticles. The small size of the nanoparticles results in a considerably lower melting point relative to their bulk-material counterparts

[2]. After a printing process, the metallic nanoparticles can subsequently be sintered at a plastic-compatible temperature. Second is use of metals with lower melting point which form interconnections between metal particles. Another approach is the use of metallo-organic decomposition (MOD) technology. High-conductivity metal films can be achieved at a low temperature by decomposing metallo-organic precursors on various substrates, where the molecular nature of the compounds allows a low-temperature conversion to metal. K. F. Wang employed the MOD inks to metallization of solar cells [4]. Teng and Vest successfully applied an ink-jet printing system with silver neodecanoate MOD ink to hybrid microcircuits [5]. Lu et al. utilized a silver paste comprising silver flakes, inorganic salt of silver oxalate ($Ag_2C_2O_4$) and organic acidic salt of silver 2-ethylhexanoate ($C_8H_{15}O_2Ag$) for forming a conductive film on the substrate at a relatively low temperature [3,6]. The MOD-metal flake mixture maintains its configuration during heating, and will decompose to form a well-bonded, well-resolved conductor at a temperature compatible to polymer based circuit board substrates. The electrical conductivity is equal to that obtained by conventional thick film conductors sintered at high temperatures (>700°C).

High density and high conductivity metal layers can also be achieved at a low temperature by thermal reduction of silver oxide with various reducing agents [7]. Silver oxide has been studied extensively for the applications in electrical, optical and magneto-optical data storage industries [8,9]. A previous study [13] indicated that MOD silver pastes with partial substitution of silver flake by Ag_2O and AgO enhances the connectivity and packing density of the silver flakes, and thus increases the electrical conductivity of the films. Resistivity of 14×10^{-6} Ω-cm, was achieved for MOD paste with 20wt% Ag_2O additions after being cured at 200^0C for 5min. However, for the flexible PET substrate, the curing process of pastes has to be proceeded at temperatures of no more than 170^0C, and the resultant film has to possess a low electrical resistivity

[14]. Also, our previous study [15] showed that silver stearate, a salt derived from stearic acid, can easily wet the silver flake powders and distribute itself uniformly between the metal or oxide powder. In this chapter study, paste formulations containing silver oxide coated with various amounts of MOD agent silver stearate ($Ag(O_2C(CH_2)_{16}CH_3)$) were prepared without the use of silver powders or silver flakes. The prepared pastes were screen-printed on alumina substrate and then thermally treated in a range of temperatures. The microstructures and electrical properties of the resultant films were characterized and discussed.

4-2 Experiment Procedure

The low-curing-temperature silver pastes used in this study were prepared from commercially available silver (I) oxide (99.99%, American Elements, LA, U. S. A.), the MOD compound silver stearate [$Ag(O_2C(CH_2)_{16}CH_3)$; GROTTO, CA, U.S.A.], and the solvent α-terpineol (TCI, Japan). Ag_2O powders have an average particle sizes (d_{50}) of 2.35 μm, measured by light scattering (HORIBA LA-910, U.S.A.). First, different weight ratios of Ag_2O and silver stearate (100:3; 100:4; 100:5; and 100:6) were mixed using dry ball-milling for 24 hr. Then the silver stearate coated silver oxide powders were mixed with solvent α-terpineol using a high-speed mixer (Thinky Mixer, Japan) for 3min and de-bubbled for 1min. The weight ratio of silver stearate coated Ag_2O powders to solvent was fixed at 70wt%, 75wt% and 80wt%. Formulations of low-curing-temperature silver pastes prepared in this study are listed in **Table 4-1**.

To understand the thermal behavior, the thermogravimetric analysis (TGA; Perkin-Elmer) on the various amount of silver stearate coated Ag_2O powders and the paste samples of different solid loadings were performed in air at a heating rate of 10°C/min. X-ray diffraction (XRD; Rigaku DMX-2200) using monochromated Cu-Ka radiation was performed for the phase identification of the films after heat treatment. Rheological behaviors of the pastes with solid content of 70wt%, 75wt% and 80wt% were explored using a HBT model viscometer (Brookfield DV-II, U. S. A.) with “40” spindle.

Silver metal lines with a length (l) of 10cm, a line width (w) of 2-4mm, and a line thickness (d) of 20-40μm were manually printed on the alumina substrate for the resistivity measurement. A keithley 2400 multimeter with a four-point probe was used to measure the bulk resistance of cured silver paste. The resistivity (ρ) of the silver conducting line cured at various temperatures was calculated using the relationship $\rho = (R \cdot w \cdot d)/l$, in which R is the resistance of the line. α-step was used to measure the line morphology with line width (w) and line thickness (d). The microstructure of the pure Ag_2O powder, coated powders, and films being cured at various thermal profiles was investigated using a field-emission scanning electron microscope (SEM; S4500, Hitachi, Japan) and a transmission electron microscopy (TEM; Tecnai F20, Philips).

4-3 Results and Discussion

The thermal decomposition behaviors of mixtures containing α-terpineol, Ag_2O or silver stearate, characterized using the TGA, are shown **Figure 4-1**. For the mixture of 70 wt% α-terpineol and 30 wt% Ag_2O, a significant weight loss was observed below 189°C and then the sample's weight levels off at 28.3 wt% of its original weight, which is close to the theoretical weight percentage taking account of the evaporation of α-terpineol and the reduction of Ag_2O to silver. It appears that Ag_2O can catalyze the decomposition of the α-terpenol solvent, which is identical with the results indicated in a previous study [13]. For the TGA trace of 70 wt% α-terpineol and 30 wt% silver stearate, there are three regions with significant weight loss, including ≈ 70 wt% weight loss below 198°C due to the evaporation of α-terpineol and then totally ≈ 22 wt% weight loss in the temperature range from 198°C to 380°C resulting from the thermal decomposition of silver stearate. Above 380°C, there is no additional weight loss, which reveals that all silver compounds were transferred to silver. For the mixture of 70 wt% α-terpineol, 20 wt% Ag_2O, and 10 wt% silver stearate, ≈ 72.2 wt% weight loss was observed below 189°C, which is corresponding to the combination of the evaporation of 70 wt% α-terpineol, the reduction of 20 wt% Ag_2O, and the decomposition of 1.1 wt% silver stearate. The remaining 8.9 wt% silver stearate was further decomposed at temperatures above ≈ 240°C. No weight loss was observed at temperatures higher than 260°C. Apparently Ag_2O can catalyze the decomposition of silver stearate, including 1.1 wt% below 189°C and the rest between 189 and 260°C. Calculations based on the above result indicates that 100 grams of Ag_2O can catalyze the decomposition of ≈ 5.5 gram silver stearate at temperatures below 189°C, however, the weight ratio for the reaction between Ag_2O and silver stearate is dependent on the physical characteristics of the Ag_2O powders, such as particle size.

Figure 4-2 shows the TGA traces of Ag_2O, silver stearate, and Ag_2O with 5 wt% silver stearate. Without the presence of α-terpineol, Ag_2O will not get reduced until the temperature reaches 370°C. Thermal decomposition path of pure silver stearate is similar to that observed in the mixture α-terpineol and silver stearate, as shown in **Figure 4-1**. It is evident that the presence of α-terpineol promotes the reduction of Ag_2O but not the decomposition reaction of silver stearate. For the Ag_2O with 5 wt% silver stearate, ≈ 7.8 wt% rapid weight loss was observed at ≈ 160°C, which corresponds to the transfer of silver compounds to pure silver (89.9 % of the original weight theoretically). XRD analysis on the sample after being heat-treated at 160°C indicates that silver and small amount of Ag_2O are present in the residue. It manifests that Ag_2O not only catalyzes the decomposition of silver stearate but also the decomposed silver induces the reduction of Ag_2O concurrently, which confirms the observation in **Figure 4-1**. Not all Ag_2O was reduced to silver. The Ag_2O residue was transferred back to silver at temperatures higher than 410°C, which is coincident with that observed in the literature.

In order to determine the optimum ratio of the Ag_2O/ silver stearate, TGA studies on the silver oxide with additions of 3, 4, 5, and 6 wt% silver stearate were performed and the results are shown in **Figure 4-3**. Similar to the decomposition behavior of Ag_2O/silver stearate shown in **Figure 4-2**, the mixtures reduce their weights dramatically at the temperatures ranging from 155 to 160°C, and Ag_2O residues reduce back to silver at temperatures higher than 410°C. Increasing the amount of silver steartae addition, the weight loss increases due to the complete decomposition of silver stearate and partial reduction of Ag_2O. As more fresh silver decomposed from silver stearate, more Ag_2O was catalyzed and reduced back to silver. Comparing the weight loss at 165°C for samples with 5 and 6% stearate, ≈0.2 wt% difference in weight loss seen corresponds to the decomposition of silver stearate. No additional reduction of Ag_2O was observed. Therefore, it can be concluded that for the silver stearate content exceeding 5 wt%, the weight loss at temperatures below 160°C corresponding to the reduction of Ag_2O does not increase.

In this study, the silver flake and binder such as ethyl cellulose were replaced by Ag_2O and silver stearate in the paste, to reduce the curing temperature while maintaining the required paste characteristics and electrical properties of the final film. Rheological behaviors of the pastes with solid loading of 70wt% and 80 wt% are characterized and the results are shown in **Figures 4-4 (a) and (b)**, respectively. It was elucidated in such a way that shear stress versus shear rate for various ratios of Ag_2O and silver stearate are calculated. The results indicate that all pastes appear to have pseudoplastic flow (shear-thinning) property. The initial shear stress and viscosity increases with increasing silver stearate content and the solid loading. The dissolution of silver stearate in solvent raised the viscosity of the paste significantly. It is similar to that observed in the typical isotropically conductive adhesive (ICA) formulations, in which stearic acids are widely used as the rheology modification agent or lubricant layer on the surfaces of metal powders, to modify the viscosity of conductive adhesive paste [16]. For the paste with 80wt% solid loading, the pastes with 5 and 6 wt% silver stearate show shear-thinning with an apparent yield point. The dissolution of silver steatrate in solvent leads to viscoelasticity properties with a stable viscosity and shear stress versus shear rate, which is acceptable for high shear rate applications, such as roll-to-roll printing and screen printing [3].

Figures 4-5(a) and 4-5(b) show the electrical resistivities of silver films prepared from the pastes with solid loadings of 70, 75 and 80 wt%, after being cured at 160°C for 5min and 10min, respectively. The film resistivity decreases with increasing the ratio of Ag_2O/ silver stearate up to 100:5 and then increases again with the content of silver stearate. Increasing the soaking time from 5 min to 10 min does not change the resistivity significantly. The electrical resistivity decreases with the solid loading, which is due the higher packing density of the conducting particles after being cured. The electrical resistivity of the films prepared from pastes with the Ag_2O/silver stearate ratio of 100:5, at solid loading of 70, 75, and 80wt% are 24.3×10^{-6} Ω-cm, 16.9×10^{-6} Ω-cm, and 13.2×10^{-6} Ω-cm, respectively, after being cured at 160°C for 5min, which meets the requirements of low-temperature and high speed manufacturing for practical applications. The electrical resistivity of the film depends on the connectivity and film density of various species in the film. As the paste is heated, Ag_2O catalyzes the decomposition of silver stearate and, simultaneously, undergoes reduction and transforms to silver particles, which may be catalyzed by the fresh fine silver particles formed on their surfaces. Reduction of Ag_2O and thermal decomposition of silver stearate proceed with time during curing which decreases the resivitivity of the films. Residual Ag_2O was found in XRD results of the films after being cured at 160°C, as shown in **Figure 4-6**. It is evident enough that the reduction reaction of Ag_2O does not proceed to completion, and leads to a small quantity of Ag_2O still remaining after thermal curing. The incomplete reduction reaction of Ag_2O retards further reduction of resistivity of silver films.

Ag_2O catalyzes the evaporation of α-terpineol and the decomposition of silver stearate, which decreases the curing temperature of films to 160°C and shortens the soaking time to 5min. At a lower content of silver stearate (Ag_2O/silver stearate = 100:3), the insufficient fine silver particles decomposed from silver stearate leads to a higher resistivity. At a higher content of silver stearate (Ag_2O/silver stearate = 100:6), the extra silver stearate could not further induce the reduction of Ag_2O during curing and, also, the high viscosity of the paste due to the dissolution of silver stearate in the solvent reduces the packing density (**Figures 4-4 and 4-5**). Therefore, higher electrical resistivity was obtained for Ag_2O/silver stearate ratios of 100:3 and 100:6 after being cured.

SEM micrographs of the films, prepared from the pastes with various Ag_2O/silver stearate ratios at solid loading of 80wt%, after being cured at 160°C for 10 min are shown in **Figure 4-7**. They indicate that the linkage of silver particles from the thermal decomposition of silver stearate and the reduction of Ag_2O results in high electrical conductivity of films after being cured. For the Ag_2O/silver stearate ratio of 100/5, the microstructure seems to have the highest film density, which is coincident with the lowest electrical resistivity of films shown in **Figure 4-5**. SEM cross-section micrograph of the films shown in **Figure 4-8** shows the interconnection of the silver grains that contributes to the low electrical resistivity. Upon carefully examining the microstructure of the films, it appears that the three-dimensional interconnection network has resulted from the coalescence of fine and fresh silver particles decomposed from silver stearate and neckgrowth of the coarse silver grains reduced from Ag_2O. TEM micrograph (**Figure 4-9**) shows the nano silver particles coated on the surfaces of silver grains, which were reduced from Ag_2O. Left-top (a) diffraction pattern corresponds to the silver from the reduction of Ag_2O and the right-down ring diffraction pattern is due to the silver from the decomposition of silver stearate. Small silver particles are formed from decomposition of silver stearate catalyzed by Ag_2O, which are then adhered onto the surfaces of silver grains that are also simultaneously reduced from Ag_2O. Neckgrowth and sintering of silver particles shown in the TEM micrograph illustrates the low electrical resistivity of films after being cured. The low resistivity of the film is facilitated by the combination of the Ag_2O and silver stearate contained in the paste used. Ag_2O consists of high silver constituent (100 grams of Ag_2O produces 93.1 grams silver), which produces a high density of silver matrix after reduction at low temperatures. The presence of a small amount of silver stearate contributes to the rheological behavior of the paste due to its dissolution in the solvent. More importantly, the co-existence of the Ag_2O and silver stearate induces their transformation to the silver form simultaneously at temperatures below 160°C.

4-4 Summary

In this study, the silver flake and binder in the paste were replaced by Ag_2O and silver stearate, to reduce the curing temperature while maintaining the required paste characteristics and electrical properties of the final film. Results indicate that all pastes appear to have pseudoplastic flow (shear-thinning) property. The initial shear stress and viscosity increases with increasing the silver stearate content and the solid loading. As the paste is heated, Ag_2O catalyzes the decomposition of silver stearate and, simultaneously, undergoes reduction and transforms to silver particles. The lowest electrical resistivity of $13.2x10^{-6}$ Ω-cm was obtained for the film prepared from paste with the Ag_2O/silver stearate ratio of 100:5 at a solid loading of 80wt% in solvent α-terpineol, after being cured at 160°C for 5min. The three-dimensional interconnection network was resulted from the coalescence of fine silver particles decomposed from silver stearate and neckgrowth of the coarse silver grains reduced from Ag_2O. Ag_2O catalyzes the evaporation of α-terpineol and the decomposition of silver stearate, which decreases the curing temperature of films to 160°C and shortens the soaking time to 5min.

References:

1. D. Redinger, S. Yin, R. Farschi and V. Subramanian: IEEE. Trans. Electron. Devices. 51 (2004) No. 12, 1978.
2. V. Subramanian, P. C. Chang, J. B. Lee, A. R. Murphy, D. R. Redinger and S. K. Volkman: Proc. IEEE 93 (2005) 1330.
3. C. A. Lu, P. Lin, H. C. Lin and S. F. Wang: Jpn. J. Appl. Phys. 46(1) (2007) 251.
4. K. F. Teng and R. W. Vest: IEEE. Trans. Components Hybrids Manuf. 11 (1988) 291.
5. K. F. Teng and R. W. Vest: IEEE. Trans. Components Hybrids Manuf. 10 (1987) 545.
6. C. A. Lu, P. Lin, H. C. Lin and S. F. Wang: submitted to Microelectronic Engineering (2007).
7. T. Honda: U. S. Patent 20040248998 A1 (2004).
8. J. Passaniti, S. A. Megahed, in: D. Linden (Ed.), Handbook of Batteries, 2nd ed, McGraw-Hill, New York, 1995, p. 122.
9. D. F. Smith, G. R. Graybill, R. K. Grubbs, J. A. Gucinskl: J. Power. Sources 65 (1997) 47.
10. O. Knacke, O. Kubaschewski, K. Hesselmann (Eds.), Thermal Properties of Inorganic Substances, Springer, 1991, p. 11.
11. B. V. L'vov: Thermochim. Acta. 13 (1999) 333.
12. W. A. Parkhurst, S. Dallek, and B. F. Larrick: J. Electrochem. Soc. 131 (1986) 2451.
13. C. A. Lu, P. Lin, H. C. Lin and S. F. Wang: Jpn. J. Appl. Phys. 46(7A) (2007) 4179.
14. D. Huang, F. Liao, S. Molesa, D. Redinger and V. Subramanian: J. Electrochem. Soc. 150 (2003) G412.
15. C. A. Lu, P. Lin, H. C. Lin and S. F. Wang: Jpn. J. Appl. Phys. 45(9A) (2006)

6987.

16.D. Lu and C. P. Wang: J. Therm. Analy. Calor. 61 (2000) 3.

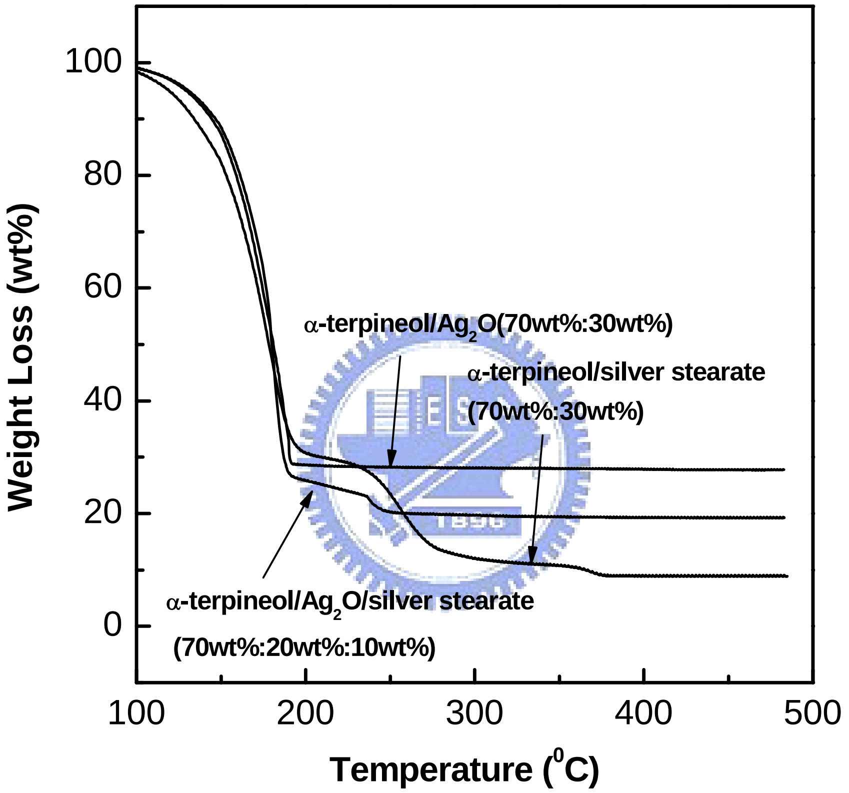

Figure 4-1. TGA results of pastes prepared from various alpha-terpineol/Ag_2O/silver stearate ratios.

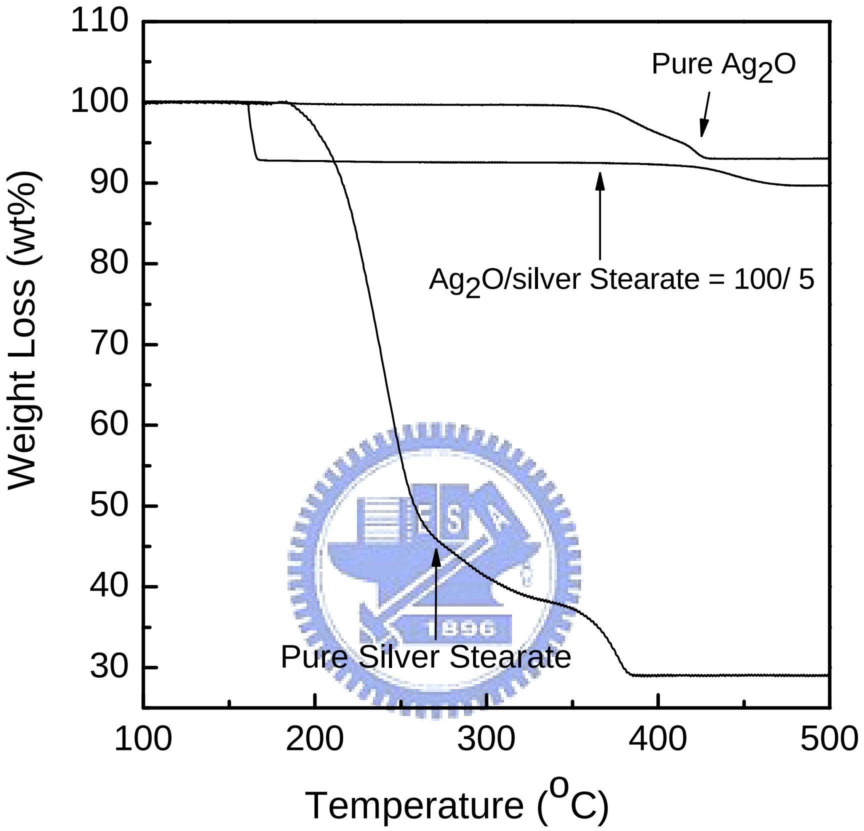

Figure 4-2. TGA results of the pure silver oxide, pure silver stearate, and silver-stearate-coated Ag_2O (100:5).

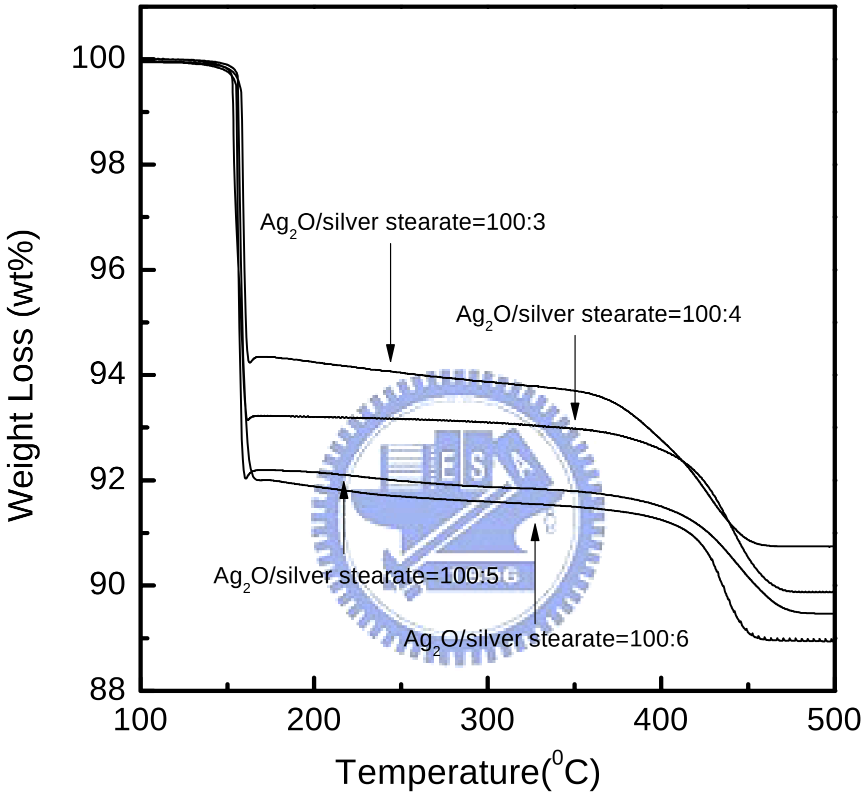

Figure 4-3. TGA results of the coated powder of Ag_2O with silver stearate at various ratios.

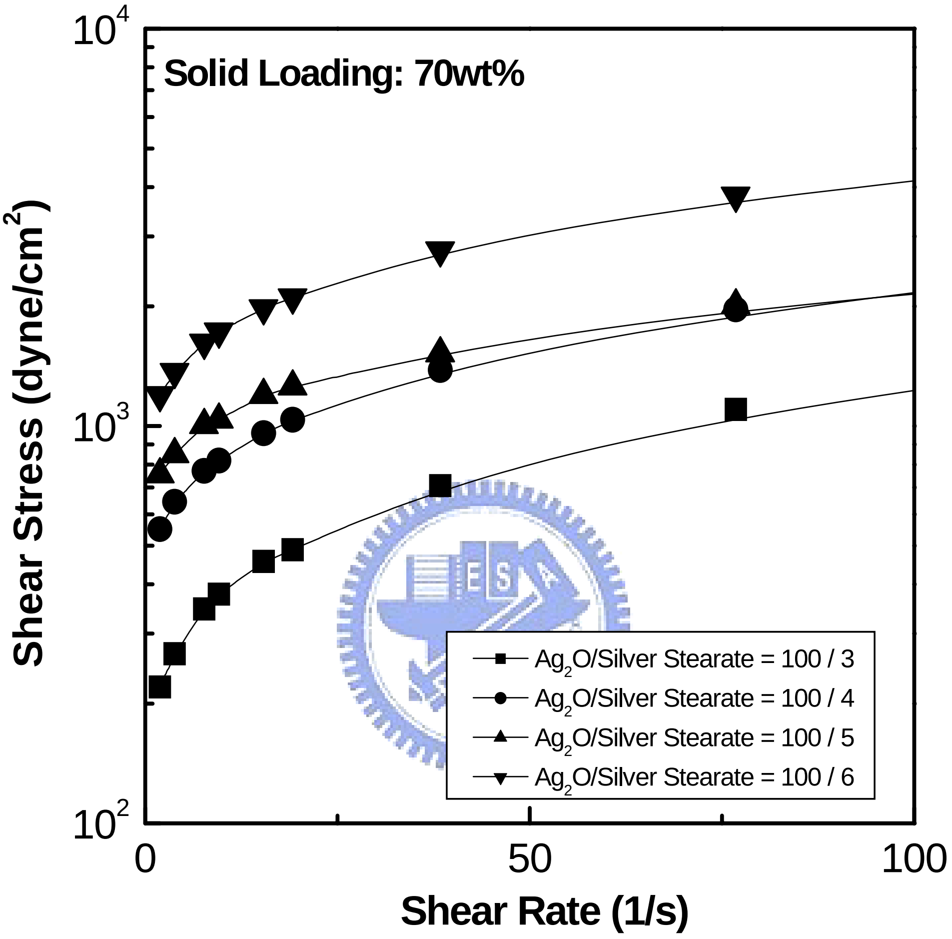

Figure 4-4(a). Rheological behaviors of pastes with various ratios of Ag_2O and silver stearate at a solid loading of (a) 70wt% and (b) 80wt%.

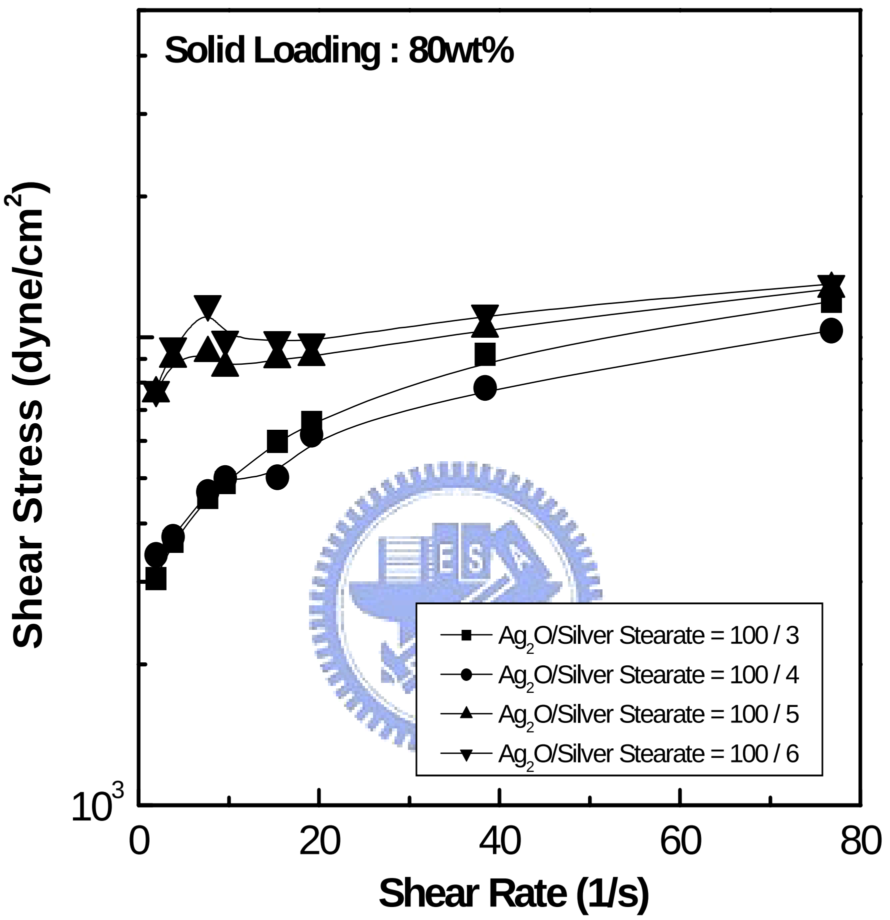

Figure 4-4(b). Rheological behaviors of pastes with various ratios of Ag_2O and silver stearate at a solid loading of (a) 70wt% and (b) 80wt%.

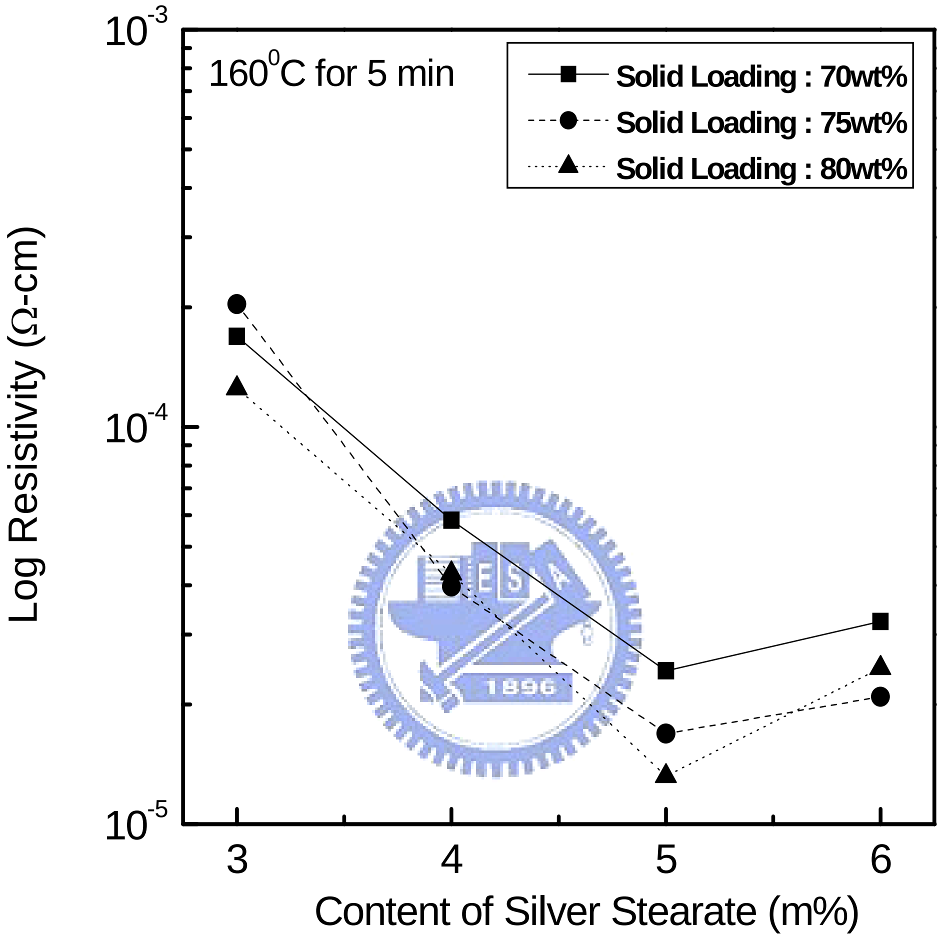

Figure 4-5(a). The electrical resistivities of silver films prepared from the pastes with various Ag_2O/silver stearate ratios and solid loadings, after being cured at 160°C for (a) 5 min and (b) 10min.

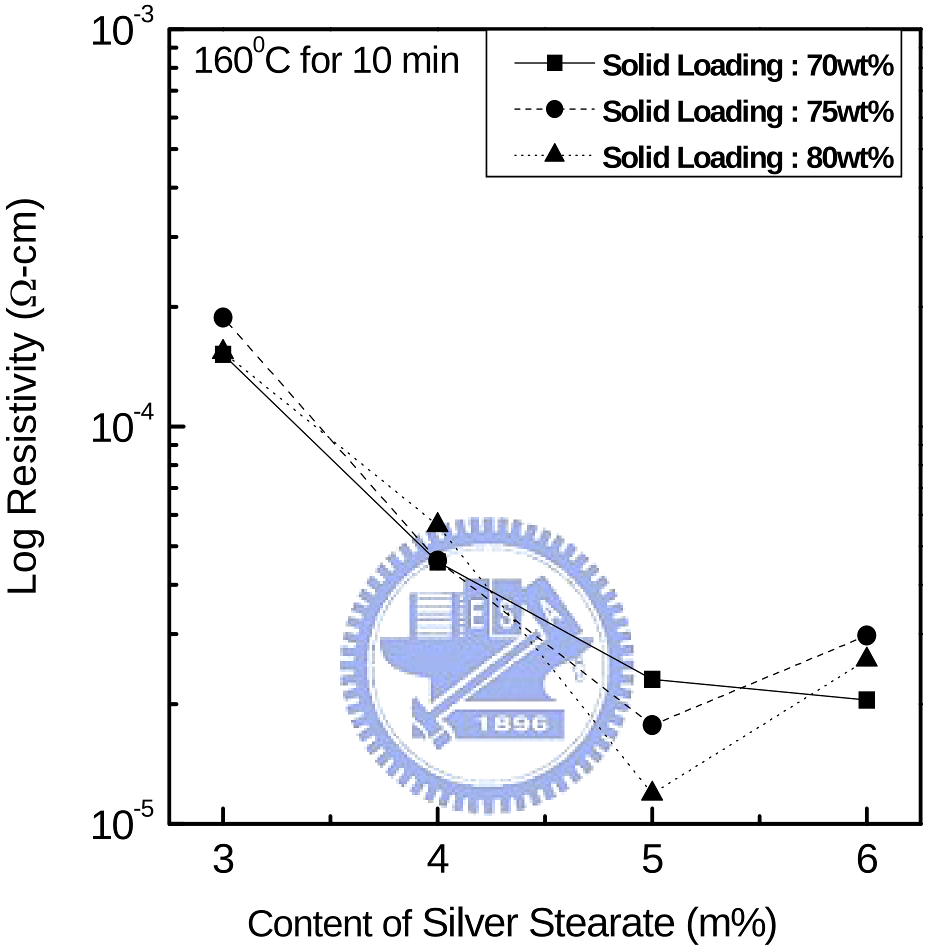

Figure 4-5(b). The electrical resistivities of silver films prepared from the pastes with various Ag_2O/silver stearate ratios and solid loadings, after being cured at 160°C for (a) 5 min and (b) 10min.

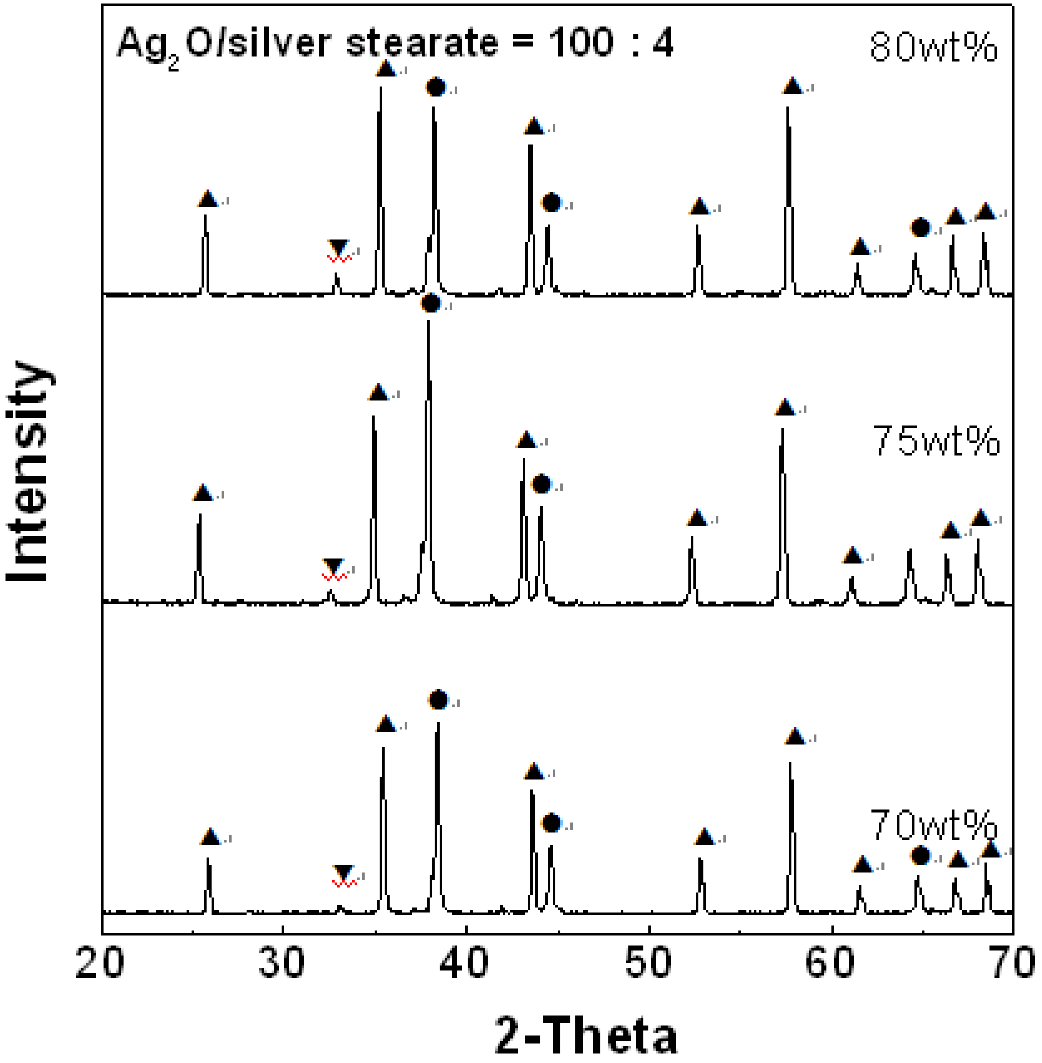

Figure 4-6. XRD results of the film with the Ag_2O/silver stearate ratio of 100:4, after being cured at 160°C for 10 min.

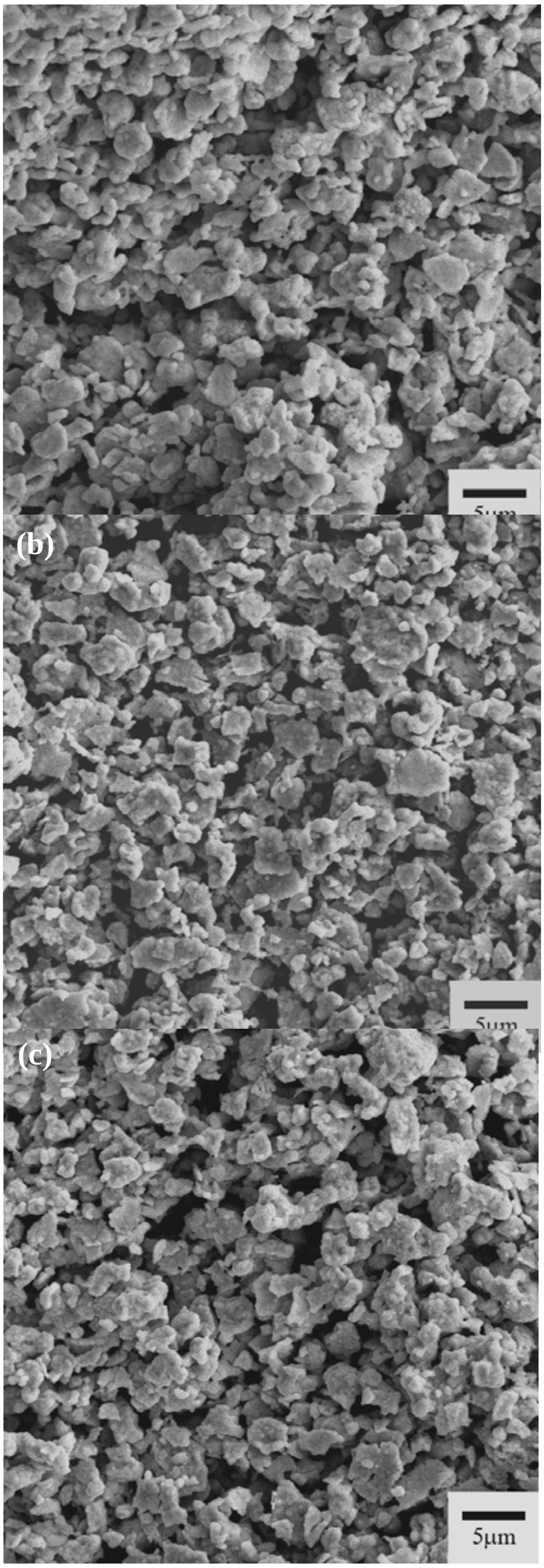

Figure 4-7. SEM micrographs of the films, prepared from the pastes with the Ag_2O/silver stearate ratio of (a) 100:4, (b) 100:5, and (c) 100:6, at a solid loading of 80wt% and after being cured at 160°C for 10 min.

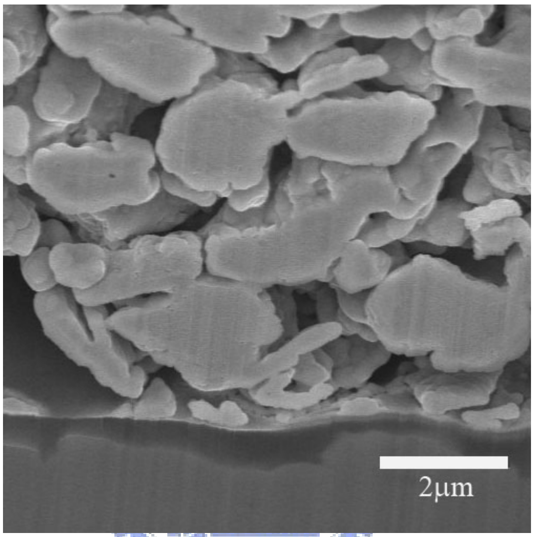

Figure 4-8. SEM cross-section micrographs of the film, prepared from the paste with the Ag_2O/silver stearate ratio of 100:5 at a solid loading of 80wt% and after being cured at 160°C for 10 min.

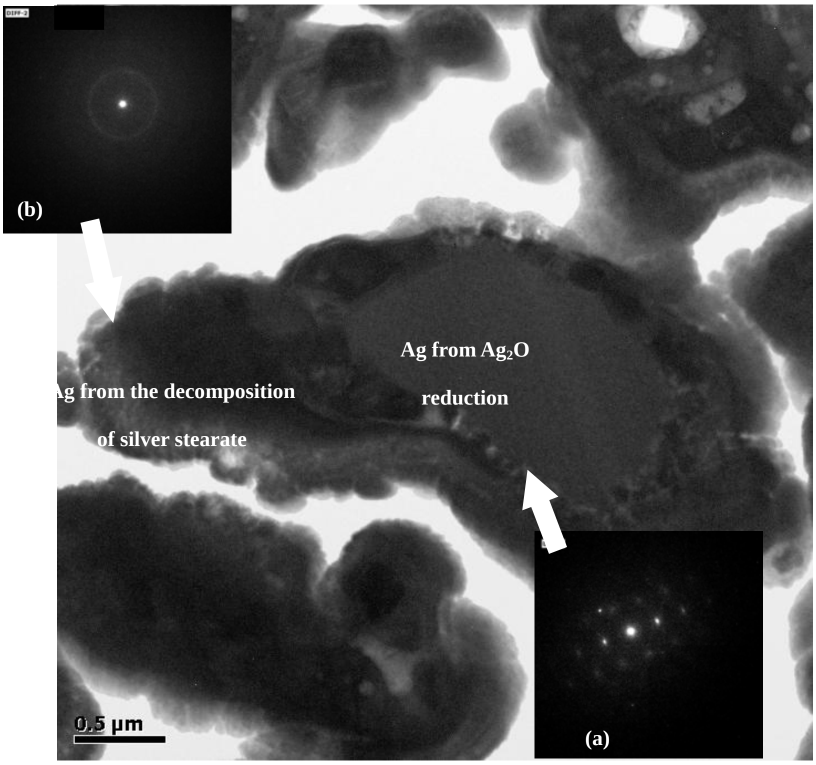

Figure 4-9. TEM microstructure of film prepared from the pastes with the Ag_2O/silver stearate ratio of 100:3, at a solid loading of 80wt% and after being cured at 160°C for 10 min.

Table 4-1. Formulations of low-curing-temperature silver pastes prepared in this study.

Solid Loading	Weight Ratio of Ag_2O to Silver Stearate	Paste Composition			Total Ag Content in Paste
		Ag_2O	Silver Stearate	α-Terpineol	
70wt%	100:3	67.96 wt%	2.04 wt%	30 wt%	63.83 wt%
	100:4	67.31 wt%	2.69 wt%	30 wt%	63.41 wt%
	100:5	66.67 wt%	3.33 wt%	30 wt%	62.99 wt%
	100:6	66.04 wt%	3.96 wt%	30 wt%	62.57 wt%
75wt%	100:3	72.82 wt%	2.18 wt%	25 wt%	68.40 wt%
	100:4	72.12 wt%	2.88 wt%	25 wt%	67.94 wt%
	100:5	71.43 wt%	3.57 wt%	25 wt%	67.48 wt%
	100:6	70.75 wt%	4.25 wt%	25 wt%	67.04 wt%
80wt%	100:3	77.67 wt%	2.33 wt%	20 wt%	72.95 wt%
	100:4	76.92 wt%	3.08 wt%	20 wt%	72.46 wt%
	100:5	76.19 wt%	3.81 wt%	20 wt%	71.98 wt%
	100:6	75.47 wt%	4.53 wt%	20 wt%	71.51 wt%

Chapter 5

Thermal Behavior and Transformation Kinetics of Titanium Dioxide Nanocrystallites Prepared by Coupling Agents.

Coupling agents have been widely used to retard the sintering of silver paste and minimize co-firing defects due to densification mismatch between silver and dielectrics. The thermal-decomposition and crystallization behaviour of the coupling agent is a subject of great concern. Differential thermal analysis (DTA), X-ray diffraction (XRD), transmission electron microscopy (TEM), and electron diffraction (ED) were utilized to study the phase transformation behavior of the coupling agents. To elucidate what is responsible for the oxidation, Ti organometallic compounds were calcined at different temperatures (350, 400, 500, 600℃) for 2 h and the crystallization behavior was determined by X-ray diffraction (XRD). This demonstrates the presence of an anatase phase until a temperature of greater than 350℃, and the intensity of the crystalline peak of (101) at $2\theta = 25.3^0$ *increases continuously with the dwell time.*

The activation energy for crystallization of coupling agents was studied by using isothermal methods. Isothermal kinetics for the coupling agent system were investigated using quantitative X-ray diffraction (XRD) analysis. According to the quantitative XRD method, the value computed by the Johnson-Mehi-Avrami equation is 134.9 kJ/mol. The growth morphology parameters are 1.061, 0.915, 1.016 respectively.

Combining the results of DTA, XRD and TEM, it is found that formation of nanocrystallized titania accompanies the combustion of organometallic compounds.

5.1 Introduction

With the reduction in size of mobile communication equipment the market for chip module type high-frequency components is developing. These chip components are required to have high performance and must be of relatively low cost. So far Ag/Pd or Ag/Pt electrode pastes have mainly been used in these components, but now low-temperature firing ceramics, which are fired at 850–950℃, are being developed. These low-firing ceramics open up the possibility of firing only Ag without Pd or Pt. However, high electrical conductivity is preferable for high-frequency, low-loss, hybrid circuit applications since the skin effect is minimized. For multilayer ceramic devices, high conductivity of the internal metallization is important to reduce the dissipation factor, especially at high frequencies[1, 2]. Ag powder has a problem of shrinkage mismatch with the dielectric during co-firing because the metal film starts to sinter at lower temperatures and it rapidly becomes very dense. This shrinkage mismatch can potentially create tensile stress in the region which sinters faster and shrinks more. Therefore stress can develop in the early stages of sintering. As stress in the film exceeds a critical level, process flaws will be generated[3, 4, 5]. Particulate additives such as dielectric materials and other oxides (ThO_2, Gd_2O_3, NiO, etc.) are often incorporated in the metallization to minimize the shrinkage mismatch with the dielectric during cofiring by delaying the early sintering of the metallization to higher temperatures so as to more closely match that of the dielectric. However, the high refractory oxides dosage is deleterious to the electrical conductivity.

We investigate a new method for minimizing shrinkage mismatch by coating the Ag powder surface with Ti organometallic compounds[6]. It is found that the formation of nanocrystallized titania accompanies the combustion of the organometallic compounds and is found to inhibit the densification of silver at low temperature, thus retarding sintering of the silver at a higher temperature and minimizing co-firing defects due to densification mismatch between silver and dielectrics. In this paper the thermal behavior and transformation kinetics of TiO_2 of the coupling agent are the subject of great concern.

5-2 *Experiment Procedure*

5-2-1 Powder and coupling agent characterization

Commercially coupling agent (Kenrich petrochemicals, Inc.) was used as raw materials in this investigation. The organometallic Ti compound used was isopropyl tri(N-ethylenediamino) ethyl titanate. The structure of this compound is shown below：

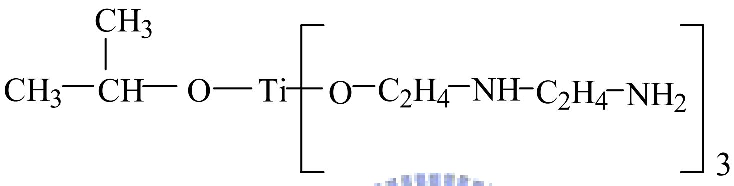

$$CH_3-\underset{}{\overset{CH_3}{\overset{|}{CH}}}-O-Ti\left[O-C_2H_4-NH-C_2H_4-NH_2\right]_3$$

Titanium-derived coupling agents are unique in that their reaction with the free protons at the inorganic interface results in the formation of organic monomolecular layers on the inorganic surface.

Thermal analysis was conducted to examine the heat and weight changes for coupling agent during the calcination process. Thermal analysis was carried out using differential thermal analysis (Perkin Elmer, DTA7) and thermogravimetric analysis (Perkin Elmer, TGA7) to investigate the possible phase transformation between 25 and 500℃ at a heating rate of 10℃min^{-1} in different atmosphere (Air, N_2, O_2) .

5-2-2 Thermal analysis

Thermal analysis was conducted to examine the heat and weight changes for coupling agent during the calcination process. Thermal analysis was carried out using differential thermal analysis (Perkin Elmer, DTA7) and thermogravimetric analysis (Perkin Elmer, TGA7) to investigate the possible phase transformation between 25 and 500℃ at a heating rate of 10℃min^{-1} in different atmosphere (Air, N_2, O_2) .

5-2-3 Characterization of calcined coupling agent

The coupling agent was dried and calcined at temperatures ranging from 350 to 600℃ for 2 h. X-ray diffraction (XRD) was conducted on the calcined coupling agent using an XRD System (model Philips PW1700) with monochromatic Cu Kα radiation. The accelerating voltage and current were set at 40kV and 40mA, respectively. A scan speed of 40 min^{-1} was selected from 2θ angles of 20^0 to 70^0.

The volume fraction (α) of anatase was calculated from the integrated XRD peak intensities of the crystalline peak of (101) at 2θ=25.3^0. The integral intensity data were collected from 2θ angles of 22^0 to 28^0 of with a scan rate of 0.25^0(2θ) min^{-1}.

5-3 Results and Discussion

5-3-1 Thermal decomposition of coupling agents

The DTA results (**Figure 5-1**) show that an exothermic peak is detected in all the coated Ag powder samples ； this peak is absent in the uncoated silver powder. To identify what is responsible for the exothermic peak, TGA was used to characterize the pure coupling agents (Zr, Al, Ti), as shown in **Figure 5-2**. All the coupling agents show significant maximum weight loss in the temperature range 200 to 300℃；however the weight loss percentages of these samples are different. Combining the DTA and TGA results, it is clear that the organic coupling agent is on the silver powder surfaces and the coupling agent layer is decomposed/vaporized from 200 to 300℃. Another approach for the analysis of the thermal decomposition is to identify it in different atmospheres. **Figure 5-3** shows that the exothermic peaks shift to a lower temperature (Zr: from 250 to 236℃, Al from 261℃ to 243℃, Ti: from 288℃ to 263℃) when the samples are analyzed in an O_2 atmosphere. This suggests that the exothermic peak is related to an oxidation process of the coupling agent. The exothermic peak is absent when the sample is analyzed in N_2 atmosphere as shown in **Figure 5-4**.

5-3-2 Crystallization kinetics of coupling agents

To elucidate what is responsible for the oxidation process, the Ti-based coupling agent was calcined directly at four different isothermal temperatures (350, 400, 500, 600℃) for 2h and the crystallization behavior was determined by XRD. **Figure 5-5** shows that the anatase phase is detected until the temperature is higher than 350℃. Since the anatase phase is detected up to temperatures lower than 350℃ and the amount of anatase phase precipitated cannot be directly determined by XRD analysis. Therefore, the volume fraction (α) of crystalline anatase phase is estimated from the integrated XRD intensity of the crystalline peak at $2\theta=25.3^0$. When the Ti organometallic compound is calcined at 400℃, for a time longer than 12h, the XRD pattern of the anatase phase is reasonably sharp and no anomalous intensity changes for the major peak (101). We therefore consider the intensity of this peak to be the standard for comparing the relative crystallinity. The relative amount of anatase present in the calcined Ti organometallic compounds is determined by comparing the intensity of the major peak of the anatase with the standard specimens. In **Figure 5-6**, the fraction of TiO_2 formed , α, is plotted as a function of reaction time for isothermal reaction at 350, 375, and 400℃. The kinetic data for the isothermal reaction follows a parabolic-like behavior. At 350℃, the fraction of the new phase of TiO_2 is almost 27% after reaction for 60 min. When the reaction time is extended to 120min, 50% of TiO_2 is obtained. When the temperature is raised to 375℃, and 400℃, 50% of TiO_2 was obtained within 15 min and 23 min, respectively. **Figure 5-7** shows the temperature dependence of the time at which volume fraction of anatase crystal is 50% in an isothermal crystallization of titanate precursor powders .Combining the results of DTA and XRD, it is found that formation of nano-crystallized titania accompanies the combustion of organometallic compounds.

To obtain the kinetic parameter of Ti precursor powders, the following rate equation is assumed[7]

$$\frac{d\alpha}{dt}=k^n t^{n-1}(1-\alpha) \tag{5.1}$$

Here α is the crystallization fraction at time t, n is the growth morphology parameter, and k is related to temperature T by an Arrhenius –type equation

$$k = A\exp\left(-\frac{E_a}{RT}\right) \tag{5.2}$$

Where Ea is the activation energy, R is the gas constant and A is a constant. The intergrated form of Eq. (5.1) can be expressed by the well-known Johnson-Mehl-Avrami (JMA) equation[8, 9]

$$\ln\left(\frac{1}{1-\alpha}\right) = (kt)^n \tag{5.3}$$

Equation (5.4) is obtained by taking the logarithms of both sides of Eq. (5.3)

$$\ln\ln\left(\frac{1}{1-\alpha}\right) = n\ln k + n\ln t \tag{5.4}$$

When the left side of Eq. (5.4) $\{\ln\ln[1/(1-\alpha)]\}$ is plotted against lnt as shown in Figure 8, the straight line slope, n, indicates the growth morphology parameter of crystallized phase. The growth morphology parameter n in the crystallization process for Ti precursor powders at varying calcined temperatures is shown in Figure 8. By Eq.(5.4) and **Figure 5-8**, the growth morphology parameter n is obtained being 1.061, 0.915, 1.016, respectively. **Figure 5-8** also provides the kinetic constant data k by the interception of the straight line with the axis of $\{\ln\ln[1/(1-\alpha)]\}$.

Equation (5.5) is obtained by taking the logarithms for both sides of Eq. (5.2).

$$\ln k = \ln A - \frac{E_a}{RT} \tag{5.5}$$

When the left side of ln k in Eq. (5.5) is plotted against the reciprocal of temperature, as shown in **Figure 5-9**. a straight line is obtained, and then the apparent activation energy can be calculated from the slopes and the activation energy for crystallization of coupling agents is 134.9 kJ mol^{-1}.

The TEM bright field (BF) images and electron diffraction (ED) patterns of the Ti-base coupling agent calcined at 375℃ for 60min are shown in **Figures 5-10 and 5-11**. It is found that very fine powders have a primary size of about 10nm. **Figure 5-10(b)** demonstrates the high resolution TEM image of anatase crystal, the (101) spacing of anatase is about 3.61 $\overset{o}{A}$. **Figure 5-11** shows the ED pattern of coupling agent calcined at 375℃ for 60min. This result agrees with the crystallites type measured from XRD.

5-4 Summary

Nanocrystalline titania powders have been synthesized by calcining Ti-base coupling agent directly. The thermal behavior and transformation kinetics of TiO_2 nanocrystallites prepared by coupling agents are studied by using isothermal methods. The kinetic data for isothermal reaction follow a parabolic-like behaviour. It is found that the formation of nanocrystallized titania accompanies the combustion of organometallic compounds. The results are summarized as follows:

(1) The isothermal activation energy for for the anatase TiO_2 crystallization is 134.9 kJ mol^{-1}.

(2) Both TEM examination and SAED analysis indicate that the anatase TiO_2 nanocrystallites with a spherical-like morphology ranging from 10 to 20 nm are formed by calcining Ti-base coupling agent directly.

References:

1. J. M. Herbert, Ceramic Dielectrics and Capacitors. Electrocomponet Science Monographs,.(Gordon and Breach , New York, 1985) Vol. 6, p.91.
2. W. Noorlander, Electrocomponet Sci. Technol. 5(1978) 33.
3. A. H. Kumar and R. R. Tummala, Int. J. Hybrid Microelectron. 14, (1991) 137.
4. R. K. Bordia and R. Raj, J. Am Ceram. Soc. 68(1985) No.6, 287.
5. C. H. Hsueh and A. G. Evans, J. Am. Ceram. Soc. 68 (1985) No 3, 120.
6. C. J. Shih, S. J. Shih, H. C. Lin, Y. C. Hung, H. H. Yeh, Nanotechnology, 14, (2003)1014.
7. A. Marotta, A. Buri, and G. L. Valenti, J. Mater. Sci. 13(1978) 2483.
8. M. Avami, J. Chem. Phys. 7(1939) 1103.

S. B. Wen, N. C. Wu, S. Yand, and M. C. Wang, J. Mater. Res. 14(1999) 3559.

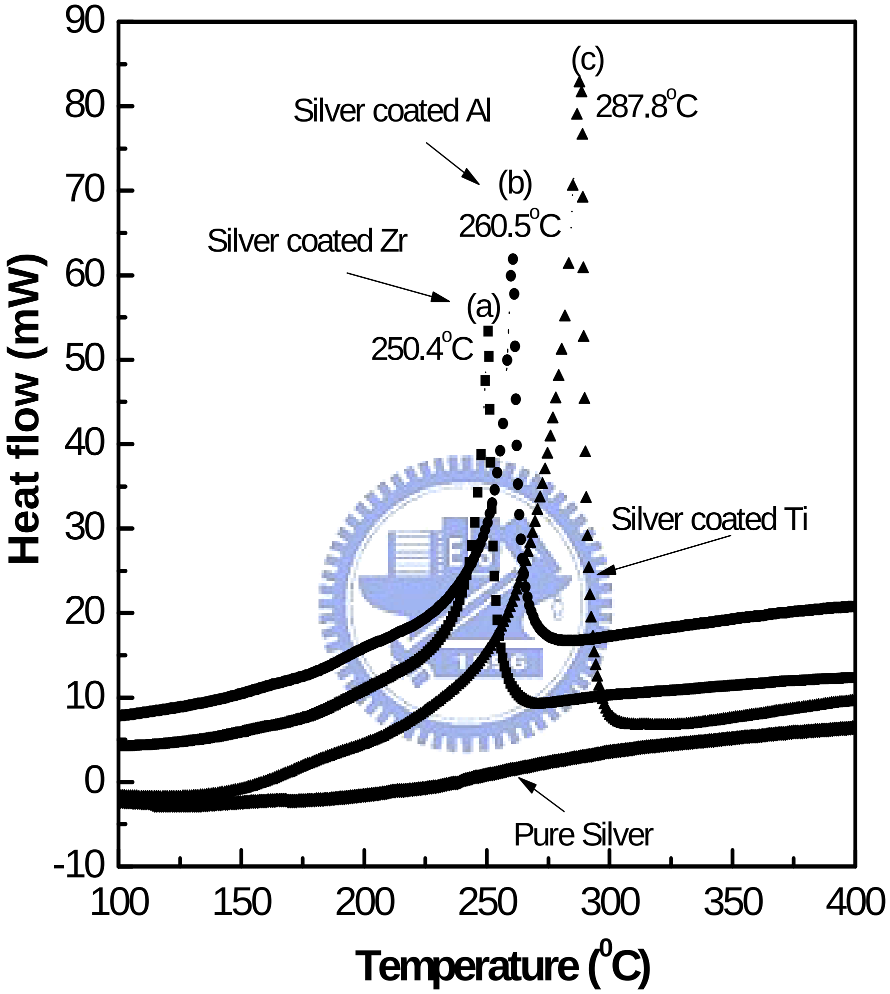

Figure5-1. DTA analyses for pure Ag and Ag powders coated with coupling agents of (a) Zr (b) Al (c) Ti at a heating rate of 10℃ in air.

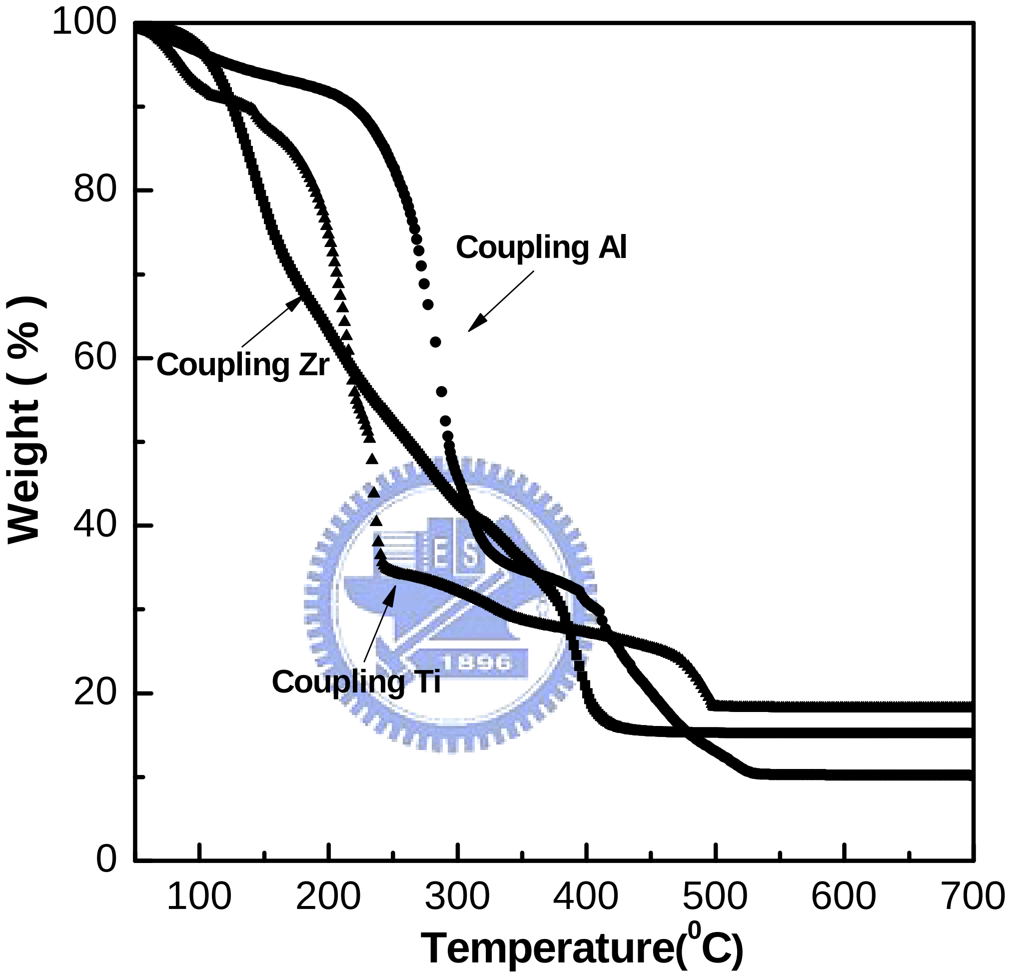

Figure 5-2. Weight loss of pure coupling agents of (a) Zr (b) Al (c) Ti at a heating rate of 10℃ in air.

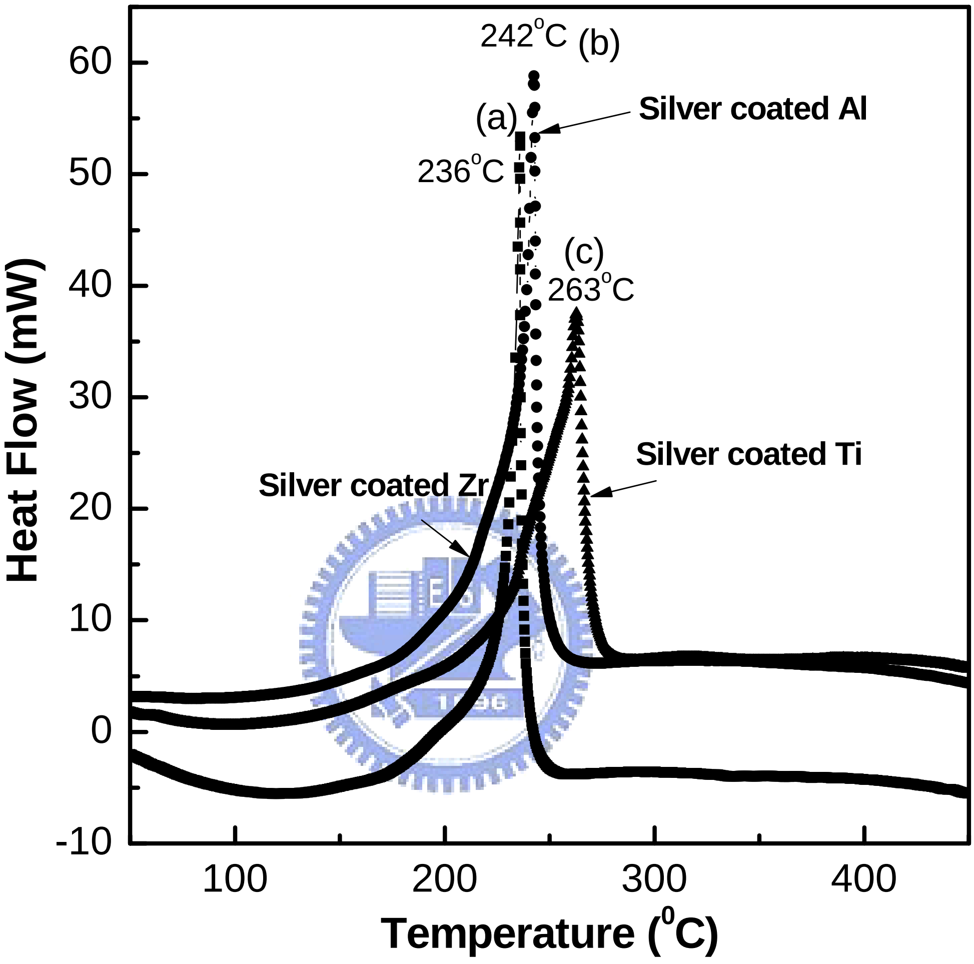

Figure 5-3. DTA analyses for Ag powder coated with (a) Zr, (b) Al (c) Ti coupling agents at a heating rate of 10℃ in O_2

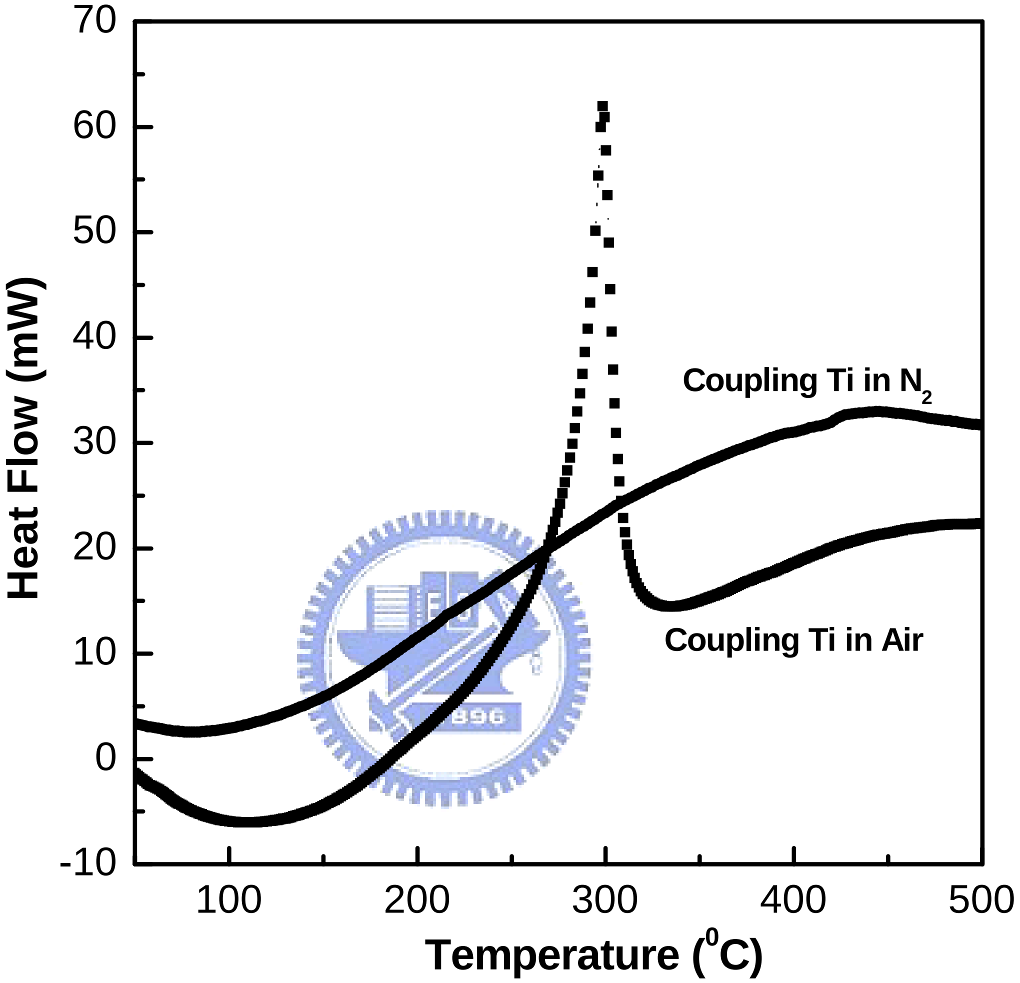

Figure 5-4. DTA analyses for Ag powder coated with Ti coupling agents at a heating rate of 20℃ in (a) Air and (b) N_2.

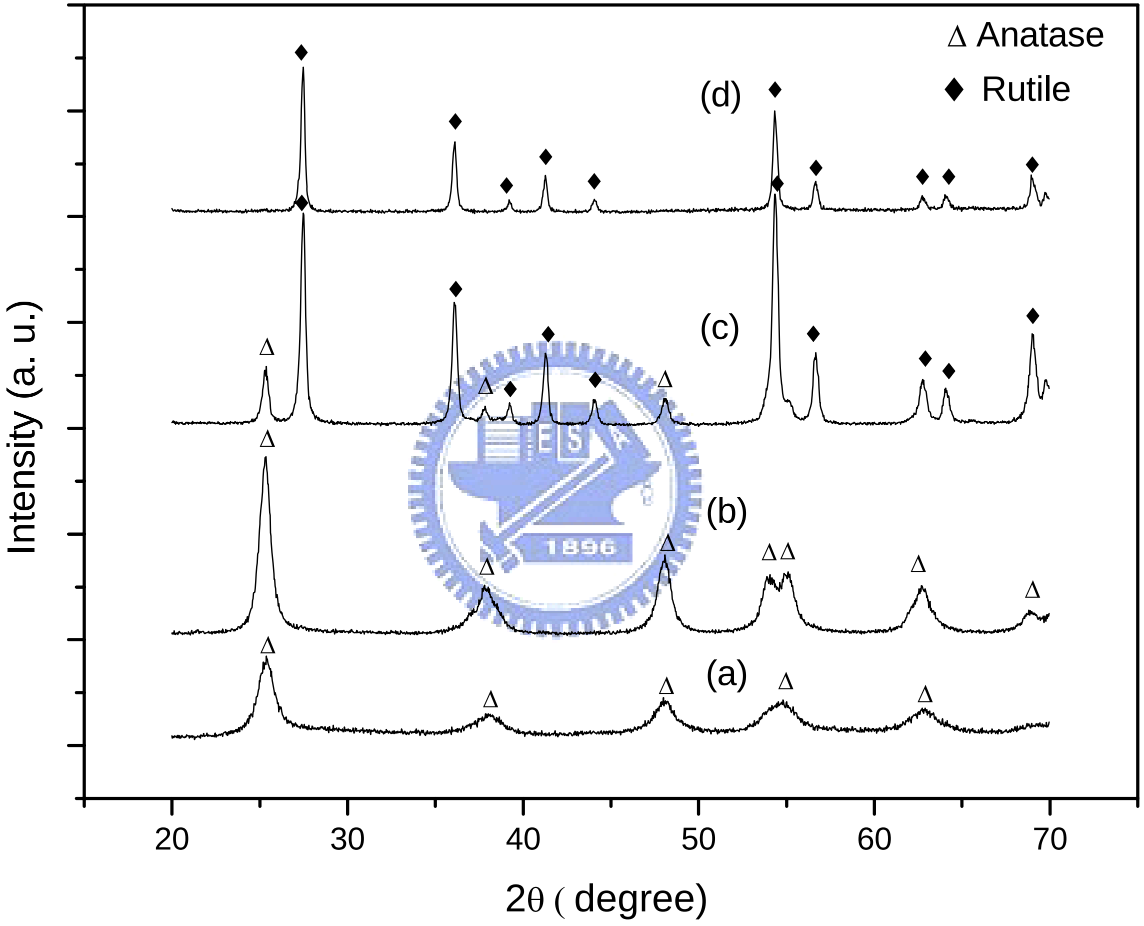

Figure5-5. XRD patterns of organometallic compounds of Ti calcined at (a) 350℃ (b) 400℃ (c) 500℃ (d) 600℃ for 2 h.

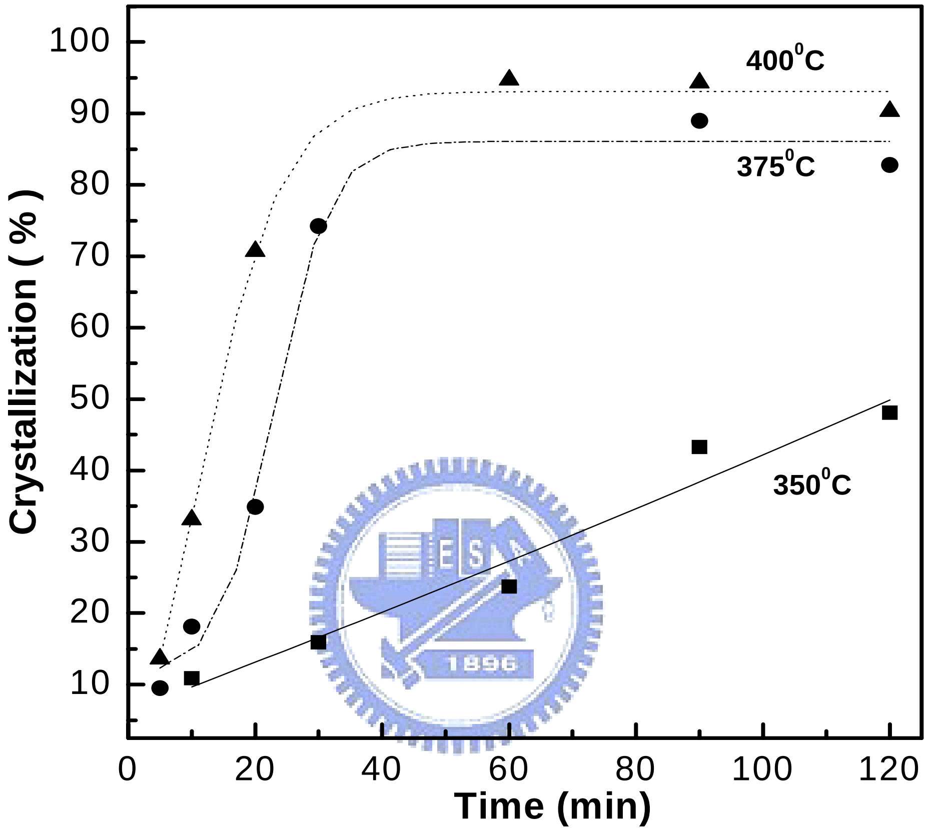

Figure 5- 6. Variation of volume fraction of Anatase crystal wth time. In isothermal crystallization of isopropyl tri(N-ethylenediamino) ethyl titanate precursor powders.

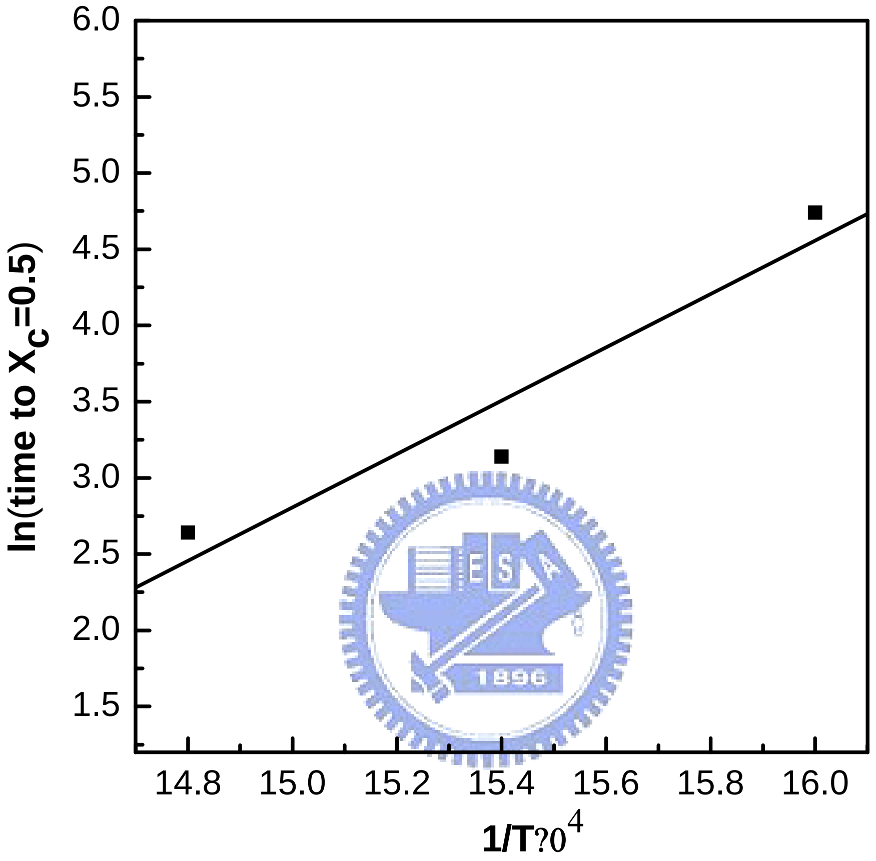

Figure 5-7. Temperature dependence of the time at which volume fraction of anatase crystal is 50% in an isothermal crystallization of titanate precursor powders.

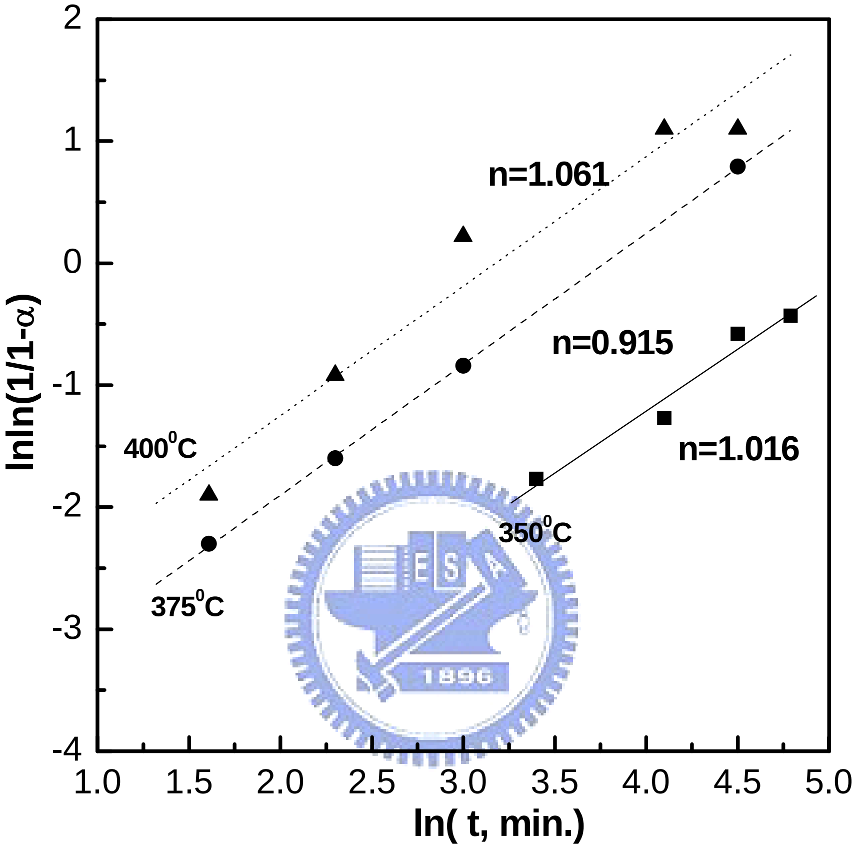

Figure 5-8. Determination of the growth morphology parameter (n) in the crystallization process for titanate precursor powders

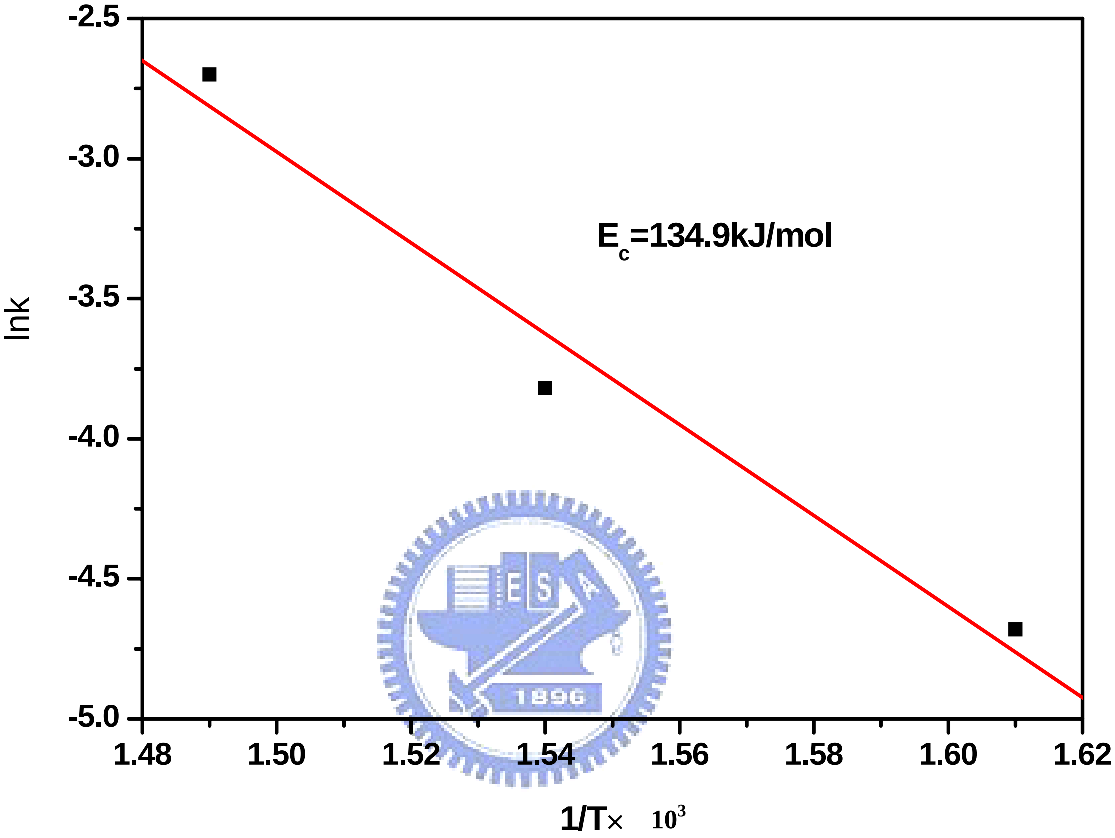

Figure 5-9. Activation energy for crystallization of Ti-base coupling agents

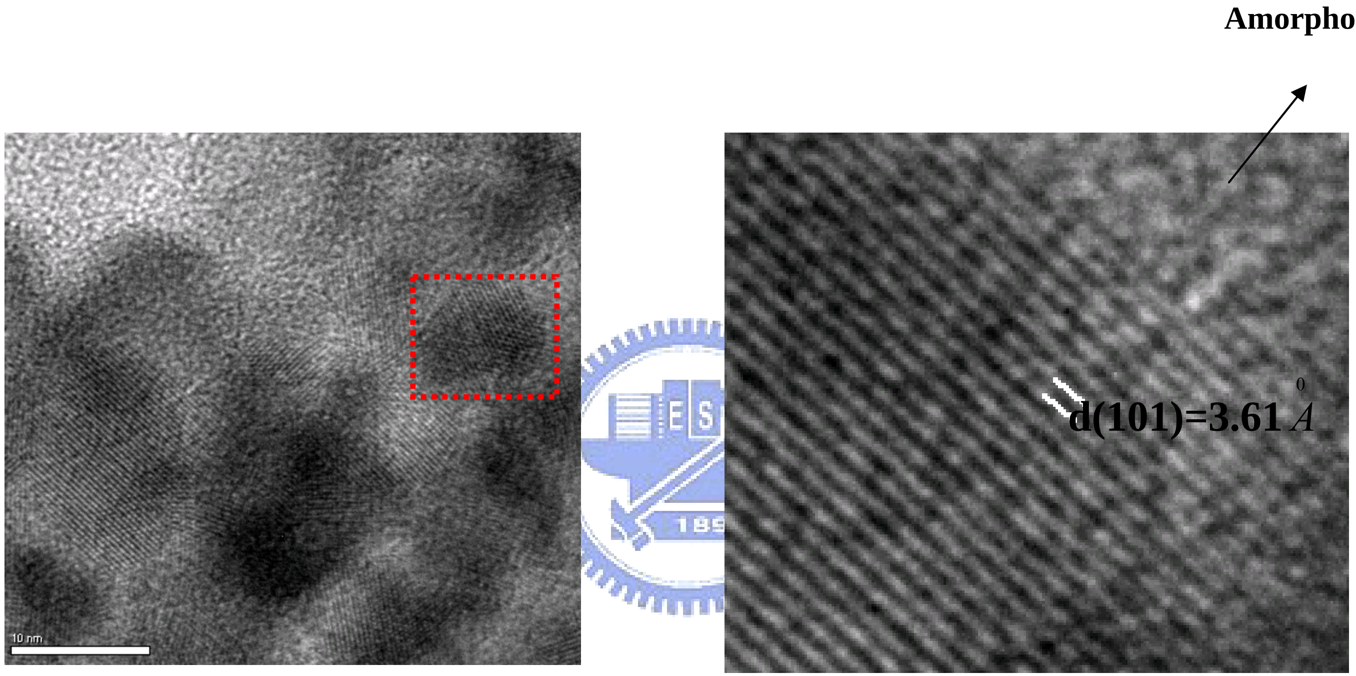

Figure 5-10. TEM images of the of the Ti-base coupling agent calcined at 375℃ for 60min (a) primary size of about 10nm (b) lattice image showing the lattice spacing of (1 0 1) is 3.61 Å.

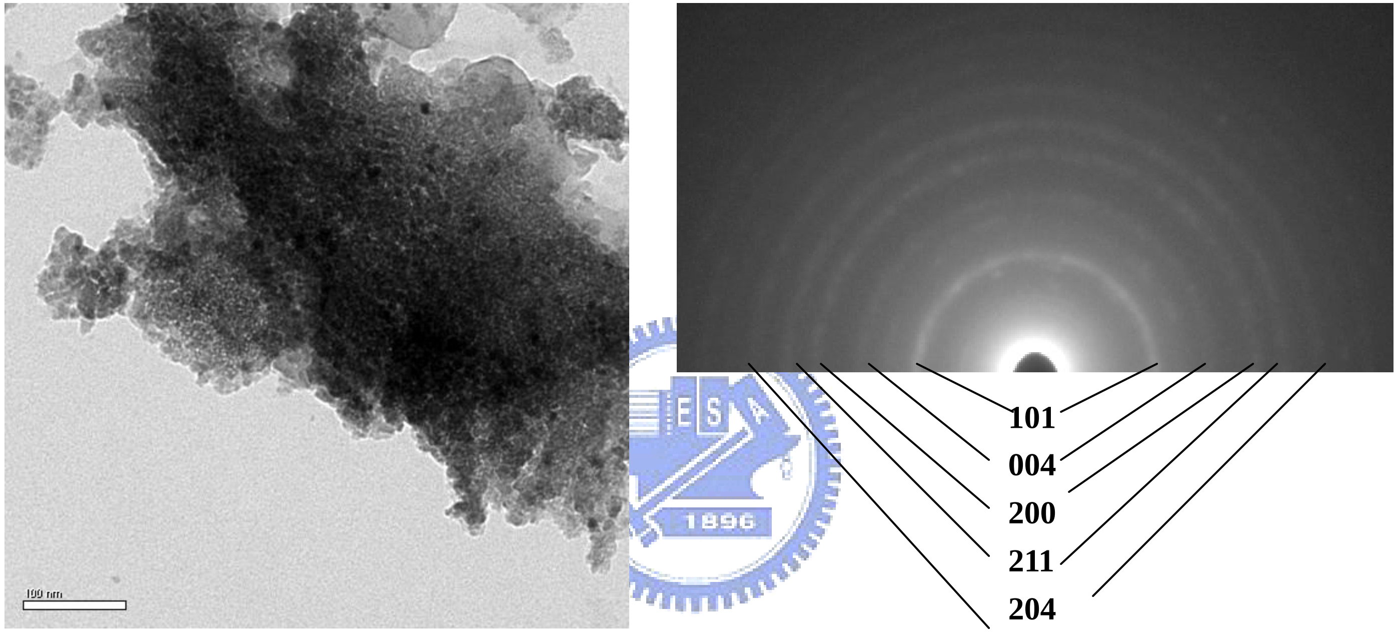

Figure 5-11. TEM BF images and ED pattern of the Ti-base coupling agent calcined at 375℃ for 60min (a) BF images (b) ED pattern .

Chapter 6

High-Frequency Electrical Properties of Silver Thick Films Measured by Dielectric Resonator Method

The electrical properties of silver films, prepared using a low-curing-temperature metallo-organic-decomposition (MOD) paste and a high-temperature silver paste screen-printed on polished and nonpolished alumina substrates, at microwave frequency were characterized in this study. Surface resistance and effective conductivity of the silver films at microwave frequency (approximately 4 GHz) were evaluated using the TE_{011} *mode of the resonator cavities method. Devices of T-type resonator circuits were fabricated to determine the simulated and measured Q-values and to evaluate the effects of silver films and the surrounding substrate. The surface roughness of the fired films printed on nonpolished* Al_2O_3 *substrate is slightly less than those on polished substrate, because the surface energy of the nonpolished alumina (29.81 mN/m) is slightly less than that of the polished alumina (36.69 mN/m). The calculated effective conductivities at 4.3 GHz are slightly less than the DC conductivities of the films. Moreover, the films prepared using the high temperature silver paste have higher electrical conductivity ranging from* 4.08×10^7 *to* 4.13×10^7 *S/m, since the high-temperature firing process leads to an improved connectivity of the silver particles. The results indicate that the films screen-printed on the polished substrate have a higher Q and a lower* ΔQ *value than those of films that are screen-printed on the nonpolished substrate. For the silver films prepared using the high-temperature silver paste, both the Q and* ΔQ *values were the highest among the films studied, which is consistent with the* *observation of the dense microstructure of the silver film and the interfacial reaction between the glass in the film and the substrate as a result of high firing temperature.*

6-1. *Introduction*

Traditionally, commercial conductive inks designed for various printing processes have two types of formulation, one method is to use a conducting metal particle as the conducting phase and use resins as the binders and vehicles, and the other is to use a metal particle as the conducting phase while glass acts as the binding and adhesive agent. However, the glass, binder, and vehicles are generally nonconductive, which may hinder the contacts of metal powders and reduce the electron transmission.

For flexible applications, low-curing-temperature conductor technology with metallo-organic-decomposition (MOD) compound additions was investigated to form a three-dimensional metal network. There is no binder and glass addition in the MOD compounds. The MOD compounds are generally synthetic metallo-organic salts that decompose completely at low temperature to precipitate metal or oxide, depending on the metal and firing atmosphere.[1, 2] A previous study[1] indicated that a paste containing 2-ethylhexanoate ($C_8H_{15}O_2Ag$) has a very low decomposition temperature (190.3°C) among MOD agents, and it forms silver particles to promote the linking among silver flake particles and thus reduces the resistivity to <13 Ω-cm at temperatures as low as 200°C. However, the electrical resistivity of the metal film was affected by the connectivity of metal particles in addition to the surface roughness and porosity of the film, which resulted from the evaporation of organic matter at high temperature.

Recently, there has been tremendous interest in the development of thick-film conductors for use in high-frequency applications, such as radio-frequency identification (RFID) tags. The behavior of an electromagnetic wave traveling through the metal film is dependent on the characteristics of the metal film and the surrounding substrate. Therefore, it is important to understand the electrical properties of metal films at high frequencies. To date, very little information regarding the electrical properties of silver thick-films at microwave frequency is found in the literature. In this study, a low-curing-temperature silver paste containing silver 2-ethylhexanoate[1] and a conventional high-temperature silver paste containing a glass binder were screen-printed on Al_2O_3 substrates with polished and nonpolished surfaces and then fired at an optimum temperature. The surface resistance and effective conductivity of the silver films at microwave frequency (approximately 4 GHz) were evaluated using the TE_{011} mode of the resonator cavities method. The surface and cross-section microstructures of the films were characterized by scanning electron microscopy (SEM). The effects of the silver film microstructure and substrate characteristics on the electrical resistivity of the silver films are discussed.

6-2. *Theoretical Consideration of Surface Resisitivity Measurement*

Metal films are widely used in many applications, such as copper cladded laminates, metallized low-temperature cofiring ceramic (LTCC) substrates, conductivity circuits, electric electrodes, and metallized antenna patterns. In the radio-frequency (RF) applications, the metal film conductivity is a critical factor for RF loss and impedance match. For metal films, the surface resistance (R_s)

and effective conductivity at microwave frequency can also be measured using the resonator cavities method with a sapphire dielectric resonator operating on its TE_{011} mode, which is the most accurate measurement that can be performed. This method, which was originally used to determine the surface resistance of high-temperature superconductors,[3, 4] could also be used to measure the surface resistance of bulk conductors[5]. From the theoretical treatment of the TE_{011} resonant mode, the surface resistance and RF current density of the film can be calculated from the unloaded Q-value and the dissipated power. The advantage of using TE_{011} mode cavities for surface resistance measurements is that there are simple and exact formulas for the resonant frequency of such cavities as well as for the quality factor, and the unique surface current distribution allows one to avoid contact problems between bottom and lateral surfaces in such cavities. As presented by Krupka[5], the total unloaded Q-factor of the resonant structure in the dielectric resonator measurements can be expressed as

$$Q^{-1} = Q_c^{-1} + Q_p^{-1} = \frac{R_{surface}}{G_b} + Q_p^{-1}, \tag{6.1}$$

where Q_c is the Q-factor associated with conductor losses in the measured metal layer, Q_p is the Q-factor due to parasitic losses from all other parts of the resonant structure, G_b is a geometric factor for bottoms of the resonant structure, and $R_{surface}$ is the surface resistance of the measured metal layer. If the Q-factor due to parasitic losses (Q_p) and the measured unloaded Q-factor value are known, the surface resistance of metal layers can be calculated using the formula as

$$R_{surface} = G_b\,(Q^{-1} - Q_p^{-1}). \tag{6.2}$$

In traditional bulk metals for RF applications, the electric field decays exponentially over a skin depth of $\delta = (2/\omega\sigma\mu_0)$[1, 2, 6]. If the thickness of the metal film is several times larger than the skin depth, the effective conductivity can be determined using the formula as

$$\sigma = \frac{\pi f \mu_0}{R_{surface}^2}, \tag{6.3}$$

here, $\mu_0 = 4\pi \times 10^{-7}$ (H/m) and f is the measurement frequency.

6-3. Experimental Procedure

6-3-1 Sample preparation

The low-curing-temperature silver paste used in this study was prepared using Ag flake (Ferro, U.S.A.), a metallo-organic compound of silver 2-ethylhexanoate (STREM, U.S.A.), and a solvent of α-terpineol (TCI, Japan). All the materials were mixed using a high-speed mixer (Thinky Mixer) for 3 min and de-bubbled for 1 min. Subsequently, a uniform paste was formed using a triple-roller grinder (EXERT, Germany), which causes the breakdown of pigment agglomerates. The weight ratio of the silver flake powder to solvent was fixed at 25:75. Silver 2-ethylhexanoate was added at a level equal to 5 wt% of the total silver flake powder and solvent. Also, a commercial silver paste (Ag paste 6142D, DuPont, U.S.A.), which is a high-temperature silver paste for use in LTCC applications, was used for comparison in this study.

Large-area metal film samples were prepared for DC conductivity and high-frequency surface resistivity measurements. Two types of silver paste as described above were screen-printed on two types of alumina substrate, including polished and nonpolished substrates (Coors Ceramics Co., U.S.A.). The films prepared using the low-curing-temperature silver paste were fired at 250°C for 5, 10, 20, and 30 min. The films prepared using the high-temperature silver pastes were debindered at 350°C for 30 min and then fired at 800°C for 10 min.

6-3-2 Characterizations

The surface energies of polished and nonpolished alumina substrates were measured using a goiniometric system (A.S.C. products, VCA 2500XE, U.S.A.), which is composed of a microliter syringe for dosing the liquids and an optical system[7]. The contact angles of the liquids, including DI water, diiodomethane (Aldrich, U.S.A.) and formamide (ACROS, U.S.A.), on the substrates were measured. Liquids were dosed onto the substrate surface and the droplet was allowed to stabilize for a few seconds before the contact angle was measured. Five measurements were performed for each liquid to obtain the average value.

The long-term roughness of the silver films was measured using a contact-mode profile meter (Kosaka Lab., LTD, Surfcorder ET 4000A, Japan) for 8 mm line scanning. The short-term roughness of the silver films and bare alumina substrates was measured using a noncontact mode 3-D Optical Profilometer (Nano View NVE 10100, Korea) for 100 to 640 μm image area scanning. DC resistance measurements of the films were carried out with spiral silver metal lines with a length (l) of 216 cm, a line width (w) of 0.8 mm, and a line thickness (d) of 10~40 μm, which were screen-printed on a 12 x 12 cm^2 area of the alumina substrate. A Keithely 2400 multimeter with a four-point probe was used to measure the resistance of the silver films. The electrical conductivity based on the equation, $\sigma = L/(R \times w \times t)$, where R is line resistivity, w is the line width, t is the line thickness and L is the line length, was calculated.

High-frequency surface resistances were determined using the TE_{011}-mode dielectric resonator, which was designed by Krupka[5] and manufactured by QWED (QWED Inc., Poland), as indicated in **Figure 6-1**. To evaluate the Q-factor due to parasitic losses, the dielectric loss tangents of the substrate and dielectric resonator have to be known. The dielectric loss tangent of the substrate was measured by the split-post dielectric resonator method [8]. A BZT dielectric resonator of 17 mm diameter and of 8 mm height was used in this study. The measurement frequency ranged between 4 and 5 GHz. The electric energy filling factor and geometric factor were rigorously computed using the Rayleigh-Ritz method[9]. DC surface resistance measurements were performed on the large-area silver films with dimensions of 5 x 5cm^2. A Keithely 2400 multimeter with a four-point probe was used to measure the resistance of the fired silver films. The surface and cross-section microstructures of the silver films were investigated using a JEOL-6500F SEM.

To evaluate the effects of the silver films and substrates on the device performance, resonator patterns of high-frequency T-type circuits, which were designed to operate at 4.3~4.5 GHz, were fabricated and characterized. As shown in **Figure 6-2**, the widths of the transmission line on the polished substrate (thickness ≈ 0.51 mm) and nonpolished substrate (thickness ≈ 0.64 mm) were calculated to be 0.483 and 0.610 mm, respectively, in order to meet the nominal resonating frequency at 4.32 GHz. The resonating frequency of S_{21} for the devices was measured using a vector network analyzer (VNA; Anritsu 37397C, U.S.A.) with a TRL calibration fixture (Anritsu 3680V Universal Test Fixture, U.S.A.) and a K-type calibration kit. Q_{unload} was calculated using the formula, of $Q_{unload} = f_0/\Delta f$ (f_0 = center frequency; Δf = 3 dB insertion loss bandwidth).

6-4. Results and Discussion

Long-term (contact mode, 8 mm) and short-term (noncontact mode) surface-roughness values of the silver films, prepared using the MOD silver paste as well as the high-temperature silver paste screen-printed on polished and nonpolished alumina, are shown in **Table 6-1**. The short-term surface roughness values of polished and nonpolished bare alumina substrates were found to be 1.93 and 389.9 nm, respectively. The Al_2O_3 substrates used in this study were fabricated using tape casting technology. After sintering, pores or gain boundaries usually existed on the substrate surface, which determines the surface roughness. For the silver films studied, the short-term surface roughness values, shown in **Table 6-1**, are slightly larger than the long-term surface roughness values. This is due to the fact that the short-term measurement employs area scanning, which traces the local structure of the surface, while long-term measurement operates on a line scanning, which may not map out all the defects or bumpy areas. Comparison of both types of silver film shows that the surface roughness values of the fired films printed on the nonpolished Al_2O_3 substrate are slightly less than those on the polished substrate. The fluidity and wettability of the pastes on the substrate surface may correspond to the differences in the surface roughness of the films. The surface free energies of the polished and nonpolished Al_2O_3 substrates, measured using a goiniometric system, were found to be 36.69 and 29.81 mN/m, respectively. The surface energy of nonpolished alumina is slightly lower than that of polished alumina, because the former has a higher surface roughness. An increase in the surface roughness and number of pores generally causes a decrease in the wettability of hydrophilic oxide surfaces[10]. It is reported that macroscopic pores are generally filled with low-surface-energy contaminants or absorb water. Silver pastes screen-printed on the nonpolished Al_2O_3 with lower surface free energy leads to a better wetting property and fluidity, which allows an improved paste leveling on the substrate and results in a reduced surface roughness of the film.

For films prepared using the low-curing-temperature silver paste heat-treated at 250°C, the surface roughness slightly changes with soaking time. The surface roughness of the films slightly increases as the soaking time of the heat treatment is increased from 5 to 10 min, which is due to the shrinkage associated with the burnout of the organics. For the films prepared using the high-temperature silver paste, the high-temperature firing process causes the sintering of silver particles. Also, the softening of the glass binder at high temperature levels the silver film and enhances the adhesion with the Al_2O_3 substrate. Sintering and leveling reduces the thickness and surface roughness of the silver film.

Table 6-2 shows the results of DC resistivity of the silver films prepared using the MOD silver paste as well as the high-temperature silver paste screen-printed on polished and nonpolished alumina, measured using the four-point probe method. The films prepared using the low-curing-temperature MOD silver paste have electrical conductivities ranging from 8.1 x 10^6 to 10.5 x 10^6 S/m after the thermal treatment, which is relatively close to the bulk resistivity of Ag. Although the differences are insignificant, it appears that the electrical conductivity slightly increases with soaking time, owing to the organic burnout and coalescence of the silver particles. The films prepared using the high-temperature silver paste have higher electrical conductivity ranging from 4.08 x 10^7 to 4.13 x 10^7 S/m, because the high-temperature firing process leads to a better connectivity of the silver particles. Apparently, the slight difference in the surface-roughness of substrate has no effect on the DC conductivity of the screen-printed silver films.

Table 6-3 shows the results of the surface resistance and effective conductivity of the silver films prepared using the MOD silver paste as well as the high-temperature silver paste screen-printed on polished and nonpolished alumina, measured at the microwave frequency range. The surface resistance (R_s) was determined at a frequency of ≈ 4.3 GHz using the TE_{011} mode of the resonator cavities method. The skin depths of the electric field at microwave frequency for the silver films were calculated, as shown in **Table 6-3**. The results confirm that the thicknesses of the silver films, shown in **Table 6-2**, are at least 5 times larger than the skin depth values. The films prepared using the high-temperature silver pastes have surface resistance values smaller than those prepared using the low-curing-temperature MOD silver paste. Comparison of the films prepared using the low-curing-temperature MOD paste after heat treatment at 250°C for various times shows that the surface roughness increases slightly and the surface resistance slightly decreases with soaking time. This implies that the decrease in the surface resistance of the films is mainly due to the improved connectivity between the silver particles. The surface roughness of the substrate and the film's free surface has no effect on the high-frequency surface resistance of the screen-printed silver films. This may be due to the fact that the films are sufficient to eliminate the surface scattering (size effect) [11, 12], or the differences in the magnitude of the surface roughness are too small to cause a discrepancy in the high-frequency surface resistance. The effective conductivities of the films were determined using Eq. 6-3 and the results are shown in **Table 6-3**. The calculated effective conductivities at 4.3 GHz are slightly lower than the DC conductivity of the films. Moreover, similar to the DC conductivity, there is no significant difference in the high-frequency effective conductivity among the silver films prepared using the low-curing-temperature MOD silver paste.

Figure 6-3 shows the SEM surface images of the films prepared using the low-curing-temperature MOD silver paste screen-printed on polished as well as nonpolished substrates after heat treatment at 250°C for 10 and 30 min. Silver grains with neck growth and interconnected porosities are found in the microstructures, which confirm the low resistivities of the silver films. It seems that all the samples have very similar microstructures, although the silver grains are slightly bigger in size for the films being heat treated for 30 min, compared with those films heat treated for 10 min. It is apparent that the nature of the substrate has no effect on the microstructural evolution of the films. **Figure 6-4** shows the SEM images of the cross-sectional view of the films shown in **Figure 6-3**. It can be seen that the microstructures of the films are porous and the coalescent grains and porosities become larger as the soaking time increases.

The surface morphologies of the polished and nonpolished substrates do not change after firing because there is no chemical reaction or interdiffusion at the interface at the firing temperature of 250°C. **Figures 6-5** and **6-6** show the SEM images of the surfaces and the crosssections of the films, respectively, prepared using the high-temperature silver paste screen-printed on polished and nonpolished substrates. The sizes of the silver grains ranged between 5 to 10 μm. Both the films printed on the polished and nonpolished substrates have an irregular interface. In the high-temperature firing process, the glass added to the film not only densifies the silver film but also wets and reacts with the substrate. This results in a perfect adherence as well as an irregular interface between the films and substrate.

Devices of T-type resonator circuits were designed according to the effective conductivities of the silver films at frequencies of 4.24~4.30 GHz. The simulated and measured Q-values and resonance frequency values of T-type resonators prepared from the films using both low-curing-temperature MOD silver paste and high-temperature silver paste are shown in **Table 6-4**. The resonator circuit was designed to have a resonance frequency at 4.3~4.5 GHz. The measured Q-values of T patterns were used to calculate the ΔQ value [$\Delta Q = (Q_{HF}-Q_M)/Q_{HF}$; Q_{HF}: simulated value; Q_M: measured value]. ΔQ indicates the difference between the simulated and measured values of Q. The results indicate that films screen-printed on the polished substrate have a higher Q and a lower ΔQ value than those of the films screen-printed on the nonpolished substrate. It is known that the device loss at high frequency is mainly due to the conductor loss, dielectric loss, and radiation loss. In this study, the higher roughness of the substrate surface results in a higher ΔQ value (**Figure 6-4**), while the free-surface roughness of the silver film does not have a significant effect on the

ΔQ value. For the silver films prepared using the high-temperature silver paste, the Q values are higher than those of the films prepared using the low-curing-temperature MOD paste, because the former has a dense microstructure (**Figure 6-5**), which leads to a higher electrical conductivity and lower conductor loss. However, the difference between the simulated and measured Q values for the films printed on the polished substrate is similar to that printed on the nonpolished substrate, which is the largest among the films studied. This is due to the fact that the glass in the film reacts with the substrate during the high-temperature firing process, which results in a perfect adherence as well as an irregular interface between the film and substrate, as shown in **Figure 6-4**, and a higher dielectric loss.

6-5. Summary

The electrical properties of silver films, prepared using a low-curing-temperature MOD paste and a high-temperature silver paste screen-printed on polished and nonpolished alumina substrates, at microwave frequency were characterized in this study. On the basis of the results obtained, several conclusions could be made as follows:

a. The surface roughnesses of the fired films printed on nonpolished Al_2O_3 substrate are less than those printed on polished substrate owing to the lower surface energy of the former.
b. The calculated effective conductivities at 4.3 GHz are slightly less than the DC conductivities of the films.

c. The films prepared using the high-temperature silver paste have a higher effective conductivity ranging from 4.08 x 10^7 to 4.13 x 10^7 S/m, because the high-temperature firing leads to a better connectivity of the silver particles.

d. The results for the device with T-type resonator circuits indicate that the films screen-printed on the polished substrate have a higher Q and a lower ΔQ value than those of the films screen-printed on the nonpolished substrate.

For the silver films prepared using the high-temperature silver paste, the Q values are higher than those of the films prepared using the low-curing-temperature MOD paste, because the former has a dense microstructure that leads to a higher electrical conductivity and a lower conductor loss. However, the ΔQ values of the films prepared using the high-temperature silver paste are the largest among the films studied, owing to the interfacial reaction between the glass contained in the film and the substrate during the high-temperature firing process, which results in an irregular interface between the film and substrate and leads to a higher dielectric loss.

References:

1. C. A. Lu, P. Lin, H. C. Lin, and S. F. Wang: Jpn. J. Appl. Phys. **45** (2006) 6987.
2. C. A. Lu, P. Lin, H. C. Lin, and S. F. Wang: Jpn. J. Appl. Phys. **46** (2007) 251.
3. J. Krupka, M. Klinger, M. Kuhn, A. Baranyak, M. Stiller, and J. Hinken: IEEE Trans. Appl. Supercond. **3** (1993) 3043.
4. C. Wilker, Z. Y. Shen, V. X. Nguyen, and M. S. Brenner: IEEE Trans. Appl. Supercond. **3** (1993) 1457.
5. J. Krupka, IEEE MTT-S Int. Symp. Dig., 2007, p. 515.
6. K. Fuchs: Proc. Cambridge Philos. Soc. **34** (1938) 100.
7. R. J. Good: J. Adhes. Sci. Technol. **12** (1992) 1269.
8. J. Krupka, R. G. Geyer, J. B. Jarvis, and J. Ceremuga: DMMA' 96 Conf., Bath, U.K. 23-26 Sept. 1996, p. 21.
9. J. Barker-Jarvis, M. D. Janezic, B. Riddle, C. Holloway, N. G. Paulter, and J. E. Blendell: NIST Tech. Note 1520 (2001).
10. M. Harju, E. Levanen, and T. Mantyla: Appl. Surf. Sci. **252** (2006) 8514.
11. U. Jacob, J. Vancea, and H. Hoffmann: Phys. Rev. B **41** (1990) 11852.
12. E. Z. Luo, S. Heun, M. Kennedy, J. Wollschlager, and M. Henzler: Phys. Rev. B **49** (1994) 4858.

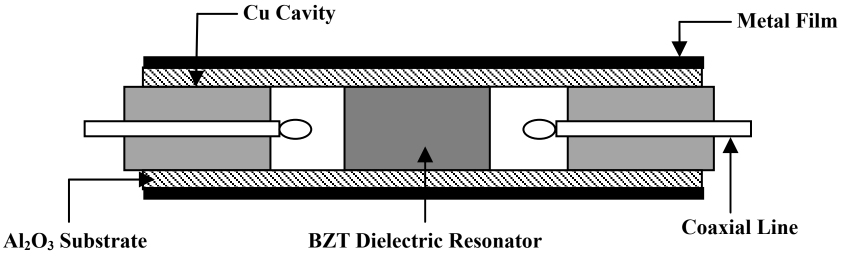

Figure 6-1. Schematic of dielectric resonator

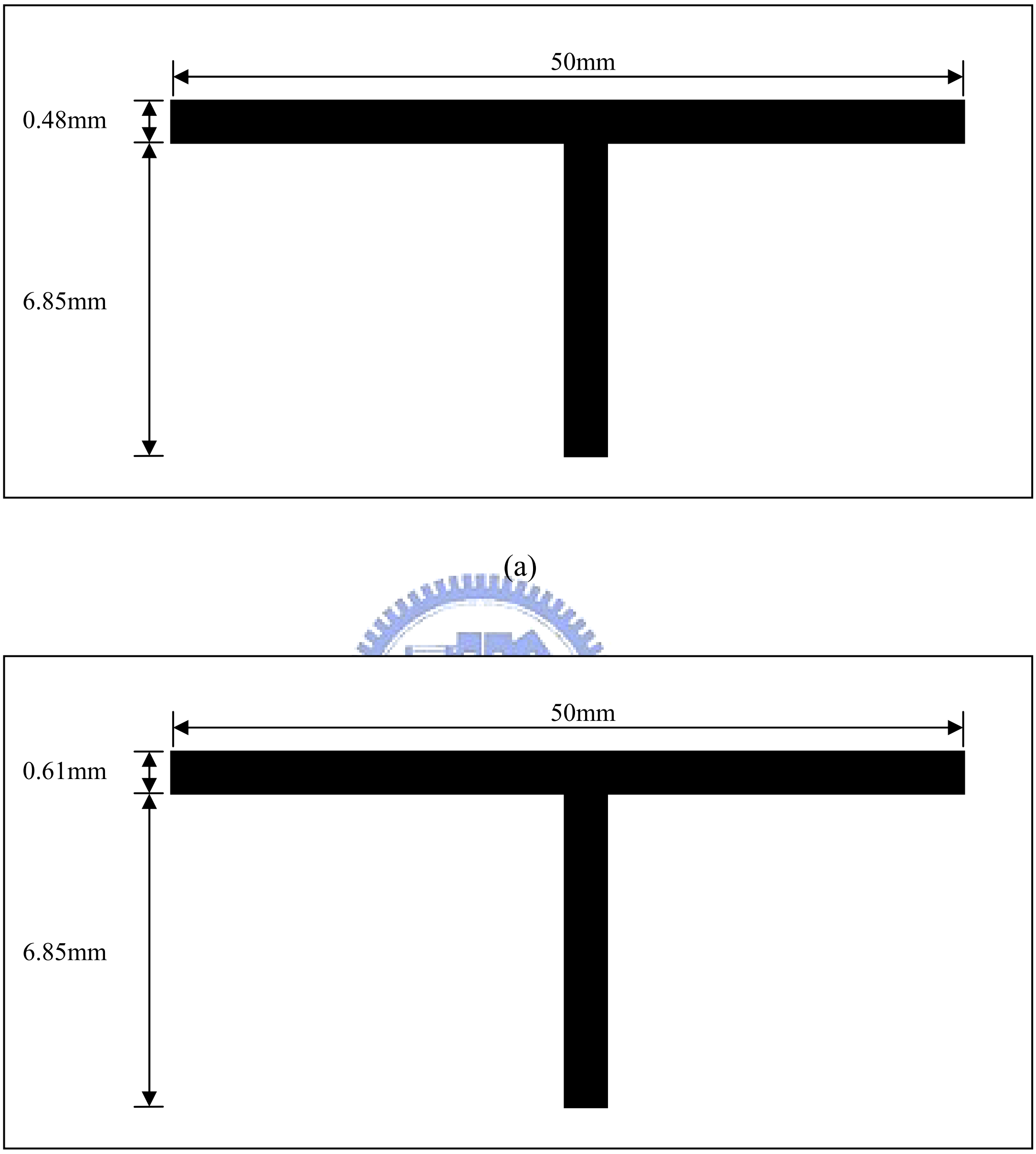

(a)

(b)

Figure 6-2. Test patterns of “T-type” microstrip resonator for silver film printed on (a) polished alumina substrate and (b) nonpolished alumina substrate, resonated at 4.32 GHz.

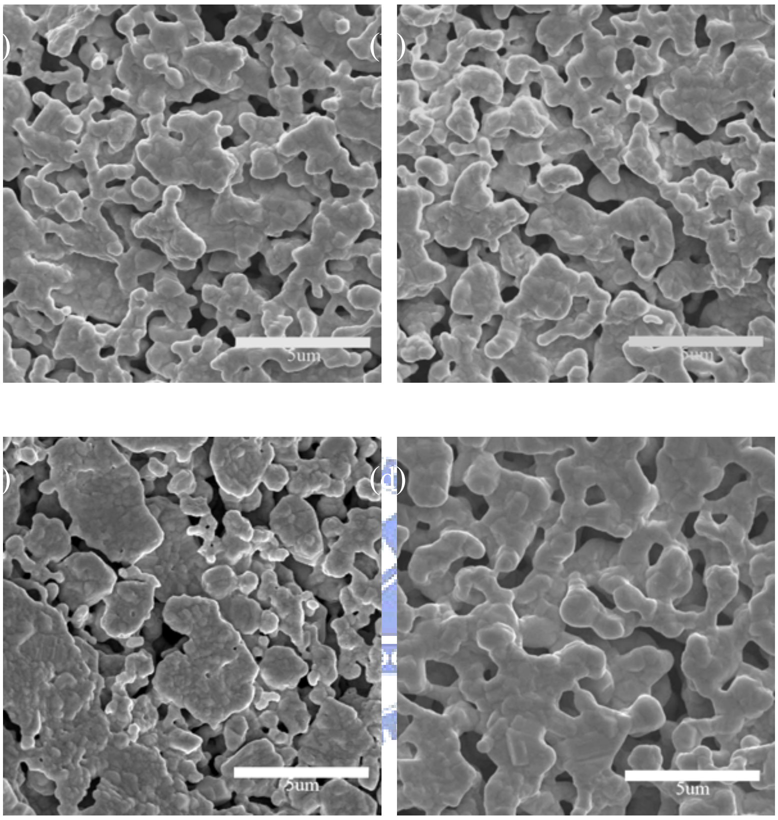

Figure 6-3. SEM surface images of films prepared using low-curing-temperature MOD silver paste screen-printed on polished substrate and fired at 250°C for (a) 10 and (c) 30 min, as well as on nonpolished substrates and fired at 250°C for (b) 10 and (d) 30 min.

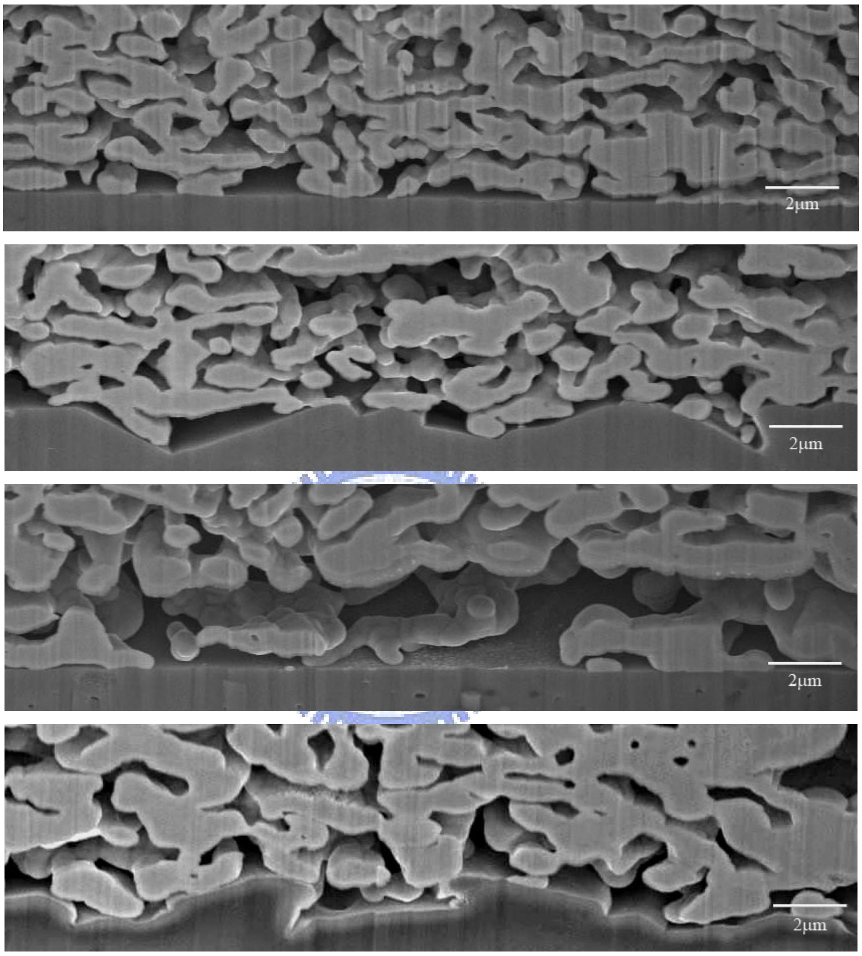

Figure 6-4. SEM images of crosssections of the films shown in Fig. 3.

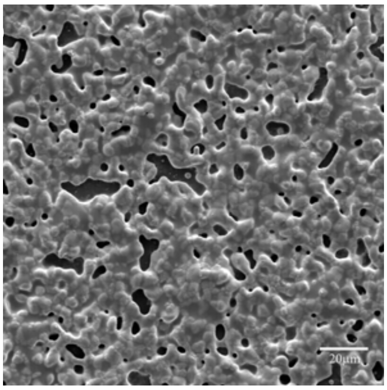

(a) High-temperature silver paste on polished substrate (top view, 500 x).

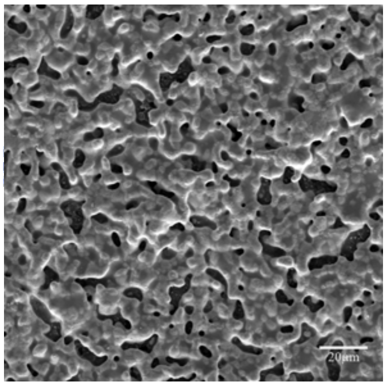

(b) High-temperature silver paste on nonpolished substrate (top view, 500 x).

Figure 6-5. SEM surface images of films prepared using high-temperature silver paste screen-printed on (a) polished and (b) nonpolished substrate and fired at 800°C for 10 min

Figure 6-6. SEM images of the crosssections of the films shown in Fig. 5.

Table 6-1 Long-term and short-term surface roughness values of silver films prepared using MOD silver paste as well as high-temperature silver paste screen-printed on polished and nonpolished alumina

Paste	Substrate	Temperature (°C)	Soaking time (min)	R_a (long-term[a)], 8 mm), μm	R_a (short-term[b)], 640 μm), μm
MOD	Polished	250	5	3.46	3.51
			10	3.50	4.04
			30	3.51	3.99
	Non-Polished	250	5	2.74	3.14
			10	2.97	3.42
			30	2.91	3.31
HT	Polished	800	30	0.93	1.42
	Non-Polished	800	30	0.83	0.97

a) Contact mode line scanning roughness measurement.

b) Noncontact mode optical profile surface morphological measurement.

Table 6-2 DC resistivities of silver films prepared using MOD silver paste as well as high-temperature silver paste screen-printed on polished and nonpolished alumina, measured using the four-point probe method.

Paste	Substrate	Temperature (°C)	Soaking time (min)	DC resistivity (Ω-cm)	Electrical conductivity (S/m)[a)]	Thickness (μm)
MOD[b)]	Polished	250	5	0.0024	8.1 x 10^{6}	22.83
			10	0.0018	8.2 x 10^{6}	23.44
			30	0.0016	9.2 x 10^{6}	25.24
	Nonpolished	250	5	0.0025	8.2 x 10^{6}	20.93
			10	0.0016	8.2 x 10^{6}	25.20
			30	0.0015	9.1 x 10^{6}	21.72
HT[c)]	Polished	800	30	0.0016	4.13 x 10^{7}	6.03
	Nonpolished	800	30	0.0016	4.08 x 10^{7}	8.56

a) The electrical conductivity was calculated using σ (S/m) = L / (R x w x t); R is the line resistivity, w is the line width, t is the line thickness, and L is the line length.

b) MOD: low-curing-temperature silver paste containing silver 2-ethylhexanoate [6].

c) HT: commercial LTCC internal electrode application (DuPont, U. S. A.)

Table 6-3 Surface resistance and effective conductivity of silver films prepared using MOD silver paste as well as high-temperature silver paste screen-printed on polished and nonpolished alumina, measured at microwave frequency range.

Paste	Substrate	Temperature (°C)	Soaking time (min)	Frequency (GHz)	Q_{unload}	$R_{surface}$ (Ω)	Conductivity (10^6 S/m)	Skin depth (μm)
MOD	Polished	250	5	4.3231	2555.74	0.05434	5.78×10^6	3.18
			10	4.3242	3073.98	0.04452	8.61×10^6	2.61
			30	4.3241	2802.82	0.04921	7.05×10^6	2.88
	Nonpolished	250	5	4.2536	2637.73	0.05560	5.43×10^6	3.31
			10	4.2486	3244.17	0.04466	8.41×10^6	2.66
			30	4.2461	3197.08	0.04506	8.25×10^6	2.69
HT	Polished	800	30	4.3232	5852.61	0.02149	3.69×10^7	1.26
	Nonpolished	800	30	4.2493	5976.20	0.02213	3.42×10^7	1.32

Table 6-4 Simulated and measured Q-values and resonance frequency values of T-type resonators prepared from the films using both low-curing-temperature MOD silver paste and high-temperature silver paste.

Paste	Substrate	Firing temperature (°C)	Soaking time (min)	Simulation[a)] using effective conductivity		Measured		ΔQ (%)
				Q_{HF}	f_0 (GHz)	Q_M	F_0 (GHz)	
MOD	**Polished**	**250**	**10**	**122.6**	**4.24**	**93.1**	**4.26**	**24.1**
			30	**114.2**	**4.26**	**89.9**	**4.25**	**21.3**
	Nonpolished	**250**	**10**	**151.5**	**4.24**	**86.7**	**4.28**	**42.8**
			30	**141.3**	**4.20**	**89.0**	**4.30**	**37.0**
HT	**Polished**	**800**	**30**	**251.3**	**4.28**	**140.0**	**4.30**	**44.3**
	Nonpolished	**800**	**30**	**273.9**	**4.27**	**134.6**	**4.30**	**50.9**

a) $\Delta Q = \frac{Q_{HF} - Q_M}{Q_M}$

Chapter 7

A Compact Cascade Quadruplet Bandpass Filter With Low Temperature Co-fired Ceramic Technology

A compact cascade quadruplet bandpass filter has been proposed. This bandpass filter has been realized with the semi-lumped method and can generate a pair of transmission zeros at the two sides of passband by using the nonadjacent cross coupling. The analysis and design procedures are provided in this paper. In order to miniaturize the size of the circuit and improve its performance, multilayered structure and the low-temperature co-fired ceramic technology are employed to design and fabricate the filter. Measurement results agree well with the electromagnetic simulation, which can validate the proposed structure.

7-1. Introduction

Compact size and low insertion loss are essential specifications within the modern telecommunication systems. In order to realize multi-band behavior, RF transceivers with more bandwidth and flexibility are utilized. Meanwhile, the technologies for integrating passive circuits to achieve multifunction, high performance, and chip-size are attractive for the microwave and millimeter-wave applications. Therefore, the low-temperature co-fired ceramic (LTCC) [1-6] seems to be one of the most efficient methods for miniaturizing and packaging technologies [7-10] because LTCC can integrate both passive and active components in a module to achieve the system-in-a-package (SiP) approach.

The bandpass filter is one of the most important components in the RF front-end. It can select passband frequencies and reduce the influence from frequencies of the adjacent channels. The lowpass prototypes have been discussed in several articles[11-12]. Levy [13] has proposed a unified theory for the synthesis of exactly equiripple lowpass prototypes. In order to realize a single pair of attenuation poles at finite frequencies, Yu et al. [14] and Hong et al. [15] adopt the microstrip open-loop resonators. Hsu et al. [16] have also adopted the coupled- resonators to design the group-delay equalizers. In this letter, the coupling scheme is proposed to control the locations of transmission zeros at both sides of passband skirts. Detailed analyses of coupling scheme and design equations are introduced in Section II. The multilayered structure of bandpass filter and fabricated unit are provided in Section III. Section IV concludes this paper.

7-2. Theory of Filter

The immittance inverter is adopted to analyze our proposed filter [17], [18]. The four-ordered quasi-elliptic bandpass filter with cross-coupling can generate a first pair of transmission zeros at finite frequencies. As shown in Fig. 1, the inverter J_{14} is connected to nodes A and B. The condition of generating the first pair of transmission zeros is $Y_{21}|_{\text{path ACDB}} + Y_{21}|_{\text{path AB}} = 0$. Assuming all of the resonators $B_i(\omega)$ are equal to $B(\omega)$, the equation can be derived as

$$\frac{J_{12}J_{23}J_{34}}{B^2(\omega)-J_{23}^2} = -J_{14} \tag{7.1}$$

Within the susceptance $B(\omega)$, both the inductor L and capacitor C are combined. This result may make the denominator of Eq. (7.1) greater than zero. Table 1 shows the relation between J_{12}, J_{23}, J_{34} and J_{14}. The positive value of J-inverter represents the circuit using the inductive coupling for the feedback loop, and the negative value of J-inverter represents the circuit using the capacitive coupling for the feedback loop.

Using the combline filter as an example. The center frequency and bandwidth ratio are defined as 2.4 GHz and 0.1, respectively, and the characteristic impedance Z_0 and the electric length θ of transmission line are choosing as 25 Ω and 25°, respectively. If the ripple of Chebyshev response is 0.01 dB, then the values of each inverter, as shown in **Figure 7-1**, can be calculated as $J_{01} = J_{45} = 0.016$, $J_{12} = J_{34} = 0.00992$, and $J_{23} = 0.00729$. Here, the frequency of transmission zero is located at the lower side of the passband at 1.9 GHz, and J_{14} can be derived, by Eq. (7.1), as –0.000394. **Figure 7-2** shows the simulated results of four ordered bandpass filters with and without the cross-coupled inverter J_{14}. For simplification, the inverters can be replaced with quarter-wavelength transmission lines. It depicts that the two transmission zeros of the simulated filter with cross-coupling J_{14} are located at 1.93 GHz and 2.97 GHz, respectively.

In **Figure 7-2**, the return loss of the filter with cross-coupling is less than the filter without cross-coupling. Moreover, the closer the two frequencies of transmission zeros to the center frequency, the worse the return loss. If two admittances Y_i, at the inputs of inverter J_{01} and J_{45}, are modified, the performance of return loss can be improved as shown in **Figure 7-3**. The admittance Y_i is matched at the central frequency and can be derived as in Eq. (7.2), and two inverters J_{01} and J_{45} are also modified as Eq. (7.3) and (7.4). As a result, the two inverters J_{01} and J_{45} are revised as 0.01667. **Figure 7-4** shows the simulated results of modified four-ordered quasi-elliptic bandpass filter and the original filter with cross-coupling J_{14}.

$$Y_i = \frac{J_{12}J_{34} - J_{23}J_{14}}{J_{23}} \tag{7.2}$$

$$J_{01} = \sqrt{\frac{J_{12}J_{34} - J_{23}J_{14}}{J_{23}R_S}} \tag{7.3}$$

$$J_{45} = \sqrt{\frac{J_{12}J_{34} - J_{23}J_{14}}{J_{23}R_L}} \tag{7.4}$$

7-3. Fabrication and Measurement

The cross-coupled four ordered bandpass filter as an example. This filter is fabricated with the substrate of Dupont 951. Its dielectric constant and loss tangent are 7.8 and 0.0045, respectively. The 2.4GHz LTCC filter is designed on four upper layers with the sheet of 1.57 mil, followed by six layers with the sheet of 3.6 mil, six layers with the sheet of 1.57 mil, and finally two layers with the sheet of 3.6 mil at the bottom. Its overall size is 132 mil × 92 mil × 41.4 mil. The simulation is carried out with the assistance of full-wave electromagnetic (EM) simulator, namely Sonnet from Sonnet Software Inc. In order to improve the accuracy of measurement, the on-wafer tester has been chosen. The network analyzer, Agilent N5230A PNA_L, is used to measure, and the short-open-load-through (SOLT) is adopted for calibration. In order to design the cross-coupled bandpass filter, with multi-layered structure, the semi-lumped method is suitable to realize four resonators. This semi-lumped method is composed of a transmission line section shunted with a capacitor. These capacitors within four resonators simply use the MIM (metal-insulator-metal) architecture to realize. The inductance coupling of L_{14} is realized by the edge coupling between the transmission lines of first and fourth resonators. The other inductance couplings of L_{12} and L_{34} adopt the broadside- coupled transmission lines. The capacitance coupling of C_{23} uses the MIM capacitor directly. **Figure 7-5(a)** reveals the detailed three-dimensional (3-D) structure of 2.4GHz LTCC bandpass filter.

As shown in **Figure 7-5(b)**, the pair of frequencies of measured and EM simulated transmission zeros are 1.93 GHz, 3.1 GHz, and 1.9 GHz, 3 GHz, respectively. At the frequency of 2.4 GHz, the measured and EM simulated insertion losses are less than 3.3 dB and 3 dB, respectively; where as the return losses are greater than19.6 dB and 27.3 dB. At the neighboring of passband, the outband rejection is more than the level of 40 dB.

7-4. Summary

The LTCC bandpass filter with coupling scheme has been proposed in this paper. The theory of generating the transmission zeros and the design procedures of filters have been analyzed. The proposed bandpass filter fabricated with the multiayered structure is realized using the semi-lumped method. The fabricated bandpass filter with the characteristics of high integration and small size is very suitable for the implementation in the multichip module. Agreement between measurement and theoretical prediction has evidenced the feasibility of our study.

References:

1. K. Kunihiro, S. Yamanouchi, T. Miyazaki, Y. Aoki, K. Ikuina, T. Ohtsuka, H. Hida, in *IEEE Radio Frequency Integrated Circuits Symp. Dig.*, 2004, pp. 303–306.
2. J. Muller and H. Thust, in *Pan Pacific Microelectron. Symp. Dig.*, 1997, pp. 211–216.
3. C. Q. Scrantom and J. C. Lawson, in *IEEE MTT-S Int. Microwave Symp. Dig.*, 1999, pp. 193–200.
4. Y. Rong, K. A. Zaki, M. Hageman, D. Stevens, and J. Gipprich, in *IEEE MTT-S Int. Microwave Symp. Dig.*, June 1999, pp. 1147–1150.
5. D. Heo, A. Sutono, E. Chen, Y. Suh, and J. Laskar, *IEEE Microwave Wireless Comp. Lett.*, vol. 11, pp. 249–251, June 2001.
6. W. Y. Leung, K. K. M. Cheng, and K. L. Wu, in *Proc. Asia-Pacific Microwave Conf.*, Dec. 2001, pp. 1008–1011.
7. Y. L. Low and R. C. Frye, *in IEEE Multi-Chip Module Conference (MCMC’97)*, 1997, pp. 27–32.
8. A. B. Frazier, R. O. Warringtun, and C. Friedrich, *IEEE Trans. Indus. Elec.*, vol. 42, pp. 423–430, Oct. 1995.
9. A. Matsuzawa, *IEEE Trans. Microwave Theory and Tech.*, vol. 50, pp. 245–253, Jan. 2002.
10. K. L. Tai, *in Proceedings of the Asia and South Pacific Design Automation Conference (ASP-DAC)*, 2000, pp. 211–216.
11. R. M. Kurzrok, *IEEE Trans. Microwave Theory Tech.*, vol. 14, no. 6, pp. 295–296, June 1966.
12. J. D. Rhodes, *IEEE Trans. Microwave Theory Tech.*, vol. MTT-18, no. 6, pp.

290–301, April 1970.

13. R. Levy, *IEEE Trans. Microwave Theory Tech.*, vol. MTT-24, no. 4, pp. 172–181, April 1976.
14. C. C. Yu and K. Chang, *IEEE Trans. Microwave Theory Tech.*, vol. 46, no. 7, pp. 952–958, July 1998.
15. J. S. Hong and M. J. Lancaster, *IEEE Trans. Microwave Theory Tech.*, vol. 48, no. 7, pp. 1098–1107, July 2000.
16. H. T. Hsu, H. W. Yao, K. A. Zaki, and A. E. Atia, *IEEE Trans. Microwave Theory Tech.*, vol. 50, no. 8, pp. 1960–1968, August 2002.
17. G. L. Matthaei, L. Young, and E. M. Jones, *Microwave Filters, Impedance-Matching Network, and Coupling Structures*. Norwood, MA: Artech House, 1980.
18. J. S. G. Hong and M. J. Lancaster, *Microstrip Filters for RF/Microwave Applications*. New York, NY: John Wiley & Sons, Inc., 2001.

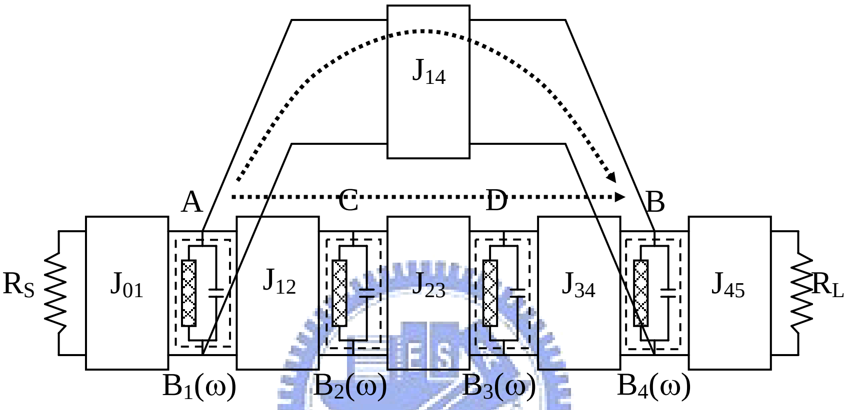

Figure 7-1. Equivalent circuit of four-ordered quasi-elliptic bandpass filter with cross coupling.

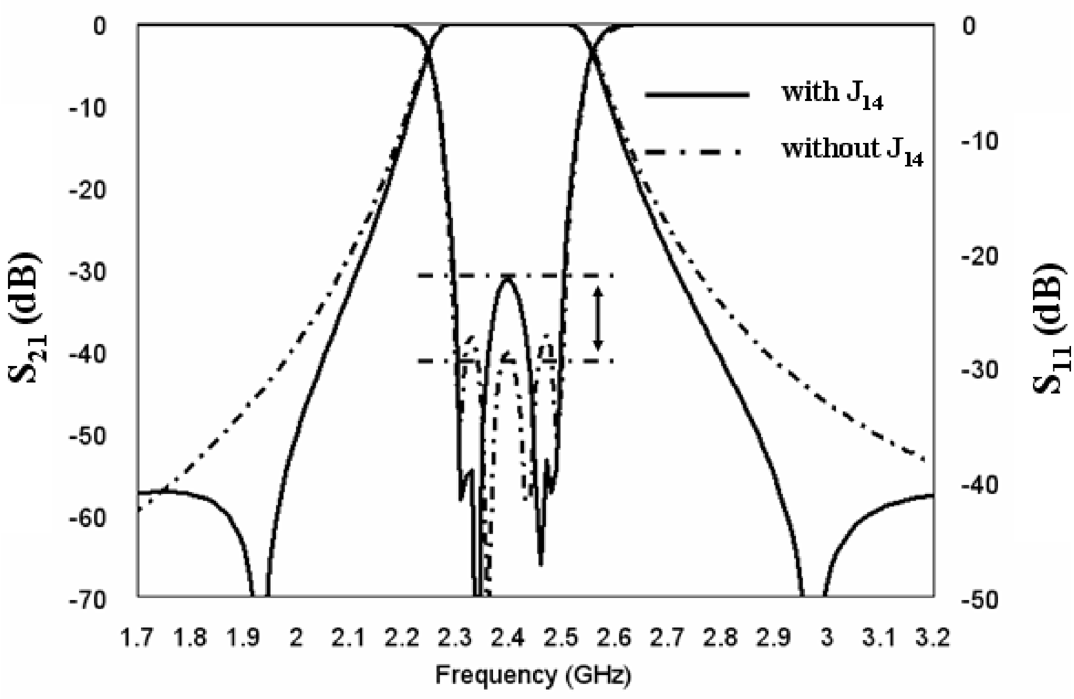

Figure 7-2. Simulated results of four ordered bandpass filters.

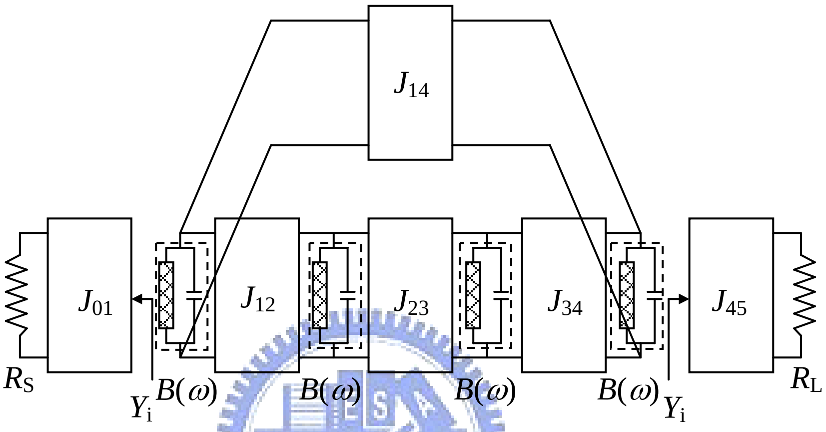

Figure 7-3. Four ordered bandpass filter, which has considered the impedance matching in the inverters J_{01} and J_{45}.

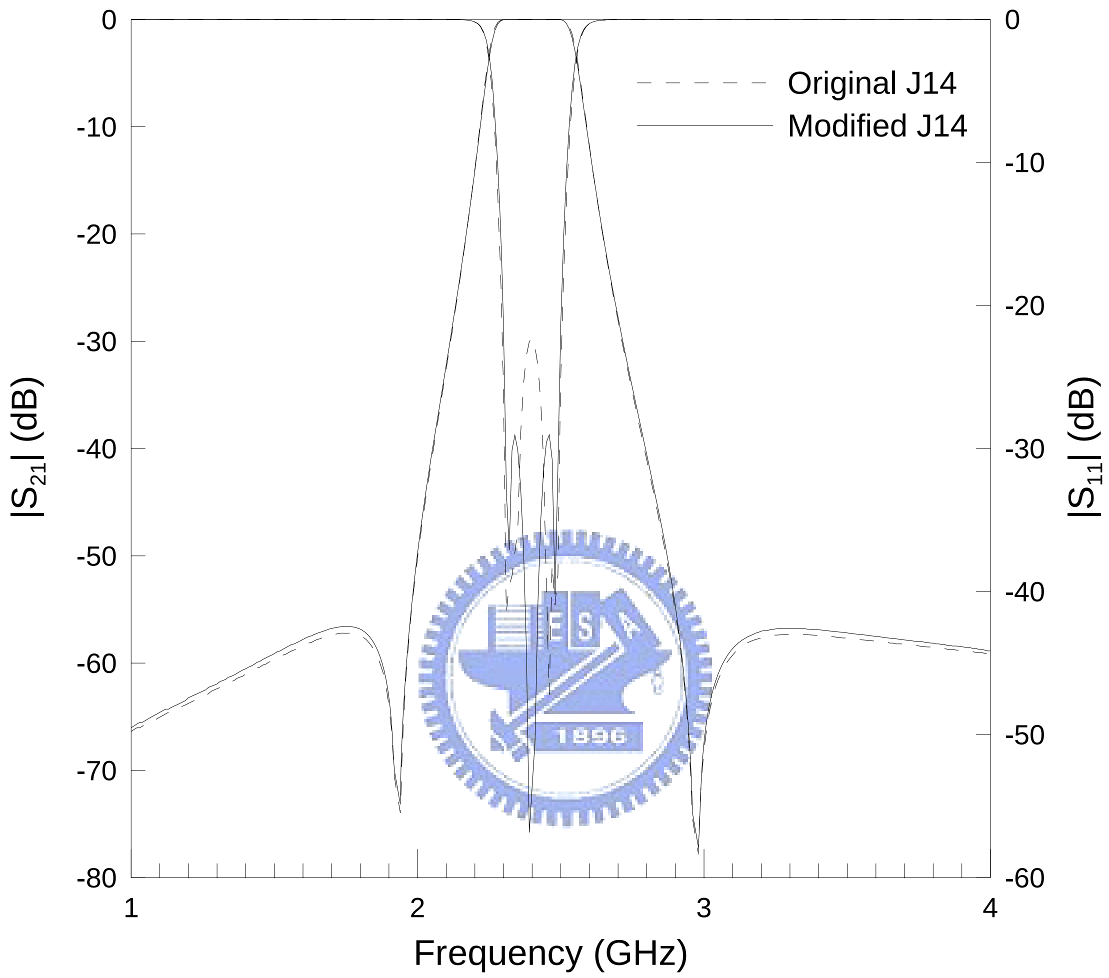

Figure 7-4. Compare the responses of modified four ordered bandpass filter with the original filter with cross-coupling J_{14}.

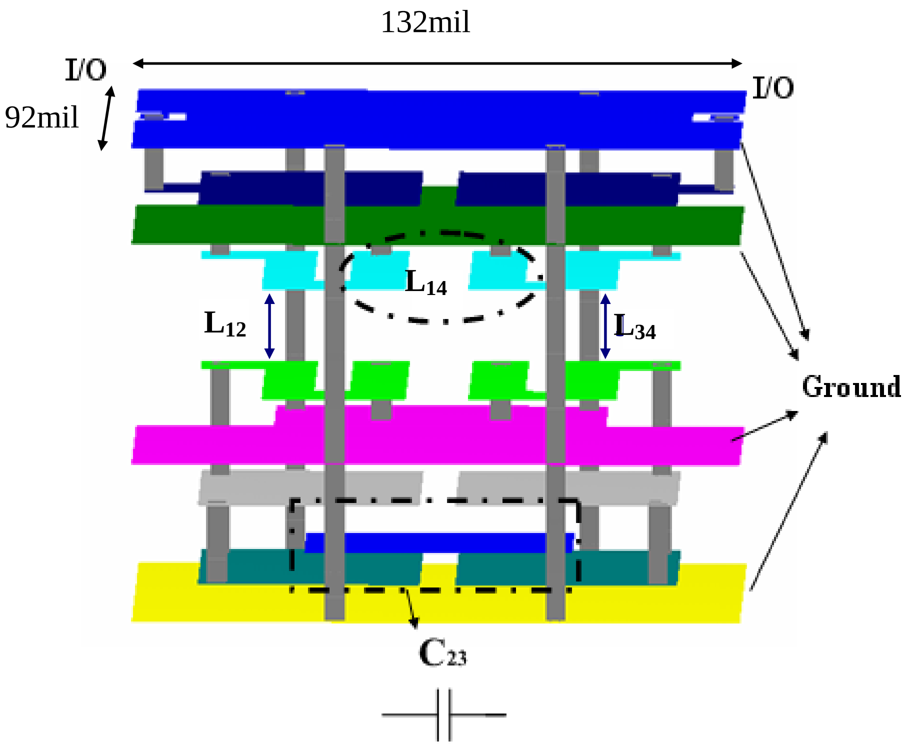

Figure 7-5(a). Fabricated cross-coupled four ordered LTCC bandpass filter. (a) 3-D structure and (b) measured and EM simulated results.

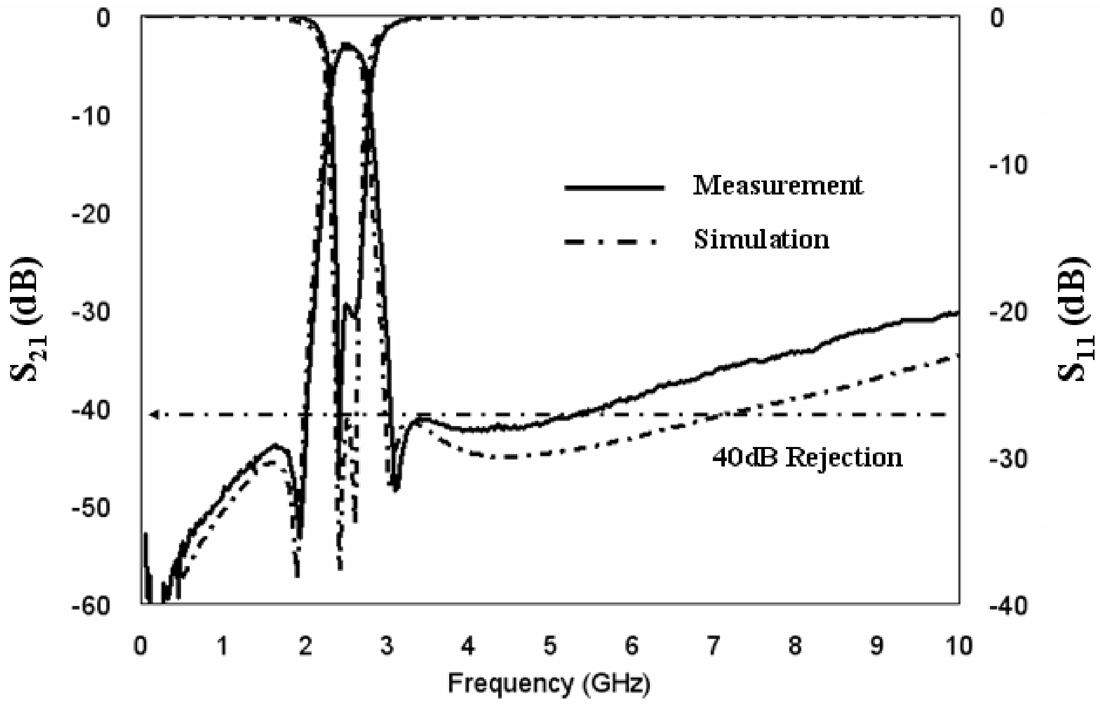

Figure 7-5(b). Fabricated cross-coupled four ordered LTCC bandpass filter. (a) 3-D structure and (b) measured and EM simulated results.

Table 7-1. Conditions of Appearing the Transmission Zero

$J_{14} = +\ \pi/2$			$J_{14} = -\ \pi/2$		
J_{12}	J_{23}	J_{34}	J_{12}	J_{23}	J_{34}
$+\ \pi/2$	$+\ \pi/2$	$-\ \pi/2$	$-\ \pi/2$	$-\ \pi/2$	$+\ \pi/2$
$+\ \pi/2$	$-\ \pi/2$	$+\ \pi/2$	$-\ \pi/2$	$+\ \pi/2$	$-\ \pi/2$
$-\ \pi/2$	$+\ \pi/2$	$+\ \pi/2$	$+\ \pi/2$	$-\ \pi/2$	$-\ \pi/2$
$-\ \pi/2$	$-\ \pi/2$	$-\ \pi/2$	$+\ \pi/2$	$+\ \pi/2$	$+\ \pi/2$

Chapter 8

Conclusion and Suggestion of Future Work

8-1 *Conclusion*

With the addition of silver oxalate, the decompositions of alpha-terpineol and silver 2-ethylhexanoate occur at temperatures below 190°C, the silver oxalate at ≈210°C, and the lubricant on the surfaces of silver flakes at ≈222°C. The resistivity of the film prepared from the pastes decreases with increasing curing temperature, due to a better connectivity of the metal particles associated with the decomposition of organics. A resistivity of 31.9 Ω-cm was obtained for the film prepared from the paste with 10 wt% silver oxalate added and curried at 225°C.

The silver flake and binder in the paste were replaced by Ag_2O and silver stearate, to reduce the curing temperature while maintaining the required paste characteristics and electrical properties of the final film. Results indicate that all pastes appear to have pseudoplastic flow (shear-thinning) property. The lowest electrical resistivity of 13.2x10-6 Ω-cm was obtained for the film prepared from paste with the Ag_2O/silver stearate ratio of 100:5 at a solid loading of 80wt% in solvent α-terpineol, after being cured at 160°C for 5min. The three-dimensional interconnection network was resulted from the coalescence of fine silver particles decomposed from silver stearate and neckgrowth of the coarse silver grains reduced from Ag_2O.

The films screen-printed on the polished substrate have a higher Q and a lower ΔQ value than those of films that are screen-printed on the nonpolished substrate. For the silver films prepared using the high-temperature silver paste, both the Q and ΔQ values were the highest among the films studied, which is consistent with the observation of the dense microstructure of the silver film and the interfacial reaction between the glass in the film and the substrate as a result of high firing temperature.

The proposed bandpass filter fabricated with the multiayered structure is realized using the high temperature silver paste. The fabricated bandpass filter with the characteristics of high integration and small size is very suitable for the implementation in the multichip module. Agreement between measurement and theoretical prediction has evidenced the feasibility of our study.

8-2 *Future Work*

The important future work must be conquered for lower curing temperature with PET or Paper substrate. As the cost effect, pattern formation has to use the high throughput method, such as gravure printing, flexo printing for flexible electron requirement. The present developing curing temperature is near 160^{0}C dwell time between 5 to 30min all of higher than PET process limit temperature and must down to 130^{0}C.

At last, this study will keep going to achieve radio frequency electrical properties of low-temperature-curing silver paste by designing and fabricating components.

簡歷

姓名：林鴻欽

性別：男

出生年月日：民國五十五年一月十三日

出生地：高雄市

地址：高雄市縣三民區遼寧二街222巷8號

學歷：

國立成功大學地球科學系學士畢業

(民國七十五年九月至民國七十九年六月)

國立成功大學地球科學研究所碩士畢業

(民國八十年九月至民國八十一年六月)

國立交通大學材料科學及工程研究所博士班畢業

(民國八十八年九月至民國九十七年六月)

博士論文題目：

低溫化銀電極膏製備與高頻應用之研究

Preparation and High-frequency Application of Low-temperature-curing Silver Paste

經歷

工業技術研究院材料與化工研究所研究員